Master Thesis, Department of Geosciences

Petrography, structure and metamorphism of mélange rocks below the Jotun Nappe in Stølsheimen, Central South Norway

Øystein Kjelberg

UNIVERSITY OF OSLO

FACULTY OF MATHEMATICS AND NATURAL SCIENCES

Petrography, structure and metamorphism of mélange rocks below the Jotun Nappe in Stølsheimen, Central South Norway

Øystein Kjelberg

Master Thesis in Geosciences
Discipline: Structural Geology and Tectonics
Department of Geosciences
Faculty of Mathematics and Natural Sciences

University of Oslo
December 2015

Supervisor: Prof. Torgeir B. Andersen

This work is published digitally through DUO – Digitale Utgivelser ved UiO
http://www.duo.uio.no
It is also catalogued in BIBSYS (http://www.bibsys.no/english)

Acknowledgements

First and foremost I would like to thank my supervisor Torgeir Andersen for help with the writing of this thesis and for always be available for discussion and questions. His review and guidance has been greatly appreciated.

I would also like to thank my field partner Anders Enger for discussion during the fieldwork and during the writing of the thesis, and to Johannes Jacob and Fernando Corfu for joining us the first days in the field.

I would also like to thank my fellow master students at CEED for many breaks during the writing of this thesis. Also big thanks to all the other staff at CEED and the Department of Geosciences for help and guidance with the geochemistry analyses. This thesis would not have been a reality without your help.

Last I would like to thank my family for their support the last year.

Abstract

The Caledonian mélange unit of South Norway is a unit that has largely been overlooked in previously studies of the Caledonides. The mélange consists of “Alpine type” metaperidotite bodies now found as serpentinites, talc and serpentine conglomerate. The ultramafics are set in a metasedimentary matrix, together with some minor meta-basalt/gabbro units. The mélange has recently been identified as a separate tectonic unit and is believed to be remnants of a hyperextended margin, and challenges the traditional interpretation of the Scandinavian orogen. The unit is positioned structurally below the crystalline nappes previously assigned to the Middle Allochthon. Recent works have recognized that the Allochthone units of the Caledonian orogen have a much more complex relationship than previously believed.

This thesis investigates the mélange unit at Selhamar, Stølsheimen in search of a more detailed description of the host rocks surrounding the ultramafic bodies in term of petrography, structures and metamorphism. The ultramafic bodies in the study area of this thesis are described in detail by Enger (work in progress). In Stølsheimen the mélange unit lies structurally between the Lower and Upper Bergsdalen nappes, underneath the Jotun Nappe Complex. The metasediments in the study area consists of metasandstone, metapelites and garnet micaschist, and are found together with some minor (garnet) amphibolite outcrops and slivers of gneissic rocks from the Upper Bergsdalen Nappe.

The metasediments was exposed to upper greenschist to lower amphibolite metamorphic conditions (515-525^{o}C and 7100-7450bars) during the Caledonian orogen. This is based on thermobarometric modelling by the use of the *Theriak-Domino* program suite together with bulk rock composition. The study area is dominated by top-to-the-NW shear direction and large scale folding, corresponding to Caledonian extension.

Table of contents

1. Introduction

1.1 Purpose of the study

The purpose of this thesis is to study the metasediments, metaigneous rocks and associated orthogneisses, constituting the wall rocks of the solitary mantle peridotite situated in Stølsheimen, between Voss and Sognefjorden. The deformed rocks that contain these mantle rocks form a part of a regional, mixed unit (mélange) that can be traced across southern Norway from the Bergen area towards Otta, and possibly beyond.

The study includes detailed mapping and sampling of the rocks in a selected area around the Raudberget metaperidotite in the western parts of southern Norway (fig. 1.1). These rocks are then subject to detailed petrography and structural/metamorphic examination in order to characterized their origin of formation and later structural and metamorphic modification. The data will also be compared to observations from other parts of the Caledonides and present day hyperextended margins.

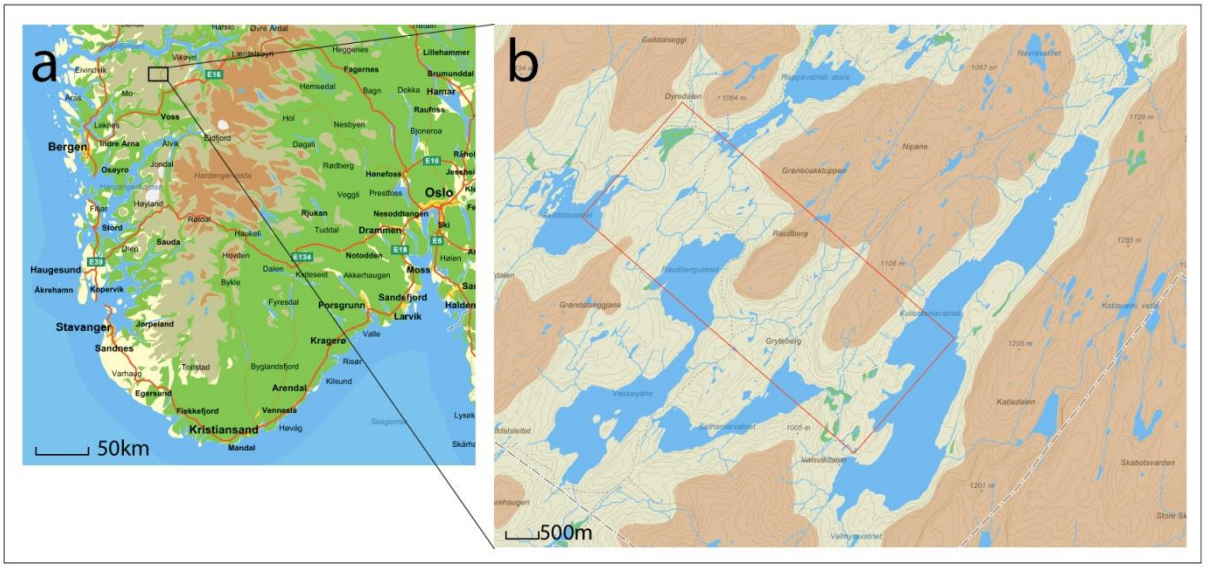

Fig. 1.1A: Map over South Norway. B: Zoomed in map over Stølsheimen. Field area marked inn red. Maps from kart.gulesider.no

1.2 Previous works in the study area

NGU (Norwegian Geological Survey) had a project in the Raudberget area in the 1980s, together with A/S Norwegian Talc and Sogn og Fjordane county. The goal of the project was to make a detailed evaluation of the talc, carbonate and sulphide deposits in the Raudberget area, with the goal of finding exploitable deposits to mine. The project resulted in several reports made by NGU together with two master theses (Torstensen, 1981; Aarflot, 1984). The NGU reports contains considerable information on the metaperidotites and drill-core description which has been used in this thesis.

Kvale (1946) and (Fossen, 1993a; b) investigated the structural geology and metamorphism in the Bergsdalen nappes that are found adjacent to the mélange. Andersen *et al.* (2012) used the Raudberget area in search of evidence of remnants of a pre-Caledonian hyperextended margin of the coast of Baltica and Fauconnier *et al.* (2014) looked into the peak metamorphic conditions in the area during the Caledonian orogen by using Raman Spectroscopy. All these articles are used and explained later in the text. The available geological maps of the study area include maps at the scale of 1:250.000 from NGU (geo.ngu.no/kart/berggrunn/).

2. The Caledonian orogeny

The Caledonian orogeny was formed by a large scale continent-continent collision between the paleocontinents Baltica, Avalonia and Laurentia. The orogenic belt is comparable in size and evolution, to the present day Himalayas (e.g. Labrousse *et al.*, 2010). Gradual convergence of the continental plates led to a collision where Baltica was partly subducted underneath Laurentia in Middle to Late Silurian to Early Devonian time (e.g. Roberts, 2003). Remnants of the orogen can today be traced for several thousand kilometres (Corfu *et al.*, 2014).

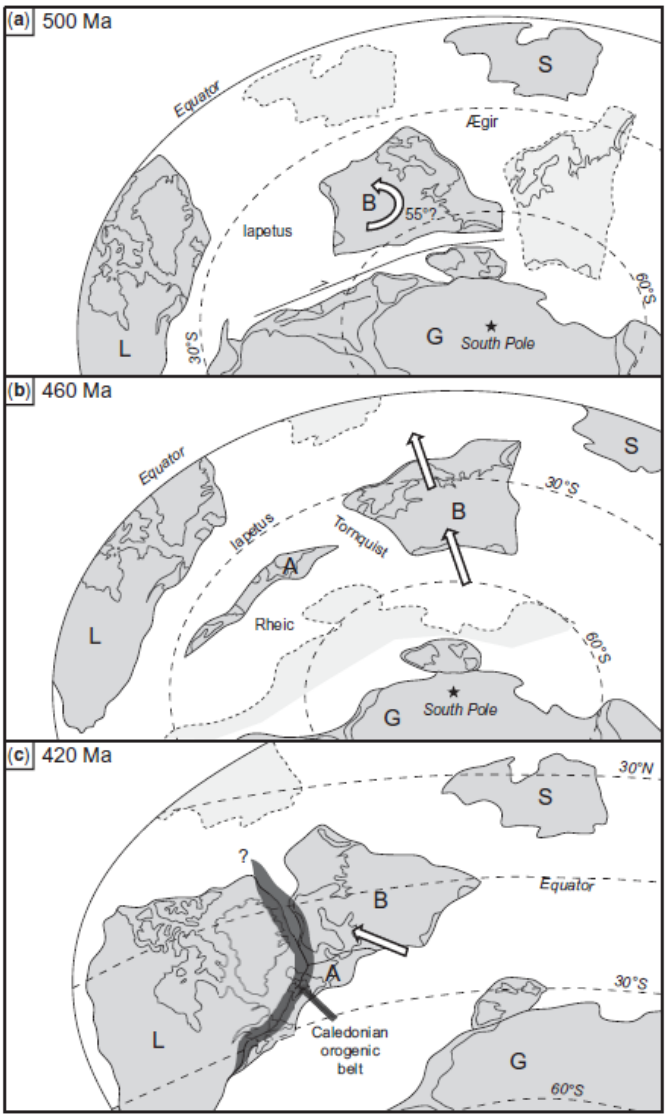

Fig. 2.1: Reconstructed paleographic positions of Baltica (B), Sibiria (S), Gondwana (G) and Avalonia (A) leading up to the Caledonian orogeny. Light grey areas show alternative interpretations of the positions for the three continents. From Corfu et al. (2014).

The orogeny was the product of several orogenic phases/events, in addition to late extensional collapse associated with orogeny-parallel sinistral shear (e.g. Andersen, 1998; Roberts, 2003). Fig. 2.1 shows the movement of Baltica, Avalonia and Laurentia leading up to the Scandian event of Caledonian orogeny and final closure of the Iapetus Ocean.

The Scandian event is the main event of the Caledonian orogeny in Scandinavia, and is marked by the final closure of the Iapetus Ocean at ca. 430 Ma (Fig. 2.1). The Baltoscandian margin of Baltica was subducted underneath Laurentia, and the ultrahigh pressure rocks in the Western Gneiss Region reached their

maximum burial depth in the early Devonian (Andersen *et al.*, 1991; Terry *et al.*, 2000; Hacker *et al.*, 2010).

The major allochthonous units of Caledonian orogeny is traditionally divided into four; the Lower, Middle, Upper and Uppermost Allochthones. These were transported several hundred kilometres in a south-eastern direction during the collision (Roberts, 2003). In the traditional classification the nappe-complexes below the Upper Allochthon were all assigned with an origin form the margin of Baltica. The Upper Allochthon was remnants of the Iapetus Ocean (ophiolites, island arcs and associated rocks) and the Uppermost Allochthon was thought to represent the overriding Laurentian continent (Corfu *et al.*, 2014).

Main units of the Scandinavian Caledonides distinguished in this paper	Classification used in Gee *et al.* (1985)
Northern segment	
Lyngen ophiolite	UMA
Hellefjord	MA
Magerøy, Reisa (Vaddas)	UA
Kalak Nappe Complex	MA
Laksefjord, Gaissa	LA
Autochthonous cover	A
Reworked basement	PA
Barents Sea Region	A
Autochthon	A
Central segment	
Devonian	Devonian
Beiarn, Niingen, Nakkedal, Tromsø	UMA
Helgeland, Ofoten, Lyngen	UMA/UA
Rödingsfjället, Heggmo	UMA
Fauske	UMA
Narvik, Lyngen ophiolite	UMA
Köli, Støren, Meråker, Leka, Reisa	UA
Gula	UA
Seve	UA (MA)
Särv	MA
Kvitvola, Rondane, Tännäs, Veman, Offerdal, Akkajaure	MA
Osen–Røa, Jämtland	LA
Autochthonous to allochthonous cover	A-PA-LA
Reworked basement	PA-LA
Autochthon	A
Southern segment	
Devonian	Devonian
Sunnhordland, Solund–Stavfjord, Gula, Støren, Meråker	UA
Seve	UA (MA)
Revsegg, Jæren	MA
Upper Jotun, Lindås, Kvitenut, Upper Finse	MA
Lower Jotun and unspecified crystalline nappes	MA
Espedalen, Eikefjord, Dyrskard	MA
Lower Finse	MA
Upper Bergsdalen	MA
Sparagmite, Kvitvola, Valdres, Rondane	MA
Extensional mélange	–
Lower Bergsdalen	LA
Osen–Røa, Synfjell, Holmasjø, Phyllite nappes	LA
Autochthonous to allochthonous cover	A-PA-LA
Reworked basement	PA-LA
Autochthon	A

Note: A, Autochthon; PA, parautochthon; LA, Lower Allochthon; MA, Middle Allochthon; UA, Upper Allochthon; UMA, Uppermost Allochthon.

Table 2.1: Classification of the Caledonian nappes as suggested by Corfu et al (2014), with the older classification from Gee (1985). From Corfu et al. (2014)

Corfu *et al.* (2014) pointed out that the traditional classification was too simplified and rigid. The Allochthones do not always have a simple tectostrategraphic order, and units with different origins maybe juxtaposed with each other in a complex fashion. One example of this is the Jotun and Lindås nappes which correspond with the age and metamorphic history of the Middle Allochthon, structurally overlie a regional mélange unit with abundant ultramafic rocks. This unit is believed to originate from the Iapetus Ocean (Andersen *et al.*, 2012) and to be typical of the Upper Allochthon (Corfu *et al.*, 2014). Instead Corfu *et al.* (2014) used the local names and described the nappe-stack in three segments (north, central and south), without correlating the nappes along the entire length of the mountain belt (table 2.1). The motivation was to

avoid unjustified correlations and interpretations inherited from the previous regional correlations (e.g. Bryhni and Andréasson, 1985)

2.1 The Caledonides in southern Norway

The southern segment of the Scandinavian Caledonides is in large scale dominated by these tectonic elements, from the foreland in the SE to the hinterland in the NW (Corfu *et al.*, 2014):

a) Autochthonous Mesoproterozoic basement overlain by an autochthonous cover and a parautochthonous to allochthonous fold-and thrust belt of mainly Lower Palaeozoic cover rocks.

b) Large scale allochthonous nappes consisting of Mesoproterozoic basement, locally with (meta)sedimentary cover.

c) Allochthonous nappes of Palaeozoic age, mostly oceanic rocks.

d) Variably Caledonized Middle Proterozoic basement of the Western Gneiss Complex (WGC), also called Western Gneiss Region (WGR).

e) Devonian deposits.

The autochthonous basement in the southern Scandinavia (a) was assembled during the Sveconorwegian orogeny (1150-900 Ma), and constitute large areas of the eastern part of southern Norway (e.g. Bingen *et al.*, 2008) (fig. 2.2). Overlaying the autochthonous basement and cover, is a group of large allochthonous nappes (b). These nappes dominantly consist of crystalline rocks and are up to 14 km thick (Smithson *et al.*, 1974).

The nappes consists of continental crust mostly formed at 1700-1600 Ma and/or around 1500 Ma, with intrusions aged 1450 and 1300-1250 occurring locally (Schärer, 1980; Lundmark *et al.*, 2007; Lundmark and Corfu, 2008; Roffeis *et al.*, 2012; Roffeis *et al.*, 2013; Corfu and Heim, 2014; Roffeis and Corfu, 2014). The nappes were assembled during the Sweconorwegian (e.g. Kvitenut nappe) and the Caledonian orogeny (e.g. Lindås and Bergsdalen nappes) (Corfu *et al.*, 2014). During the Caledonian orogeny these nappe complexes underwent a variety of different metamorphic conditions. The Lindås nappe

experienced high-pressure metamorphism and reached eclogite facies along shear zones (e.g. Austrheim, 1987), while for example the Lower Jotun Nappe has only moderate Caledonian overprint (e.g. Schärer, 1980).

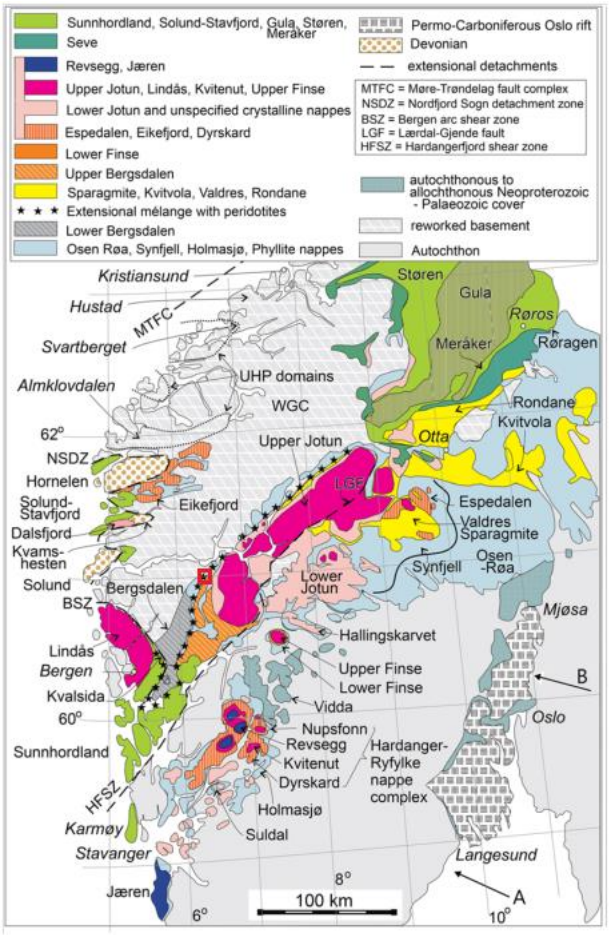

Fig. 2.2: Tectonic map showing the southern segment of the Caledonian orogeny, with the major nappes complexes. Note the extensional mélange running from the Bergen area and north-eastwards across the southern Norway, with the field area in this thesis marked with red. From Corfu et al. (2014).

On top of, and partly interlayered with, the Proterozoic crystalline nappes lies a sequence nappes consisting of ophiolitic and island arc nappes (c) formed in the pre-Caledonian ocean basin(s), including the Iapetus Ocean. In the Western Norway these nappes consist of two groups, Sunnhordland and Jæren. Sunnhordland comprises of Early to Middle Ordovician ophiolites and island arc sequences. The Jæren nappe consists of metasedimentary rocks with minor eclogite lenses and granodioritic to tonalitic bodies (Corfu *et al.*, 2014).

The Western Gneiss Complex (d) is a large area of high and ultra-high pressure metamorphism, covering more than 50 000 km^2 of the north-western part of South Norway (fig. 2.2). The WGC has a continuous metamorphic gradient from amphibolite facies rocks in the ESE to eclogite facies rocks in the WNW (e.g. Hacker *et al.*, 2010).

2.1.1 Origin of the ultramafic bodies in the mélange in South Norway

The ultramafic bodies found in the mélange (fig. 2.2) has been described as remains of an ophiolite sequence, but an ophiolite association not easily recognisable (Qvale and Stigh, 1985). There is no pillow basalt, gabbro or sheeted dykes observed together with the

ultramafic rocks. Serpentinites are found along the length of the Scandinavian Caledonides and are often found together with detrital serpentinites/serpentine conglomerates (Qvale and Stigh, 1985, see also Alsaif, 2015). The origin of the conglomerates have been suggested to be volcanic, either as pyroclastic deposits or combined with sedimentary processes (Oftedahl, 1969; Strand, 1970). Qvale and Stigh (1985) (along others) suggested that the conglomerates were provided by a serpentinites with an ophiolitic origin, and this was later considered to represent a terrain-linking unconformity (e.g. Sturt *et al.*, 1991; Sandstad *et al.*, 1993; Sturt and Ramsay, 1999). The Reiggehaugen serpentinite conglomerate found south of Vågå (see Alsaif, 2015) was by Sturt and Ramsay (1999) and Sturt *et al.* (1991) suggested to be a part of the Vågåmo ophiolite, unconformable overlying the Sel Group which includes the fossil-bearing Otta conglomerate with fossils with a Llanvirn age (Bruton and Harper, 1981). The Otta fossils are well preserved within the conglomerate and have an mixed Baltic and North American affinities (Bruton and Harper, 1981; Neuman, 1984). The Otta fossils belongs to a Celtic fauna developed seaward of the main continents of Laurentia and Baltica (Harper *et al.*, 2009). The interpretation of (Sturt *et al.*, 1991; Sturt and Ramsay, 1999) should probably be reconsidered, based on their tectonostratigraphic positioning (Andersen *et al.*, 2012; Alsaif, 2015). One of the problems with this interpretation is that the ophiolite is not a proper ophiolite and the serpentinite conglomerates are in sequence rather than unconformable (Jakob *et al.*, in prep (a)).

More recently the origin of the metaperidotites was by Andersen *et al.* (2012) suggested to be remnants of hyperextension of the Fennoscandian continental crust. They explained their hypothesis with use of direct and indirect evidence:

1) The mantle peridotites have supplied the basin with clastic material, such as the serpentine conglomerate found in the study area in this thesis (see below). This shows that the exhumation of the ultramafics to the seafloor most have happened prior to the Caledonian collision, when the basin still was receiving sediments.

2) Widespread serpentinization and talcification of ultramafic rocks and formation of ophicalcite is typical of peridotites exhumed through the process of hyperextension at passive continental margins.

3) There is no contact metamorphism visible between the ultramafics and the surrounding host rocks, meaning that the ultramafics cannot be a result of magmatic intrusion and crystallization. The only other likely mechanism is structural emplacement

3. Hyperextended passive margins

3.1 Magma poor rifted margins

Rifted margins used to be presented as juxtaposition of continental and oceanic crust through simple shear, pure shear or composite deformation mechanisms, but are now undergoing a paradigm shift (e.g. Peron-Pinvidic *et al.*, 2013). Observations of distal rifted margins lead to the discovery of structural setting of exhumed subcontinental mantle and/or hyperextended continental crust, questioning the validity of some rifting models (Peron-Pinvidic *et al.*, 2013). Fig. 3.1 shows a schematic section of a typical rifted margin, with the different structural domains.

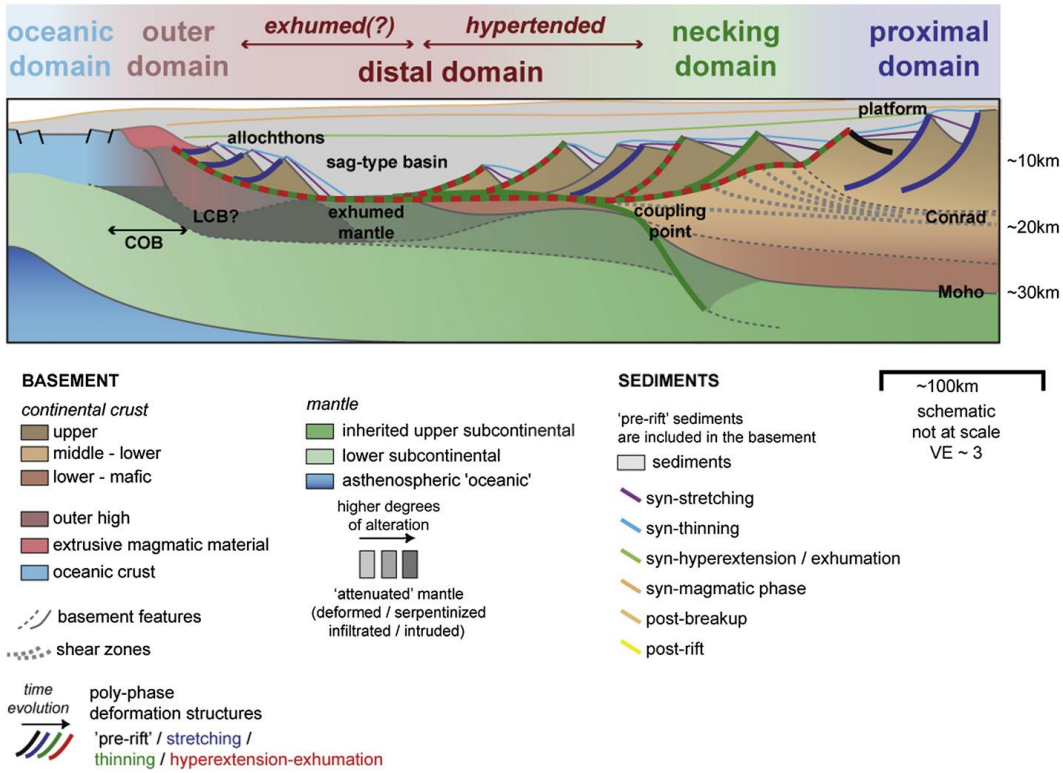

Fig. 3.1: A cartoon showing a typical example of a rifted margin, with the placement of the different domains, including hyperextended domain and exhumed mantle. The colour coding on the faults indicate when they were active, with black being pre-rift, blue during stretching of the crust. Green and red faults are active during the thinning and exhumation period. The green and red dotted line is faults active during both thinning and hyperextension. From Peron-Pinvidic et al. (2013)

The Proximal domain

The proximal domain is often referred to as *platforms*, and is the part of the system closest to the continent. This domain is characterized by graben and half-graben systems filled with syn-tectonic sediments. The major faults cuts down through the upper crust, but they do not reach or affect the Moho and the crustal thinning in this part of the system is low (Peron-Pinvidic *et al.*, 2013).

The necking domain

The necking domain is the part of the margin where the crustal thickness is extended to such a degree that the thickness of the crust is reduced to less than 10 km (Péron-Pinvidic and Manatschal, 2009). This domain has an increase in accommodation space towards the basin (Sutra and Manatschal, 2012). The coupling point is the first point where the crust is thinned to less than 10km and the taper break is the point where the first brittle faults cut through the entire crust and down into the upper mantle. The coupling point and the taper break are commonly found close by each other or at the same place, and are found in the outer part of the necking domain (Peron-Pinvidic *et al.*, 2013).

The distal domain

The distal domain is the part of the margin that includes hyperextended continental crust and exhumed mantle, and is also referred to as the hyperextended domain. This domain includes both upper and lower continental crust, and exhumed mantle rocks with various degree of serpentinization. In some cases the distal domain also contain embryonic oceanic crust (Peron-Pinvidic *et al.*, 2013).

The outer domain

The outer domain is located between the basement of the distal domain and the oceanic crust. Ideally the oceanwards limit of the outer domain corresponds to the ocean-continent transition (OCT). Continentwards the definition of the limit is less well defined, but it can correspond to either the oceanwards closure of the sag-basin or the slight deepening of the

seismic Moho associated with important basement topography (see Fig 3.1 and Peron-Pinvidic *et al.*, 2013).

3.2 The formation of hyperextended passive margins

Hyperextended margins are characterized by a wide continent-ocean transition with a small amount of magmatism during crustal thinning and mantle exhumation prior to oceanic spreading (Pérez-Gussinyé, 2013). Hyperextension is a term used on passive margins where an assumed crustal thickness of 30-35 km is stretch by a factor of 3-4 (Lundin and Doré, 2011), ending up with a crustal thickness of less than 10 km and exposure of mantle rocks over large areas (>150-180 km wide). These margins typically have an asymmetrical tectonic structure (Minshull *et al.*, 2001). The stretching of the crust lead to embrittlement and coupling of the lower and upper crust, which allow faults to cut through the entire crust and down to the upper mantle. This process leads to partial hydration (serpentinization) of the upper mantle (Doré and Lundin, 2015).

When lithospheric plates are extended and thinned they form rift basins, and if the rifting continuous they form rifted margins. The deformation processes leading form a moderately extended margin to a highly stretched margin are still unclear (Ranero and Pérez-Gussinyé, 2010), and several models have been made to explain the formation of magma poor passive margins. Present day rifted margins vary in their appearances especially in width of the necking domain (Sutra and Manatschal, 2012).

The formation of these margins has been explained with both simple and pure shear. Those in favour for a pure shear model (e.g. Le Pichon and Sibuet, 1981) depend mostly on the thermal history and associated subsidence, while the simple shear model (e.g. Wernicke, 1985) generally refers to the asymmetric structures (Brun and Beslier, 1996). The best models for hyperextended passive margins use both offshore data and onshore analogues (Andersen *et al.*, 2012), like for example Manatschal (2004) with a model from the Alps. Hyperextended margins tend to be a wide transitional area with diffuse continental or oceanic affinities, rather than an abrupt (Pérez-Gussinyé, 2013).

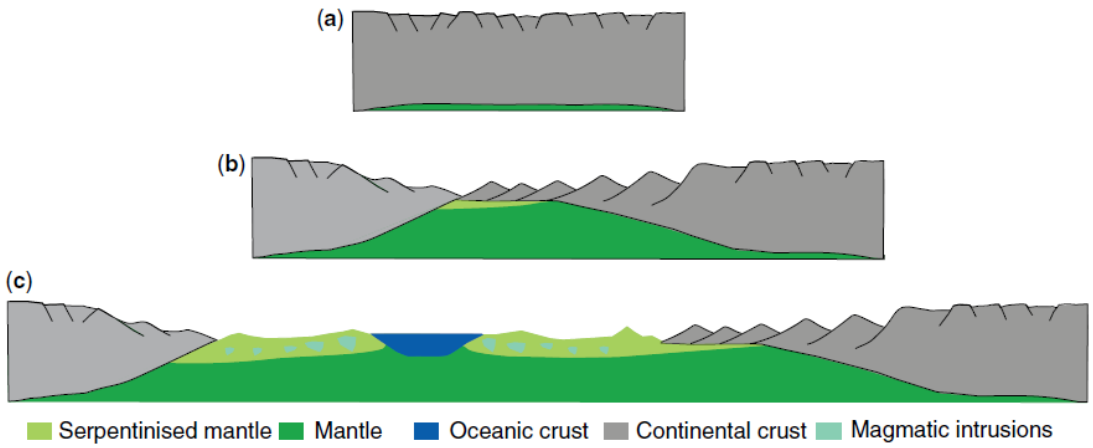

Fig. 3.2A-C: A cartoon showing the principles of magma poor hyperextension of continental crust. A) Little crustal thinning and active faults distributed over a large area, with no discrepancy between crustal thinning and horizontal extension on the faults. B) In this stage a clear asymmetric shape has developed. On the right side there are large scale faults with rotated blocks and a gradually shallowing of the Moho and the left side show little faulting and an abrupt thinning of the crust. This stage the faults change from planer to listric, and then to detachment-like faults with increasing extension. The margin stage has a discrepancy between the amount of crystal thinning and the extension measured. C) The final stage of the extension with exhumation of the mantle at the COT. From Pérez-Gussinyé (2013)

Fig. 3.2A-C shows a cartoon with the basic principles of the formation of hyperextended margins and to the development of oceanic crust at three selected stages. Fig. 3.3A-R shows a more complex and detailed model of the formation of these margins and is based on the western margin of Iberia and the conjugate Newfoundland margin, which is one of the best studied pair of hyperextended margins (Pérez-Gussinyé, 2013), and is typical of highly extended non-volcanic margins. Ranero and Pérez-Gussinyé (2010) and Pérez-Gussinyé (2013) suggested that the transition from continental crust with a thickness of ca. 20 km to exhumation of mantle involves several major faults (f1-f7, fig. 3.3A-R), developed at favourable strain locations. The faults are form with an angle of ca. 65-55^{o}, relative to the pre-rift strata, and is rotated to ca. 42-28^{o} as the system develops, through slipping and further thinning (Pérez-Gussinyé *et al.*, 2003). As the extension progresses, faults grow and link up laterally. The focus of the extension is in the basin-dipping faults in the basin centre, while the faults in the basin flanks are progressively abandoned (Cowie *et al.*, 2005). The two first faults (f1 and f2) appear to become listric at depth, while f3-6 merge into the S detachment at the crust-mantle interface. The last fault (f7) is completely back-rotated and

exhibits a very shallow angle (fig. 3.3R) (Pérez-Gussinyé, 2013). When a fault becomes inactive, a new fault forms in the hanging wall, e.g. f1 and f2. Slip and rotation of the new fault change the deeper segment of the previous fault changing the geometry from planer to listric, and the inactive faults are passively rotated to lower angles. Rupture and separation of the continental crust and successive mantle exhumation happens after the last fault (f7) become inactive (Pérez-Gussinyé, 2013).

As the system progresses, the lower crust become progressively more brittle and is cut and exhumed by the overlaying faults as the extension progress (Pérez-Gussinyé, 2013). The embrittlement of the lower crust allows seawater to reach the mantle through the fault systems. This then leads to hydration (serpentinization) of the upper mantle (Pérez-Gussinyé, 2013). Since serpentine are very weak, the hydration of the mantle acts as stress guides further focusing the extension, so the exhumation of mantle occur just after crustal embrittlement and serpentinization (Perez—Gussinyé and Reston, 2001). Seismic images from the Galicia Interior basin (Pérez-Gussinyé *et al.*, 2003) show that the faults in the platform are planer and do not cut through the entire crust. As the extension progresses the faults become listric and cut deeper into the crust. This suggests that the lower crust at the start of the extension is ductile and that embrittlement occur during progressive extension (Pérez-Gussinyé, 2013).

Perez—Gussinyé and Reston (2001) have suggested that hydration of the upper mantle may be responsible for the exhumation of mantle rocks to the surface due to the increasing buoyancy due to the volume change during serpentinization.

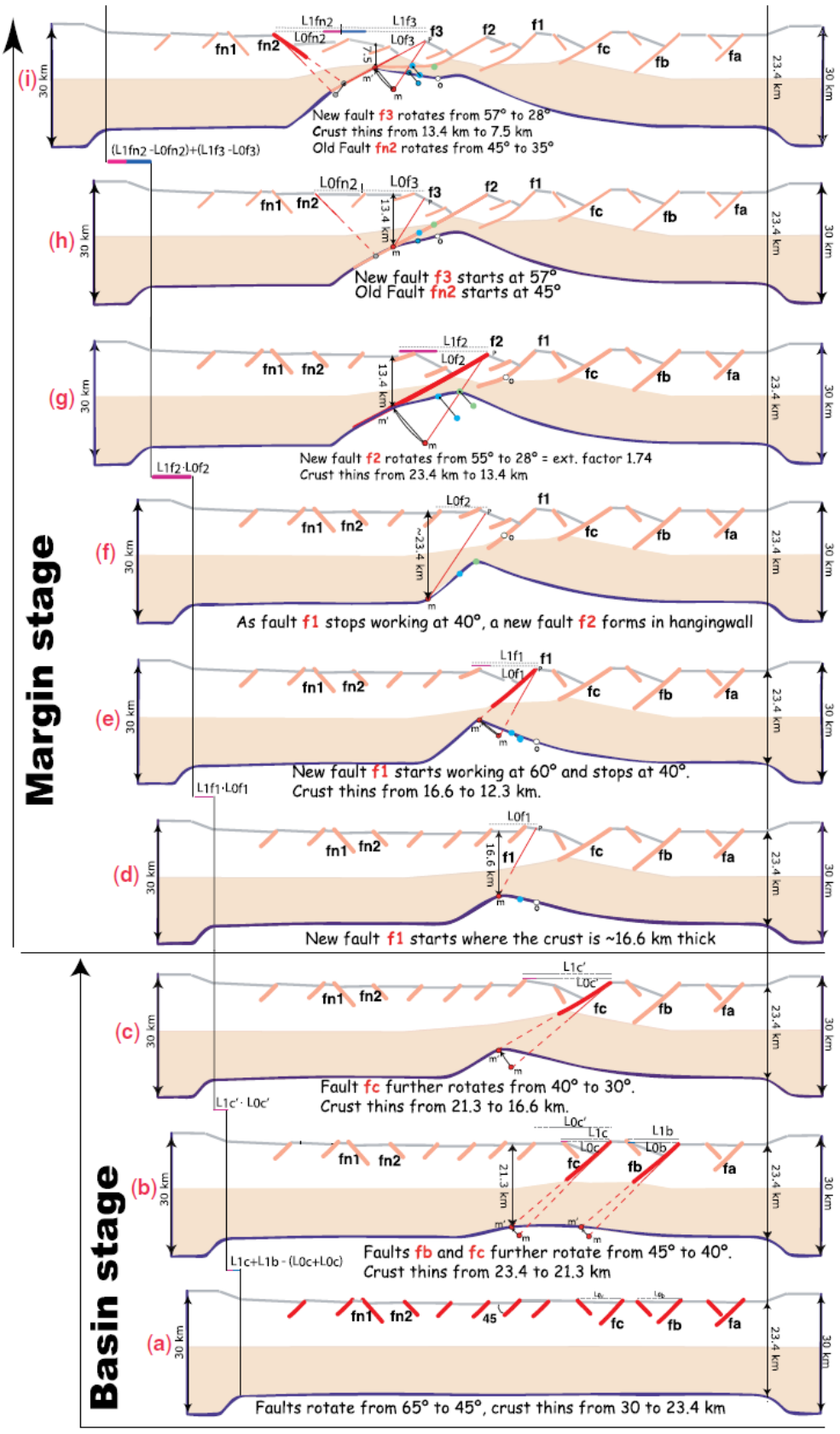
Margin stage
Basin stage
(i)
(h)
(g)
(f)
(e)
(d)
(c)
(b)
(a)
30 km
23.4 km
fn1
fn2
f3
f2
f1
fc
fb
fa
L1fn2
L0fn2
L1f3
L0f3
7.5 km
13.4 km
~23.4 km
16.6 km
21.3 km
L1f2
L0f2
L1f1
L0f1
L1c'
L0c'
L1c
L0c
L1b
L0b
45
(L1fn2 -L0fn2)+(L1f3 -L0f3)
L1f2·L0f2
L1f1·L0f1
L1c'· L0c'
L1c+L1b - (L0c+L0c)
New fault f3 rotates from 57° to 28°
Crust thins from 13.4 km to 7.5 km
Old Fault fn2 rotates from 45° to 35°
New fault f3 starts at 57°
Old Fault fn2 starts at 45°
New fault f2 rotates from 55° to 28° = ext. factor 1.74
Crust thins from 23.4 km to 13.4 km
As fault f1 stops working at 40°, a new fault f2 forms in hangingwall
New fault f1 starts working at 60° and stops at 40°.
Crust thins from 16.6 to 12.3 km.
New fault f1 starts where the crust is ~16.6 km thick
Fault fc further rotates from 40° to 30°.
Crust thins from 21.3 to 16.6 km.
Faults fb and fc further rotate from 45° to 40°.
Crust thins from 23.4 to 21.3 km
Faults rotate from 65° to 45°, crust thins from 30 to 23.4 km

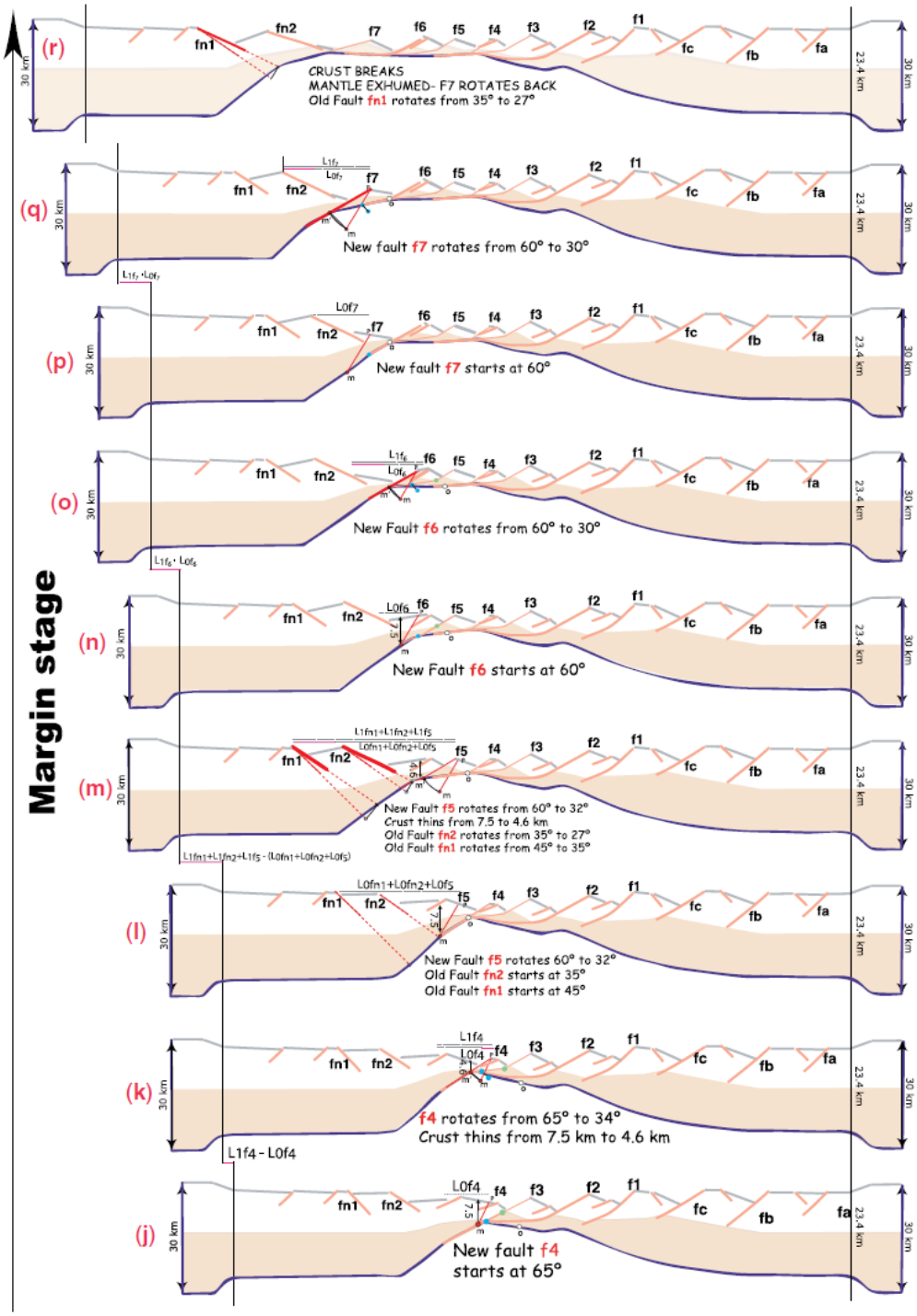

Fig. 3.3A-R: A model showing step by step development of a hyperextended margin based on the "sequential faulting" model, based on the Western Iberian margin. The model show the how the crust is gradually thinned by the development of the fault system and how these margins have an asymmetric appearance. The model is fixed on the right side. Red and orange lines show active and inactive faults. Dashed red lines show projections of the fault plane into the ductile part of the crust. The blue line shows the Moho. From Pérez-Gussinyé (2013). See also Ranero and Pérez-Gussinyé (2010)

Hyperextended margins are now beginning to be recognized as a common extensional mode (Pérez-Gussinyé, 2013). Present day hyperextended margins include:

- The Norwegian Sea margin (Osmundsen and Ebbing, 2008)
- The Red Sea (Cochran and Karner, 2007)
- South Atlantic (Contrucci *et al.*, 2004)

3.3 Alteration and serpentinization of peridotites

Present day hyperextended margins are commonly underlain with a high velocity lower crustal body, and Lundin and Doré (2011) argued that this is the result of a partially serpentinized upper mantle. Partial serpentinization at passive margins has been linked to severe crustal extension. If the crust reach sufficient thinning the remaining upper and lower crust is embrittled, which allow faults to cut the crust and water to reach the mantle. Embrittlement occurs at a crustal thinning factor of 3-4, given an assumed initial crust thickness of 30-35 km (Lundin and Doré, 2011).

Most metamorphosed alpine type peridotites fits well into the CMS-H (CaO-MgO-SiO_2-H_2O) system. Peridotite contains olivine, orthopyroxene and clinopyroxene with variable proportions. When a peridotite is exposed to hydrous conditions below 500^{o}C, olivine and pyroxene is serpentinized. Ultramafic rocks affected by low-grade metamorphism are dominated by serpentine minerals (lizardite, chrysotile and antigorite). Lizardite and chrysotile occur in low grade serpentinites, while antigorite tend to occur in somewhat higher temperature metamorphism (Winter, 2014). During the metamorphism excess iron is incorporated into magnetite (Winter, 2014) and adjacent rocks undergo Ca-metasomatism and rodingitization (Austrheim and Prestvik, 2008).

Peridotites undergone greenschist metamorphism tends to be almost pure serpentinites, along with brucite, diopside and magnetite. At higher temperatures (ca. 400^{o}C) antigorite and brucite breaks down into secondary olivines. Secondary olivine formed by prograde

metamorphism of serpentine tends to be more Mg-rich then the original peridotitic olivine. This is because the Fe is taken up in magnetite during early serpentinization (Winter, 2014).

Soapstones

Soapstones are ultramafic rocks consisting of dominantly talc and magnesite (or dolomite). They form the interaction between ultramafic bodies and externally derived CO_2-H_2O fluids (Bucher and Grapes, 2011). Eq. 1 shows the transformation of serpentinites to soapstone by interacting with CO_2:

Serpentinite + 3 CO_2 → Talc + 3 Magnesite/breunnerite (Eq. 1) (Sanford, 1982)

3.4 Ultramafic rocks in the Scandinavian Caledonides

The metaperidotites in western Norway are found in two main associations: the WGR and within the Caledonian nappes (Qvale and Stigh, 1985). The peridotites in the WGR have experienced (U)HP metamorphism during the Caledonian orogeny (e.g. Van Roermund and Drury, 1998). They are associated with the Proterozoic gneisses of the WGR and occur in the most felsic gneisses in the north-western parts of the WGR (e.g. van Roermund, 2009). The origin(s) of these peridotites is debated, but the most commonly used interoperation is that they derived from the mantle wedge during the subduction of Baltica below Laurentia during the Scandinavian orogeny (Andersen *et al.*, 1991). Some peridotites occur as cumulates in the ophiolite complexes, such as Karmøy and Gullfjellet ophiolite complexes (Qvale and Stigh, 1985; Dunning and Pedersen, 1988)

Other occur as solitary “Alpine-type”, also called orogenic type, peridotites in the regional mélange unit, that has been mapped from the Bergen area and north-eastwards across southern Norway, as far as the Vågå-Otta area, a distance of more than 400km (Andersen *et al.*, 2012), see fig. 2.2. From Otta and towards the Røros area, no mélange is found between the Lower and Middle Allochthon. There are ultramafics in this area, but they are found in the Upper Allochthon, and they are found along with gabbros (Nilsson and Roberts, 2014).

The “Alpine type” peridotites are the most common type of ultramafics in the Scandinavian Caledonides. “Alpine-type” peridotites are on several places associated with clastic ultramafic rocks (Qvale and Stigh, 1985), which also occur in Stølsheimen (see below).

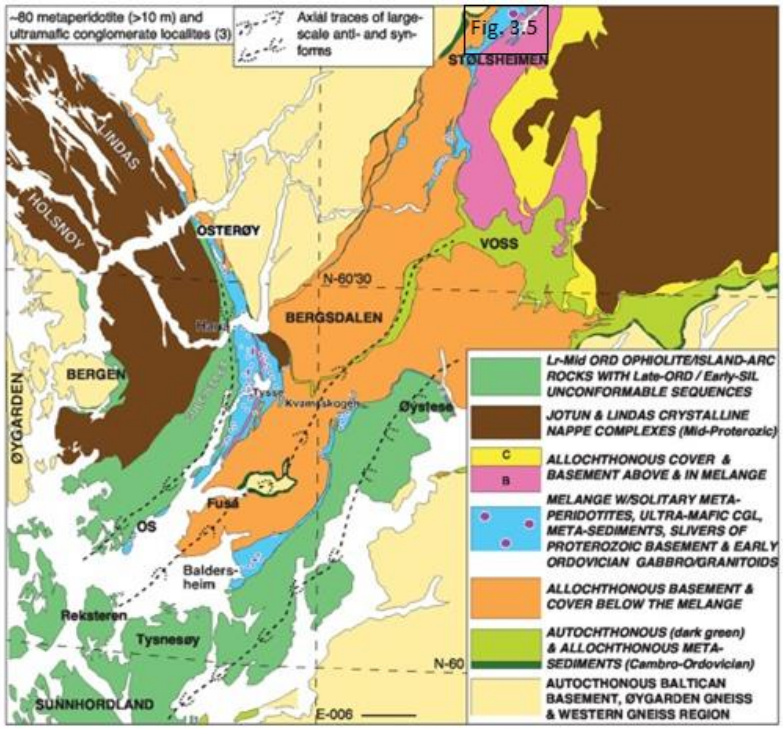

Fig. 3.4: The mélange unit (blue) with solitary peridotites in Western South Norway, from Bergen in west and up to Stølsheimen, and adjacent Caledonian Nappes. The unit is semi-continuous from Osterøy, down to Os and Baldersheim, and then north again towards Stølsheimen. See also figure. 3.5. Andersen (2015, unpublished).

The study area described in this thesis is a part of the peridotite bearing mélange unit that occurs between the Lower and Upper Bergsdalen Nappes, structurally below the Jotun Nappe (Andersen *et al.*, 2012)(fig. 3.4 and 3.5).

The metaperidotites in the mélange unit has been altered through hydration processes, and are today found mostly as serpentinites, but also as talcschists and soapstones (Karlsen, 1990; Andersen *et al.*, 2012). The largest ultramafic bodies are up to 2km in size, but most of them are found as lenses less than 100 meter across. The best preserved bodies still contain some primary minerals (Andersen *et al.*, 2012). The Raudberget and Vetle Raudberget metaperidotite bodies in Stølsheimen are described in detail by Enger (work in progress). The matrix envelope of the ultramafics is dominated by metasediments recrystallized into graphitic schists, garnet schists, mica schists and phyllites. The Caledonian metamorphism reached upper greenschist to lower amphibolite facies (Andersen *et al.*, 2012).

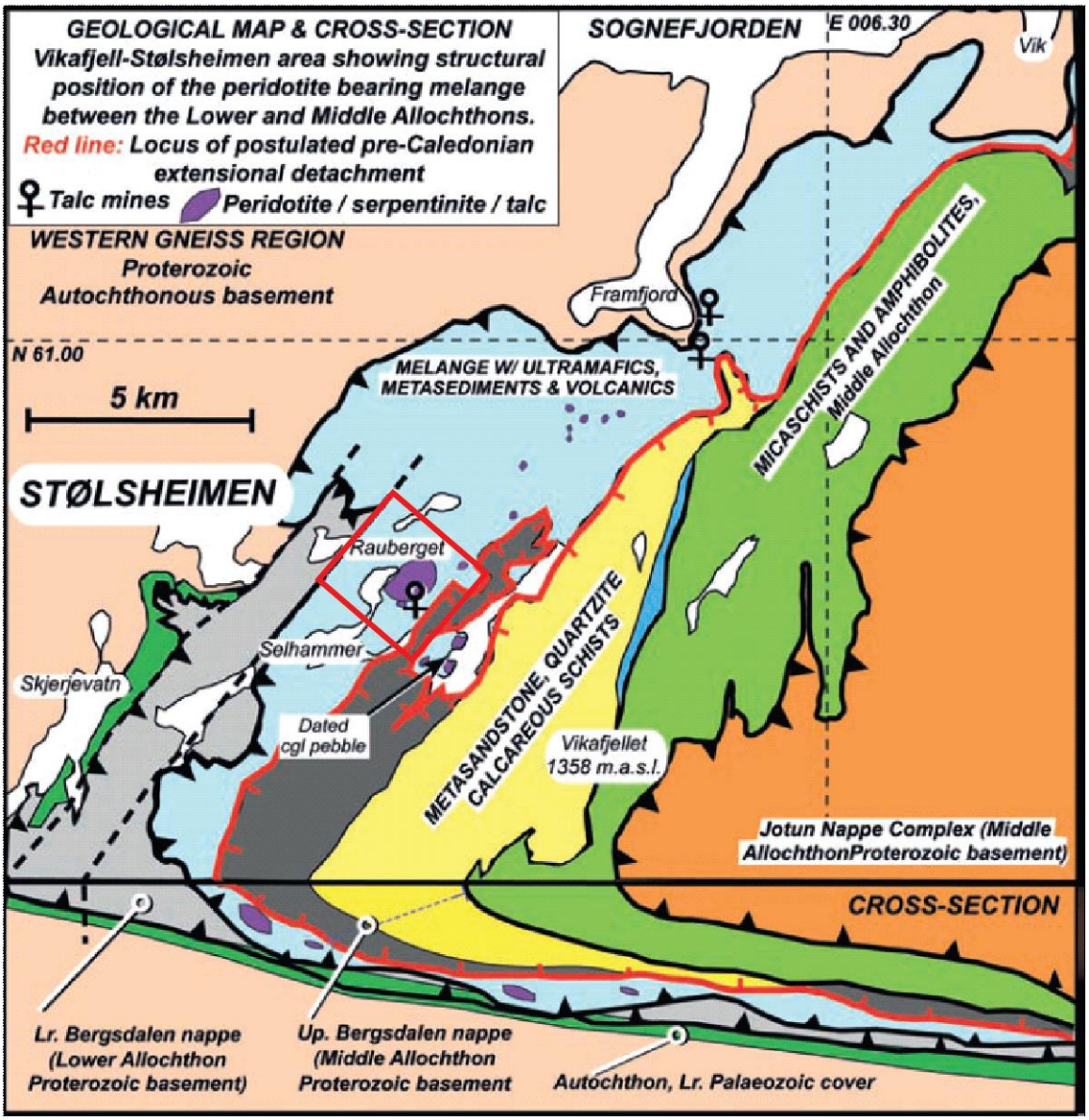

Fig. 3.5: Geological map with cross-section showing the stratigraphical positioning of the mélange unit in the Stølsheimen region. Notice that the mélange unit is structurally positioned between the Lower and Upper Bergsgalen nappes. These nappes are apparently discontinues and taper out north of the study area. Study area marked with red. Map from Andersen et al. (2012).

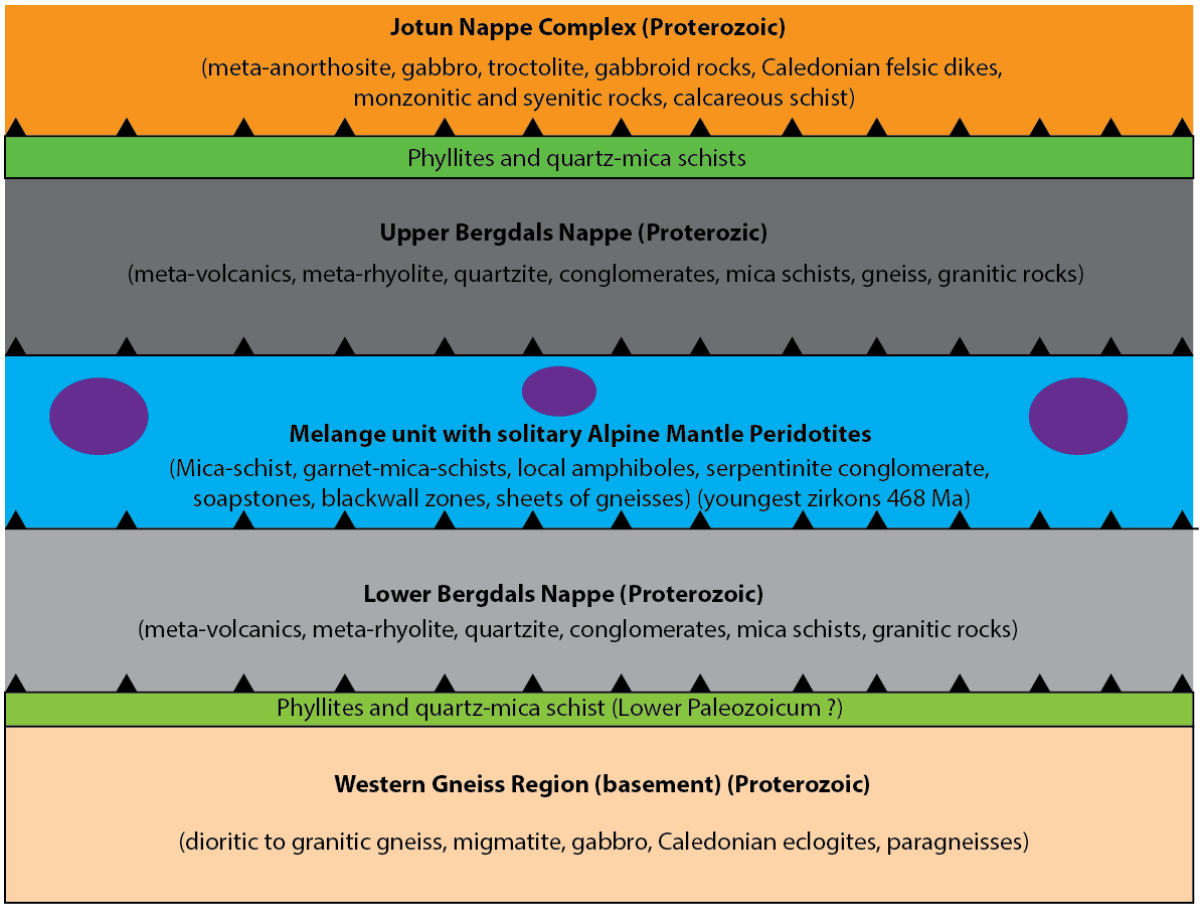

Fig. 3.6: Simplified tectostratigrahic cartoon showing the different nappes in the western parts of southern Norway. The Western Gneiss Region as the lower most unit, followed by the Lower Bergsdalen nappe. Between the Lower and Upper Bergsdalen nappes is the mélange unit with solitary peridotites in a matrix of largely metasediments. The Jotun Nappe Comples as the uppermost unit in this area. Units not to scale. From Enger (work in progress).

4. Methods

A selection of samples from the fieldwork where chosen for further analyses. The samples were chosen to get a good representation of the different lithospheric units in the mapped area. The methods used in this thesis are: optical microscopy, x-ray fluorescence (XRF) and the electron microprobe (EMP). In addition *Stereonett 7* with equal area projection is used for organising structural data, recorded in the field. In total 20 samples was selected for thin sections, with some of the thin sections was studied in the electron microprobe.

A standard optical microscope was used to examine and describe thin sections of the lithologies in the study area. The microscope was also used to find areas of interest for examination in the EMP.

The EMP was used to investigate the composition of the main rock forming minerals. It was also used to make element map of selected garnets from the garnet micaschist found in the study area. Bulk rock composition of selected samples from the XRF was used together with *Theriak-Domino* (de Capitani and Brown, 1987; de Capitani and Petrakakis, 2009; de Capitani and Petrakakis, 2010) to determine peak metamorphic conditions during the Caledonian collision.

All geochemical analyses were done at the Department of Geosciences, University of Oslo.

4.1 Field equipment

The main part of the field work was carried out in the summer of 2014, with some additional field work in the summer of 2015. In the field a Garmin GPSmap 62s was used in combination of topographic maps (1:250 000 scale) downloaded from geo.ngu.no/kart/berggrunn, to make a field sketch of the area. The finished geological map was then digitalized in *Arcgis* on the basis of the field sketch together with coordinates taken with the GPS. Cross-sections was made using *Adobe Illustrator*.

Strike and dip measurements was taken with a Silva expedition S clinometer compass. The right hand rule was applied when the measurement was taken.

4.2 Sample preparation

4.2.1 Glass beads

Six of the samples chosen for thin sections were also selected for a major element analyses using XRF. These samples were crushed in a jawbreaker until the crushed fragments had a maximum size of 0,5 x 0,5 cm in area. Before the samples were crushed a seventh sample with similar mineralogy was sent through the jawbreaker to reduce the risk of contamination from other samples. This sample was not used for the analyses.

The six samples were then pulverized in a steel mill until the grain size was down to 100-200 µm. The samples were then dried for a couple of days in an oven at 120^{o}C to remove all non-structural water that may be present in the sample.

To determine the amount of structural water in the rocks, the samples were run through a process called loss on ignition (LOI). In this process the samples are heated to 1050^{o}C and left for about 70 minutes. The high temperature oxidises the samples and all the fluids (H_2O and CO_2) evaporate. The samples were weighted before and after the process. Comparing the two numbers give the amount of fluids that was present in the minerals in the samples. The amount of fluids is then used when calculating the bulk composition of the sample.

The samples were then mixed with a flux made of lithium borate and melted into glass beads to ensure a homogeneous sample and reduce secondary fluorescence. The mix ratio that was used was 6,000 gram flux and 0,6000 gram sample in each bead. The sample and flux was mixed in a crucible made of platinum, and then melted at 1275^{o}C.

4.3 Basics of XRF and the EMP.

Both the XRF and the energy dispersive X-ray spectroscope (EDS) on the electron microprobe use the electron configuration in atoms through characteristic x-rays and Bragg's law for the analyses of the sample.

An atom is consist of a positively charge core of protons and neutrally charged neutrons, surrounded by negatively charged electrons. These electrons are grouped in shells or energy levels. The lowermost shell is called the K-shell, followed by L-shells, M-shells and so on. The L-shells are divided into three sub shells (L_{I-III}) and the M-shells into five (M_{I-V}). The number of electrons in the different shells varies. The K-shell can hold two electrons, the L-shells can hold a total of eight electrons and the M-shells a total of 18 electrons. The energy levels in the different shells are unique for each element (e.g. Brouwer, 2003).

When an atom is exposed to irradiation, such as electrons from the EMP and x-rays from the XRF, with sufficient energy, electrons may jump to a higher shell or be removed from the atom all together. Since the atom strive to keep a lowest possible energy configuration, an atom from a higher energy level take over the vacant position. For example is an electron from the K-shell is removed by the incoming irradiation, it can be replaced by an electron from one of the L-shells. The left-over energy is released as a photon with a specific wavelength or energy level. Since the energy level in the different shells are unique to each element the wave length of the photon is unique to the element, hence the name characteristic x-rays (Brouwer, 2003).

The wavelength dispersive X-ray spectroscopy (WDS) uses an analysing crystal to disperse the different wave lengths from the photons. The incoming radiation gets reflected of the crystal after the parameters given in Bragg's law:

$$n \cdot \lambda = 2 \cdot d \cdot \sin(\theta) \quad \text{(Eq. 2)}$$

Where n= order, λ= wavelength, d= the space between the different layers in the crystal (d-spacing) and θ= angle of the x-rays. Only the incoming radiations that obey this law are reflected of the crystal and towards the detector. Different crystals with varying d-space are used for different elements, according to the wavelength in their characteristic x-rays (Brouwer, 2003).

4.4 XRF

XRF is a non-destructive analytical method used to determine the chemical composition of a sample using x-rays. X-rays covers the range between 0,01nm and 10nm in wavelength in the electromagnetic spectrum. The X-rays are produced in an X-ray tube by a current that is sent through a filament heating it up to the point where it starts releasing electrons. The electrons are then accelerated by an area of high voltage (20-100kV) towards an anode. When the electrons hit the anode they decelerate and the extra energy is released as x-rays. The x-rays then leave the tube through i.e. a Be-window towards the sample. Between x-rays then go through a filter on the way to the sample. The filter is there to improve the signal-to-noise ratio by reducing the ratio of interfering lines and background radiation. The machine used during the analyses use a WDS spectrometer as explained above (Brouwer, 2003).

4.5 Electron microprobe

The EMP is a non-destructive method used to take spot analyses (10 µm) of the chemical content in a sample, e.g. thin-section. An electron gun fires a beam of electrons towards the sample. The interaction between the sample and the electron been produce three effects used by the microprobe: characteristic x-rays, backscattered electrons and secondary electrons. Backscattered electrons are electrons from the electron beam reflected of the sample. This used to make black and white images of the sample, where the different grey shades give the reflective value. Lighter shades have a higher reflective value and indicate heavier elements. Secondary electrons are electrons removed from the sample and are used in the energy-dispersive spectrometer (EDS).

The EMP has two ways to analyse the sample, WDS and EDS. The WDS spectrometer was used to make an accurate analysis of a given mineral crystal, while the EDS produces a spectrum which was mainly used to give a quick overview of the chemical elements and as an identification of mineralogy.

A CAMECA SX 100 microprobe was used for the analyses. The acceleration voltage was set to 15 keV and a beam current of 15 nA, except for the element mapping of the garnets where 30 keV was used. The peak count time was set to 10 seconds. Table 4.1 gives the

Elements (in weigh% oxide) analysed in the EMP	
SiO_2	TiO_2
NaO_2	FeO
$Al2O_3$	MnO
K2O	MgO
CaO	Cr_2O_3

Table 4.1: Elements analysed in the EMP. NiO was added for samples close to the ultramafics.

selected oxides for the EMP analyses. For the samples taken close to the meta-peridotite bodies Ni was added to the analytical procedure.

The oxide wt% was then recalculated into cations. This was done with the help of an *Excel* spreadsheet made by López-Carmona and Segovia-Diaz (2015)

A separated spreadsheet was used for the amphibole formula calculation. This spreadsheet is made by Preston (2015). The spreadsheets take the oxide weight percent and recalculate them into cations per formula unit by the standard methods, normalized on a given number of oxygen atoms. The number of oxygen's used for the different minerals is given in table 4.3. In addition to give the number of cations, the amphibole spreadsheet gives the name of the amphibole based on the chemical content. This is done by looking at the amount of the different cations and their position in the crystal lattice. The spreadsheet differentiates between 39 different amphiboles.

Table 4.2: Standard calculation method for cations from oxide wt%. Brady (2015)

Standard calculation of cations from wt %
1) Divide the wt % of each oxide by the formula weight of the specific oxide (Table 4.5)
2) Multiply the resulting "mole number" with the number of oxygen in the oxide formula
3) Multiply the resulting "oxygen number" of each oxide by a normalization constant (given by the number of oxygen desired in the formula divided by the sum of "oxygen numbers")
4) Multiply the "normalized oxygen numbers" of each oxide with the number of cations per oxygen in the oxide formula

The EMP was also used to make element maps of garnets. The five spectrometers on the microprobe were set to scan for: AlO, CaO, MgO, FeO and MnO. This was done to look for chemical zoning in the garnets. In addition to the element mapping, profiles of three garnets were made by analysing points throughout the crystal. This was done to make a quantitative plot of the element distribution.

Table 4.3: Number of oxygen atoms used for the calculation of cations from wt%

Mineral	Oxygen	Mineral	Oxygen	Mineral	Oxygen
Amphiboles	23	K-feldspar	8	Epidote	12,5
Biotite	11	Muscovite	11	Talc	22
Chlorite	28	Plagioclase	8	Garnets	12

4.6 An introduction to *Theriak-Domino*

In order to determine peak metamorphic conditions during the Caledonian orogeny in the study area a program called *Theriak-Domino* was used together with bulk rock composition from the XRF.

A detailed description of the inner workings of *Theriak-Domino* is given by de Capitani and Brown (1987), de Capitani and Petrakakis (2009) and de Capitani and Petrakakis (2010). Here follows a short description of the software based on these articles and documentation in the program suite.

Four of the most popular programs used by petrologists are: *THERMOCALC*, *Perple_X*, *Gibbs* and *Theriak-Domino*. One of the benefits with *Theriak-Domino* is that the program does all the calculations and that the graphical representation of the data is done automatically by the software.

Theriak-Domino is a program package written by Christian de Capitani. The program use as standard a database called JUN92D for the calculations. The database contains phase definitions and information used to calculate Gibbs free energy for variable temperatures and pressures. The database also contains definitions of solutions and solution models, along with fixed composition solution phases and Margules parameters for non-ideal solution phases (de Capitani and Petrakakis, 2009). Other databases can be used but they require the right format to be used as an input.

Note that for sample 65-14 omphacites was removed from the standard database. This was done because the sample does not contain these minerals, but with the standard database omphacites was found in most mineral assemblages in the *P-T* conditions used. Minerals

can be removed from/made inactive in the database by changing the code involving the desired mineral to a comment. In the JUN92D database this is done by adding a "!" as a prefix in the code. H_2O was removed from the finished diagrams due to it being stable at all mineral assemblages.

The program package consists of 10 programs, where *Theriak* and *Domino* are the two most important:

***Theriak*:** *Theriak* is the heart of the equilibrium assemblage calculations. Given a bulk-rock composition the program calculates the mineral equilibrium assemblages at any *P* and *T* or along a *P-T* path. *Theriak* is designed to produce correct mineral assemblages even for non-ideal and complex systems. The program provides a theoretical mineral assemblage based on Gibbs free energy minimisation for a given bulk rock composition *P-T* conditions using the database(s), which are derived from experimental and empirical data. Because the current databases are not perfect, the mineral assemblages given by *Theriak* is somewhat simplified.

***Domino*:** *Domino* calculates the equilibrium assemblage diagrams. It can also calculate pseudo-binary and pseudo-ternary diagrams, pixel maps of thermodynamic variables and isolines for bulk-rock, mineral and solution properties. The expressions pseudo-binary and pseudo-ternary are used for diagrams that show two or three variables in the bulk-rock chemical composition. The diagrams produced by *Domino* are based on predicted stable mineral assemblages based on Gibbs free energy minimization. Since *Theriak-Domino* use bulk-rock composition to calculate the equilibrium diagrams, the calculations are only valid for the specific composition, in contrast to the classical petrological grids.

Table 4.4: Programs in addition to Theriak and Domino in the program suite and their tasks. From de Capitani and Petrakakis (2010)

Other programs in the *Theriak-Domino* program suite and their tasks	
Therbin	Calculates binary phase diagram at constant *P* or *T*
Therter	Calculates ternary phase diagrams at constant *P* or *T*
Tahilia	Calculates phase thermodynamic parameters as functions of *P* or *T*

Thermo	Calculates thermodynamic parameters at *T* and *P* and tables of V (volume) or G (Gibbs free energy)
Guzzler	Use the output from *theriak*, *domino* or *thalia* and makes the graphics more readable by cleaning up labels. (Used in this thesis)
Explot	Takes the diagrams from the other programs and convert them into .ps (PostScript) files readable in most graphic handling programs. (Used in this thesis)
Makemap	Takes the pixelmap information made by domino and incorporates a grey pixelmap image into a .ps file and a portable grey mapfile
Plotxy	Takes the thermodynamic variables included in a multi-step calculation and prepares plots of XY diagrams

4.6.1 Mole calculation

Three of the samples that were chosen for XRF where run through the *Theriak-Domino* software package for thermobarometric analyses. First the weight percent of the elements in the samples, given by the XRF-analyse, was recalculated to moles and normalized to 100, using the oxide weights given in table 4.5. The mole value for the different elements was calculated by the two formulas:

Mole units = (Oxides wt % from XRF x number of cations in oxide) / oxide wt% gfw (Eq 3)

$$\text{Mole proportions} = (100 / \text{mole units}_{tot}) / \text{mole units}_{element} \quad \text{(Eq 4)}$$

Oxide	Oxide wt gfw	Oxide	Oxide wt gfw
SiO_2	60,08	V_2O_5	181,88
TiO_2	79,87	Cr_2O_3	151,99
Al_2O_3	101,96	SrO	103,62
Fe_2O_3	159,69	ZrO_2	123,22
Mn_3O_4	70,94	BaO	153,33
MgO	40,30	NiO	74,69
CaO	56,08	CuO	79,55
Na_2O	61,98	ZnO	81,38
K_2O	94,20	PbO	223,20
P_2O_5	141,94	HfO_2	223,20
SO_3	32,06		

Table 4.5: Oxide wt gfw used for calculation of mole fraction and number of cations.

After calculation the bulk composition into moles, *Domino* was first used to calculate stable mineral assemblage for the different bulk compositions. Previous works (see below) was used to reduce the pressure and temperature range of the diagrams.

4.6.2 Geochemistry in *Theriak-Domino*

Domino was then used to calculate garnet end member diagrams and Si in white mica (SIPFU), to better define the peak pressure and temperature. The garnet end members that were used for this is: almandine, pyrope and grossular. The garnet plots were then used to look for parts of the plot where all three end member overlap each other, giving the most likely peak metamorphic conditions.

The mineral equilibrium is the standard calculation for *Domino*. To calculate solution phases the setup need to be changed. Non-solution phase commands can be calculated for several minerals and the input commands are the same (see below).

4.6.3 Step by step calculations using *Theriak-Domino*

1) Type in the mole calculation of the bulk rock composition in *Therin*
2) Start the program suite
3) Select *Domino*
4) Select database
5) Select minimum and maximum temperatures for the plot
6) Select minimum and maximum pressure for the plot
7a) For calculation of standard mineral equilibrium:

    Type "."

7b) For calculation of non-solution phases:

    Standard input: (Phase) Key (Nr) Min Max Step, with two spaces between the inputs

    - Example almandine end member composition between 60-80% with 2% steps: Garnet alm 1 0.6 0.8 0.02

8) Run *Guzzler*
9) Run *Explot*

5. Description of mapped units

Here follows a description of the different lithologies found in the study area as seen in appendix 1. A map showing the sample localities used for geochemistry analyses is given in appendix 2, with an overview of what the different samples have been used for in appendix 3. The results of the XRF analyses are given in appendix 4, with and without recalculation for LOI. Appendix 5 lists the mineral chemistry of the different samples from the EMP.

5.1 Ultramafics

The ultramafic bodies in the study area are only briefly described here. For a detailed description of the mineralogy and geochemistry, see Enger (work in progress).

There are two major ultramafic bodies in the field area, Raudberget and Vetle Raudberget, with Raudberget been the larger of the two. In addition there is a third ultramafic body below the surface at Bjørnshaugen. Raudberget is approximately 1,5 x 0,9 km in size and stands 160 meters above the surrounding terrain. Vetle Raudberget is on the other hand a much smaller outcrop located in the eastern part of the study area. The exposed parts of Vetle Raudberget are approximately 450 x 150 meters, with a maximum height of ca. 20 meters relativity to the surroundings. With the exception of blackwall altered schists (see below) in the transition between the ultramafics and the surrounding lithologies, no contact metamorphism between the ultramafic bodies and the surrounding matrix has been found. This is supported by the finds of Andersen *et al.* (2012).

Raudberget has two distinct colour variations on weathered surfaces, the lower part of the mountain have a brown and grey colour, while the upper parts have a brighter red to orange colour. The surface colour is ca. 1cm deep and on freshly exposed surfaces rock have a dark green colour.

The ultramafic bodies have three distinct textures; smooth, rough and brecciated. Raudberget is intensely fissured, without a dominating directional trend. Veins of different minerals are found in different parts of the hill, for example serpentine veins shown in fig. 5.1D. Fig. 5.2 shows the different surface textures as mapped by Enger (work in progress).

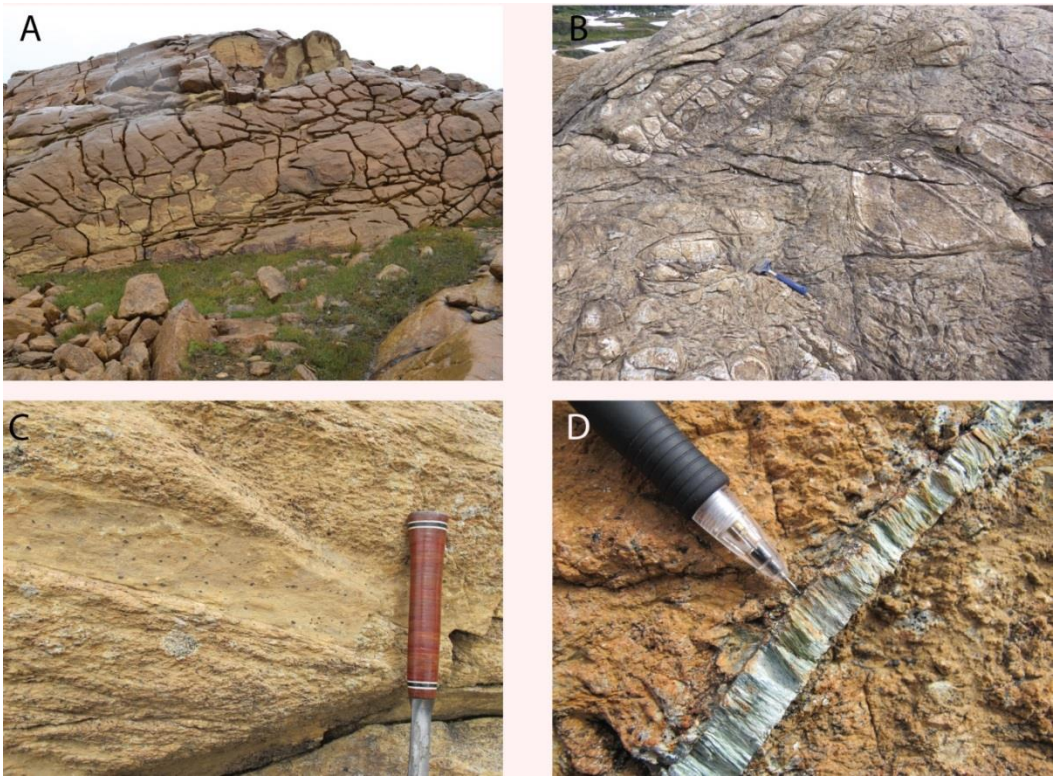

Fig. 5.1A-D: Textures of the Raudberget metaperidotite. A: Fissure system without a domination direction on top of Raudberget (photo Anders Enger). B: Serpentine breccias (photo Anders Enger). C: Fine and curse grained texture of Raudberget. D: 1cm thick serpentine vein in Raudberget.

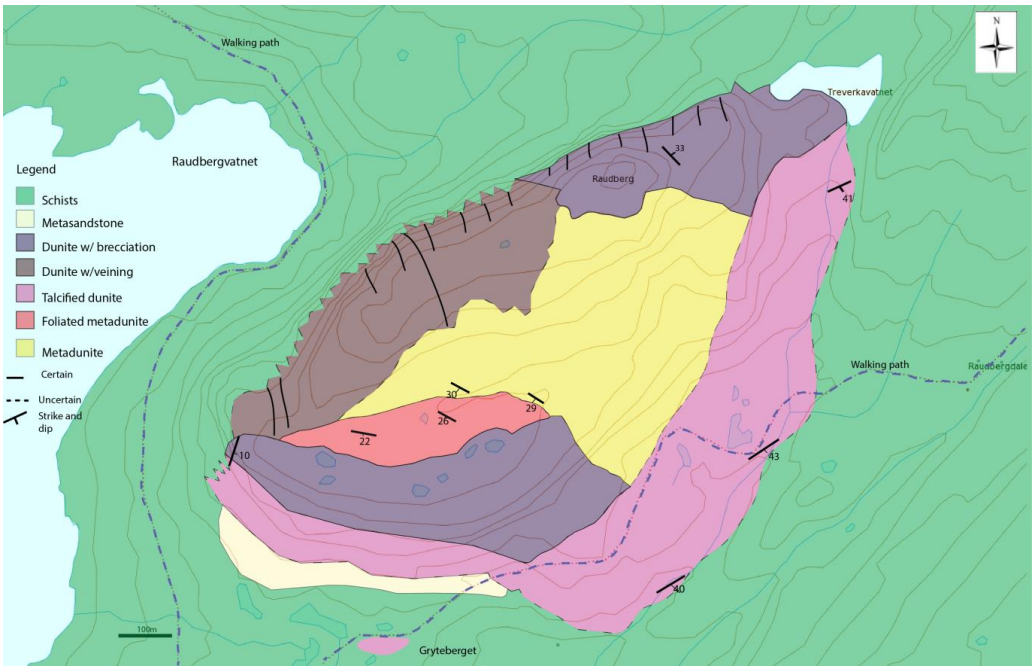

Fig. 5.2: Detailed map over Raudberget with the different zonation, with a dunitic and metadunitic centre and a talcifed dunite along the rim of the body. Also note the talcifed dunite/soapstone body of Gryteberget. From Enger (work in progress)

There are other smaller ultramafic bodies found outside the study area as shown by fig. 6.4. Some of these were visited during the field work, and it seems that they are highly exaggerated in scale on the map.

5.1.1 Serpentine conglomerate

On the east side of there is a serpentine conglomerate, which has been quarried and used in the construction of the hydroelectric dams in the area. During the field work the water level in Kvilesteinsvatnet was too high to see the conglomerate *in situ.* Fig. 5.3A and B is taken by Torgeir Andersen at an earlier occasion and shows the conglomerate as it is found today, when the water level is low enough. The conglomerate consists of clasts of serpentine in a serpentine matrix. There is also some (meta)sandstone and quarzitic horizons in the conglomerate.

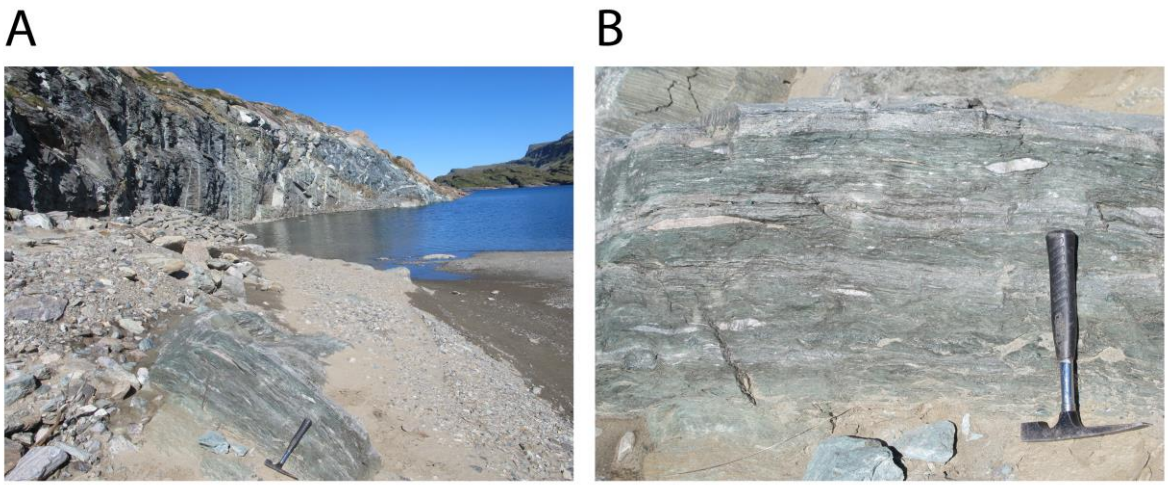

Fig. 5.3A: Serpentine conglomerate as it is found today, notice that the ultramafic conglomerates have been quarried. At normal water level the lithology is not accessible, but nice samples of the conglomerate can be studied in blocks used in the hydroelectric dams. B: Close up photo of the conglomerate, with serpentine clasts in an green serpentine matrix with some (meta)sandstone layers. Hammer for scale. Photos by Torgeir Andersen

5.1.2 Transitional zones

Between the ultramafics and the surrounding metapelites there are different examples of transitional rocks. Fig. 5.4 shows a layer of talc schists found underneath Gryteberget, a small soapstone body found a few meters south of Raudberget. The talc schist has a weak greenish tint layers with white quartz veins cutting through the rock. The lithology has a very schistose texture and is very porous, due to the talc content in the rock. The rock is

very fine grained with thin compositional layers showing a strong foliation. Microstructures

Fig. 5.4: Talc schist found ca. 50 meters from Gryteberget. Pencil for scale

in the rock show complex folding structures that are especially visible in the lighter layers.

Fig. 5.5: Transition between the ultramafics (bottom) and the surrounding lithologies (top) at Vetle Raudberget with three lithologies. Talc (lower part of outcrop), amphiboles (actinolite?) in the middle and the surrounding metapelite on top. Hammer for scale.

Fig. 5.5 shows the transitional found between Vetle Raudberget and the metapelite. Underneath the metapelite there is a layer of actinolite that has a bright green in colour, followed by a layer of talc.

5.2 Metapelites

The dominating lihologies in the study area are phyllites, mica schists and quartz schists (from here called metapelites). The appearance and mineralogical composition varies a lot within this unit with gradual transitions and local variations, often over small distances, making them difficult to map in detail. For this reason all the lithologies are mapped as one unit.

All of the metapelites are foliated and schistose with layers of biotite/muscovite/chlorite and quartz/K-feldspar/carbonate, and shows intense folding easily visible in the quartz lenses (fig. 5.6). Some locations also have abundant graphite, used for thermobarometric studies (Jakob *et al.*, in prep (b)). The thickness of the bands varies between <1mm-2mm.

The parts of the metapelites that contain carbonates have an eroded surface where carbonates have been washed out. Grain size varies, but is normally between 1-2mm for the non-mica minerals. The colour is dominantly grey, with layers of light non-mica minerals and the darker layers of mica. The lithologies have numerous quarts lenses. Most of these have an asymmetrical shape and can be used as kinematic indicators (see below). The strength of the rocks also varies a lot within the layers, but the general trend is that the carbonate holding parts are weaker and more porous, while the non-carbonate bearing parts are stronger. The grade of deformation varies within the layer, from showing intensely folded quartz veins, to less deformed parts with only minor visible folding.

Fig. 5.6: Carbonate rich foliated mica schist, with folded quartz lenses. Some of the exposed carbonates have been washed out of the rock. The lithology shows a clear foliation with dip towards the SE. Photo taken at Kvilesteinsvatnet. Hammer for scale.

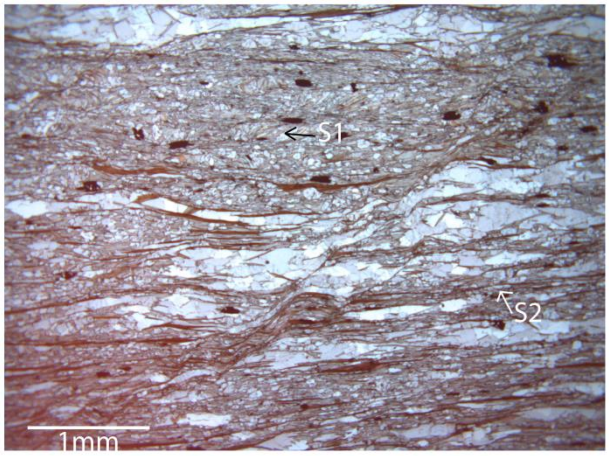

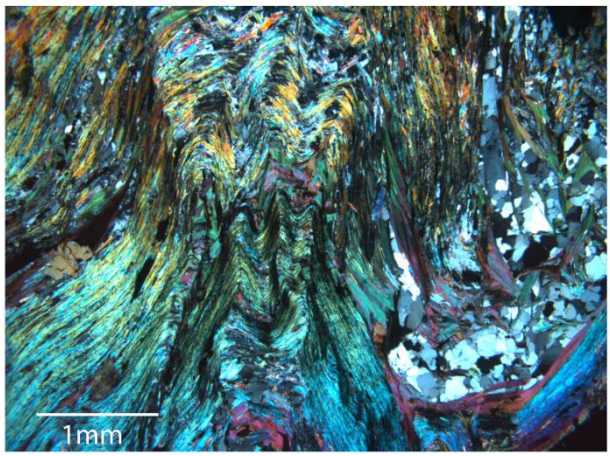

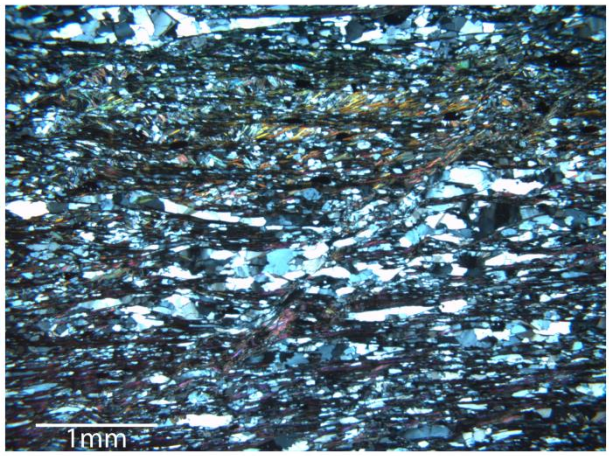

Fig. 5.7: PPL and XPL this-section photos of the metapelite. S1 generation foliation is folded during D2 deformation stage. Sample 54-14

Fig. 5.8: Three generations of deformation in the metapelite. S1 foliation orientated vertically largely overprinted by S2 foliation orientated horizontally. Late shear band cutting diagonally across the thin-section. Sample 17-14

Fig. 5.7 shows an intense folding of the first generation foliation during later deformation, with parasitic folds. The later deformation stage is mostly observable in the fine grained micas, while the larger quartz/K-feldspar crystals is largely unaffected by the folding.

This unit made up of micas (biotite, chlorite and muscovites), quartz, plagioclase and K-feldspar. Biotite and chlorite are often found as elongated and interlayered crystals, up to 0,9x1,7mm in size. In foliated parts of the metapelites, the mica crystals are found orientated along with the foliation. The biotite shows little variation in geochemistry and the chlorites has a high FeO content. Feldspar ($An_{\sim 35}$) and quartz have a large variation in grain size, with the largest grains up to 0,75x0,5mm. Large quartz lenses (>2m) area found on several locations. Samples taken from the calcareous holding parts of the metapelites

Fig. 5.9: Lower part of outcrop: Fine grained and laminated dark grey phyllite with small quartz veins. Upper part of outcrop: Coarser grained and lighter colour mica schist with carbonates. The outcrop is c. 3m tall. Photo taken south of Raudberget.

are rich in calcite. The grains size of the carbonate crystals average 0,75x0,6mm. The calcites vary between 51,5wt% and up to 59,7wt% in CaO.

Fig. 5.8 shows a thin-section photo of the metapelite. Three generations of deformation is observable in the figure, two generations of foliation and one late shear band. The first generation folitation is made up of biotite, while two second is muscovite and chlorite. The two foliations is orientated almost perpendicular on each other. The shear band cuts through the second generation of foliation, showing a late stage deformation.

Amphibole

One of the samples taken in the metapelite unit is amphibole bearing, along with biotite, chlorite, calcite and feldspar. The amphiboles have a small variation in both Si and relative Mg/(Mg+Fe) composition. All of the analysed amphiboles plot in the magnesio-hornblende section of the classification (Fig. 5.10)

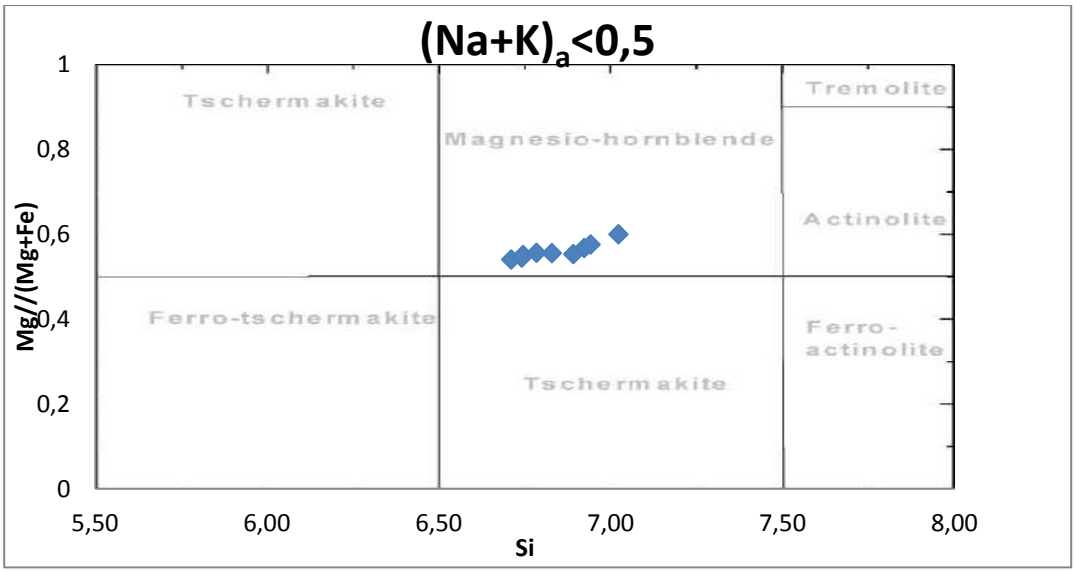

Fig. 5.10: Amphibole classification of the amphibole bearing sample from the metapelite unit. All amphiboles plot as magnesio-hornblendes, with little variation in Si and relative Mg/Fe content. Sample 43-14

5.3 Garnet micashists

Fig. 5.11: Garnet micaschist, with multiple large garnets up to ca. 1cm in diameter. The lithology shows a clear foliation with dip towards the SE. Photo taken NW of Raudberget.Pencil for scale.

The garnet micaschist has a well-developed foliation with micas folding around the garnets. The texture of the garnet micaschists is similar to the other metapelite. The rock has a light grey colour, with darker and lighter layers.

Biotite and chlorite are found as elongated, interlayered crystals, with biotite been the most abundant of the two minerals. The chlorites in this sample shows a fairly large variation in FeO (24,8-38,7wt%) and MgO (1,7-14,8wt%), the other elements only show minor variations. Biotite on the other hand only shows small variations in geochemistry. The grain size of the biotite and chlorite crystals are ca. 0,5x0,2 mm. Muscovite are much smaller than the other two kinds of mica. Muscovite shows a slight variation in SiO, AlO and FeO, but is else fairly similar in mineral

chemistry. Most of the micas are orientated in the same direction, along the foliation. The garnet micaschists also have K-feldspar and quartz with a large variation in grain size.

5.3.1 Garnets

The garnets in the garnet micaschist differ in size, depending upon where the sample is taken. Sample 51-14 and 30-14 have both large (<1cm) garnets. Sample 53-14 has smaller garnets, but they are much more numerous (fig. 5.15). The garnets have a dark or dark red colour. The locations of the samples are shown in appendix 2.

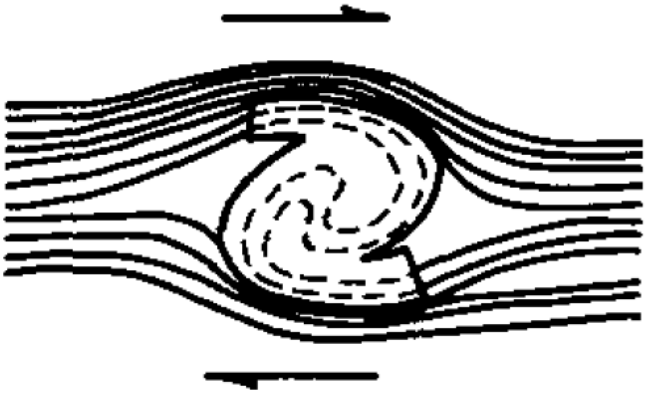

Fig. 5.12: Garnet rotating relative to the matrix during simple shear deformation. From Vernon (1978)

Porphyroblasts (for example garnets) with S- or Z-shape inclusions have for a long time been recognized as products of syntectonic mineral growth (e.g. Zwart, 1962). The development of these inclusive patterns is a result of relative rotation of the porphyroblast and the matrix (fig. 5.12).

The garnets in sample 30-14 and 51-14 both show syn-kinematic growth at prograde metamorphism (fig. 5.13). This garnet shows an anticlockwise rotation during prograde metamorphism.

The larger garnets show distinct S-shaped inclusion trails in thin-sections (fig. 5.13). These inclusion trails are very similar to those found in the Lower Bergsdalen Nappe (Fossen, 1993b). In the Lower Bergsdalen Nappe the majority of these inclusion trails give a top-to-the-E shear direction. The garnets are set in a matrix of micas which show abundant evidence for D2 deformation reworking (Fossen, 1993b and fig. 5.11). Other garnets (fig. 5.14) show no folding of the S1 foliation.

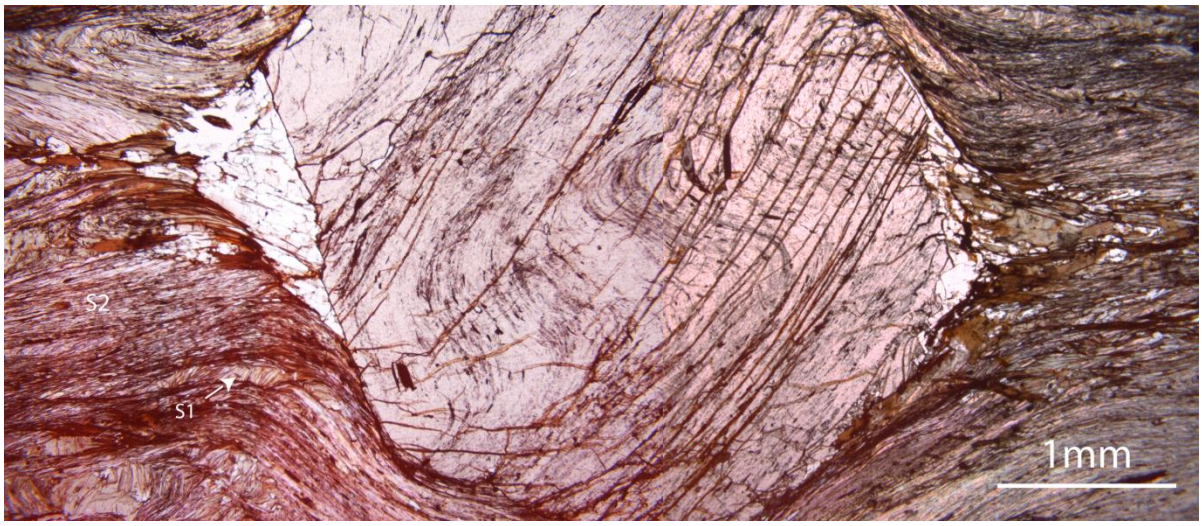

Fig. 5.13: Garnet in the garnet micaschist showing syn-kinematic microfolds of S1 fabric in the garnet, from growth at prograde metamorphism, with anticlockwise rotation. Two generations of foliation is visible in the matrix, S1 and S2. S1 running vertical and the dominating S2 running horizontally. Sample 51-14

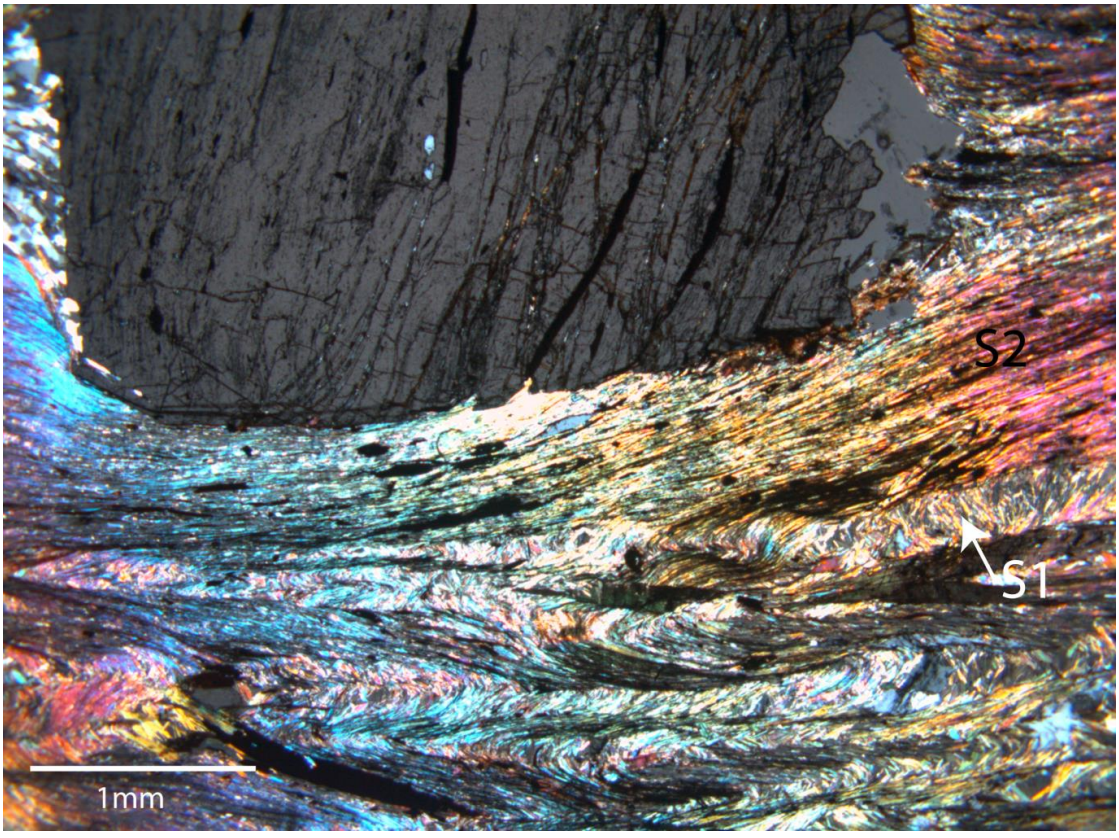

Fig. 5.14: Remnants of S1 foliation orientated vertical on the photo, visible in the garnet and the mica matrix. The dominating S2 foliation is bending around the garnet crystal. Sample 30-14

There are two generations of foliation visible in thin-sections of the garnet micaschist, S1 and S2 (fig. 5.13 and 5.14). The S2 generation is the dominating foliation, largely overprinting the earlier S1 foliation. Mineral inclusions in fractures in the garnet most likely show secondary mineralization during D2 deformation (see below) (Fossen, 1993b).

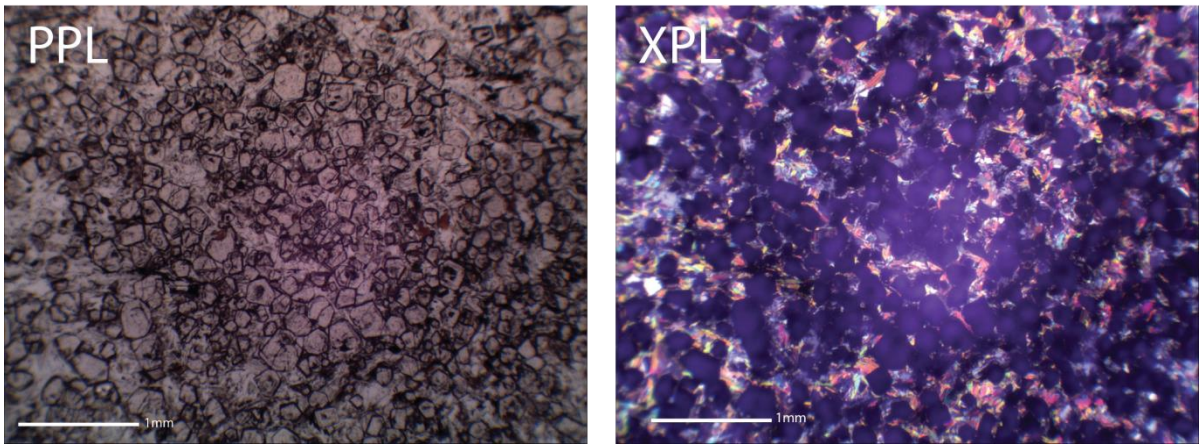

Fig. 5.15: Plane polarized light (PPL) and cross polarized light (XPL) photo of sample 53-14. Numerous small garnets set in a matrix of fine-grained micas.

Chemical zonation of the MnO concentration in garnets set in metamorphic rocks very common. Most frequently the garnets show a decrease in MnO content from the core to the rim of the garnet crystal. Because of this a decrease in MnO towards the rim has been called *normal zoning* and an increase towards the rim is called *reverse zoning* (e.g Banno and Chii, 1978). A third kind a MnO distribution with a high MnO core decreasing towards the rim and a enriched rim is called a mixed-type zoning (Banno and Chii, 1978). Normal MnO zonation in garnets can be explained by changing physical conditions, usually progressive, metamorphism (e.g. Müller and Schneider, 1971; Kretz, 1973). Because garnets do not re-equilibrate like other minerals, the crystals preserve the equilibrium composition of each of the prograde continuous metamorphic reaction (Hollister, 1969).

5.3.1.1 Element map sample 30-14

The garnet chosen for element mapping, shown in fig. 5.17A-E has been partially dissolved during retrograde metamorphism. The garnet is dissolved all the way into the core of the crystal on the left hand side as the garnet is seen on the element map.

CaO shows an increase towards the edge of the garnet, with the largest content change visible in the outer parts. In the centre of the garnets the content of CaO is 10wt%, with an increase to about 15wt% at the rim. FeO shows first a decrease and then an increase in content. In fig. 5.13 FeO starts on a bit over 50wt% before decreasing to 40wt% in the centre of the garnet before increasing to almost 50wt% at the crystals edge. The red and blue sections in the FeO map, is biotite inclusions in the garnet. The increasing FeO component is balanced by decreasing MnO. MnO shows first an increase from ca. 3wt% and up to ca. 15wt% in the crystals centre before decreasing to 3wt% at the rim of the crystal. The lowest content of FeO corresponds to the highest MnO content and most likely shows the old centre of the garnet, before the garnet was dissolved. The red, green and yellow sections in the MgO map are inclusions of other minerals.

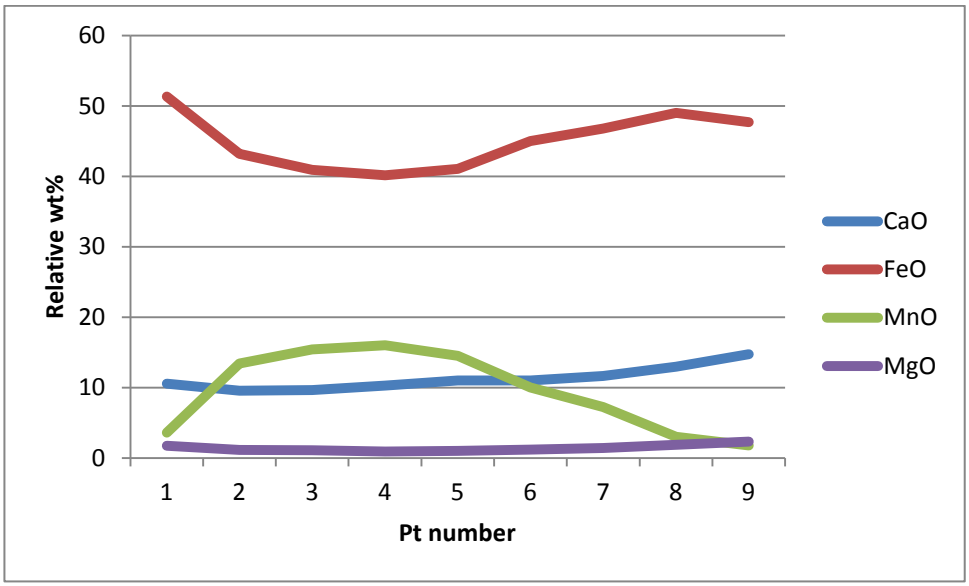

Fig. 5.16: Qualitative element zonation of one of the garnets in sample 30-14, seen in figure 5.17, normalized to 100%. Pt. 4 is the centre of the garnet and pt. 9 is the rim. CaO shows an increase towards the crystals edge. MgO shows a slight increase at the rim of the garnet. MnO has a maximum content in the centre with ca. 16wt% and show a decrease towards the rim. FeO is lowest in the garnet centre and increase towards the rim, before decreasing again at the rim.

The EMP zonation map in fig. 5.17 show the quantitative zonation of the four elements in the garnet. The element map reflects the plot in fig. 5.16, with the largest variation in FeO and MnO, with slight variation in CaO. The element map shows that the garnet zonation is not perfectly symmetrical.

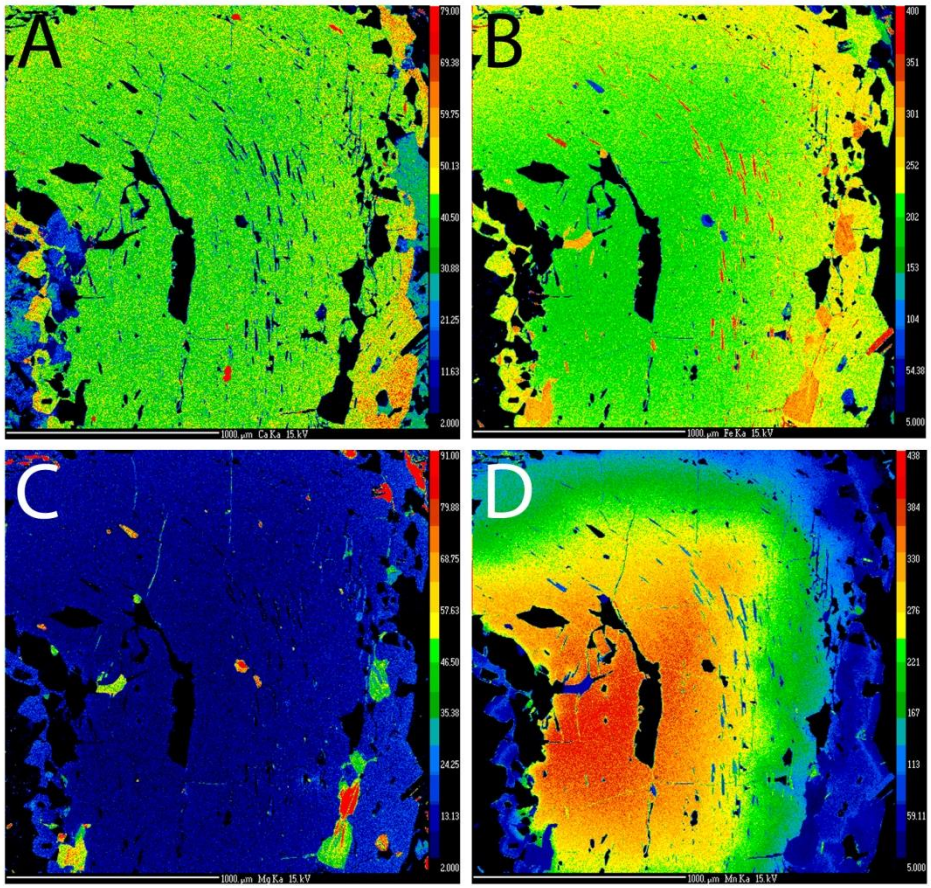

Fig. 5.17: Quantitative element zonation of a garnet in sample 30-14, from the EMP. A: CaO B: FeO C: MgO D: MnO. Visible increase in CaO at the rim of the garnet. FeO how an increase towards the rim of the crystal, and a slight decrease at the rim of the garnet, also visible in fig. 5.16. MgO shows only a slight increase at the garnets rim. MnO shows a clear zonation, with the highest concentration in the centre of the garnet. MnO zonation shows that the garnet is not perfectly symmetrical.

5.3.1.2 Element map sample 51-14

Fig. 5.18 shows an element profile of a garnet in sample 51-14, because of the size of the crystal only half of the garnet could be mapped in the EMP. Some of the garnets have a fissure system going through the crystal, visible in fig. 5.19A. Oxide inclusions and cracks in the garnets show a folding structure in the garnet crystals. Fig. 5.18 and 5.19 shows an increase in FeO towards the edge of the garnet. MnO shows a general decrease towards the edge. An internal rim of higher MnO content is visible indicating at least two growth phases. In increase of MnO must mean a decrease in other element, but the same clear rim is not easily visible in none of the other elements. The edge of the garnet also shows an increased MnO content. MgO shows an increase towards the garnets edge. CaO and AlO show no zonation, but on the edge of the garnet show an increase in CaO.

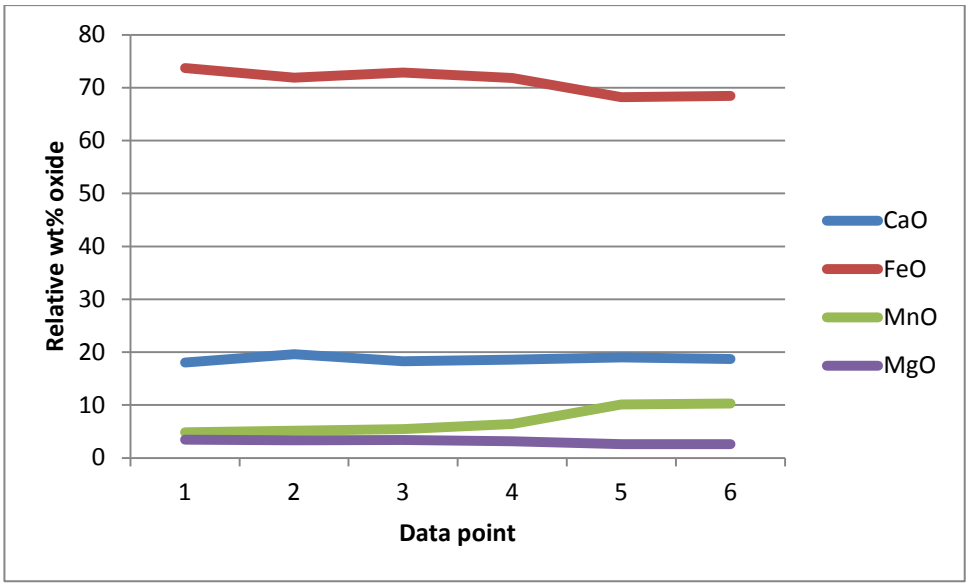

Fig. 5.18: Qualitative element zonation of a garnet in sample 51-14, with pt. 1 being the edge of the crystal and pt. 6 the centre. CaO and MgO show no zonation. FeO shows a slight decrease towards the centre of the crystal. MnO shows a slight increase in the centre of the garnet.

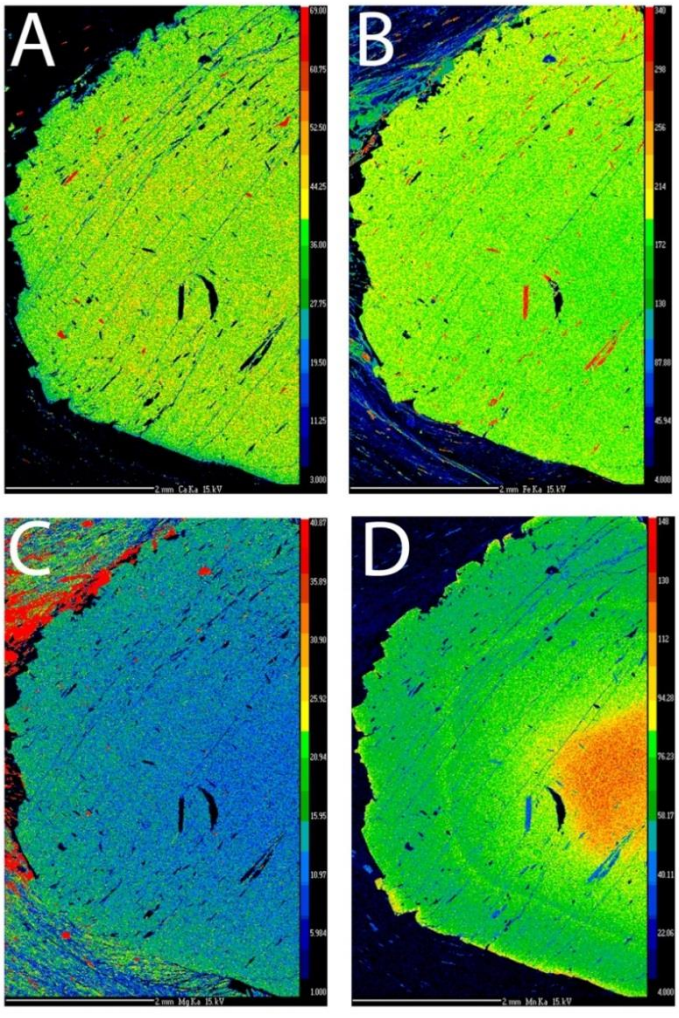

Fig. 5.19: Element map of a selected garnet in sample 51-14. A: CaO B: FeO C: MgO D: MnO. No visible zonation in Ca, but a slight decrease at the rim. Fe shows a small increase towards the edge of the garnet. MgO shows a slight increase towards the edge. MnO shows a clear zonation of with the highest concentration in the centre, with a MnO enriched rim. An internal MnO enriched rim is also visible, without a clear decrease in the other elements. The internal MnO rim could be a result of a second stage garnet growth.

The garnet seen in fig. 5.19 show a retrograde dissolution at the edge of the crystal. During retrograde metamorphism the edges of the garnet have been dissolved. The MnO of the original garnet have than been reabsorbed into the garnet,

leaving a MnO enriched outer rim.

5.3.1.3 Element map sample 53-14

The garnets in this sample show a nice element zonation especially for FeO and MnO, shown in fig. 5.20 and 5.21. The other mapped elements show no visible zonation in the element map. Fig. 5.20 show the relative distribution of the mapped elements, normalized to 100% in the mapped garnet.

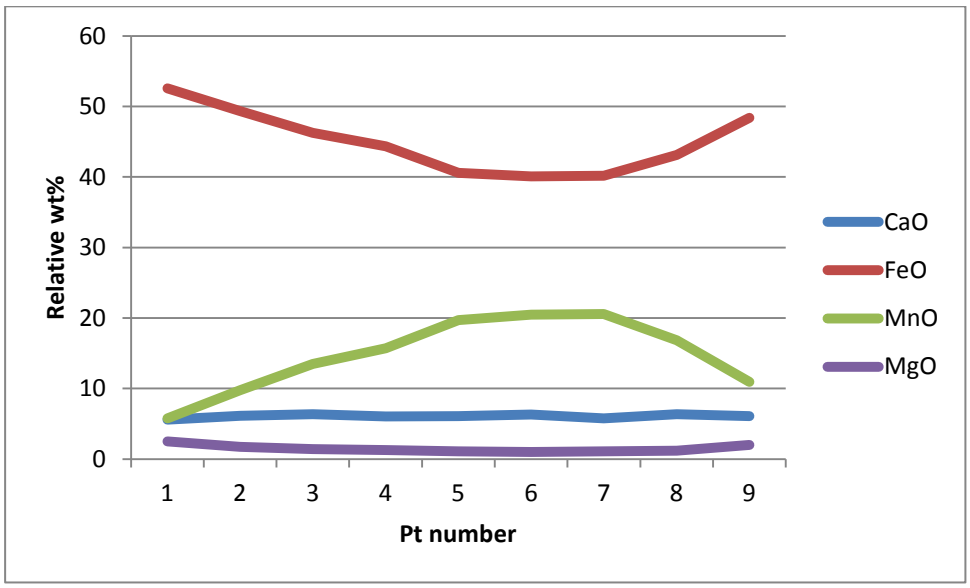

Fig. 5.20: Qualitative zonation of a selected garnet in sample 53-14. Pt. 5 shows the centre of the garnet. CaO and MgO show no zonation. FeO shows a decrease towards the centre of the garnet, from ca. 53wt% to ca. 40wt%. MnO shows a decrease from ca. 21wt% in the centre and ca. 6wt% at the rim of the crystal. The plot shows that the zonation in the garnet is not perfectly symmetrical.

The CaO content is evenly distributed throughout the garnet with only a small variation. FeO show an increase towards the edge of the crystal, and vary between 40wt% in the crystal centre to 52wt% at the edge. MnO shows a clear zonation with the highest concentration in the centre of the crystal and decreasing towards the edge. In the core of the garnet crystal manganese has a bit over 20wt%, while at the edge of the crystal the content is down to under 6wt%. MgO shows a small increase along the crystal's edge and no zonation in the core of the crystal. Fig. 5.21 shows that the garnet is not perfectly symmetrical in element distribution. This can be seen in element map for MnO, where the green coloured field on the right hand side of the garnet is somewhat larger then on the left hand side.

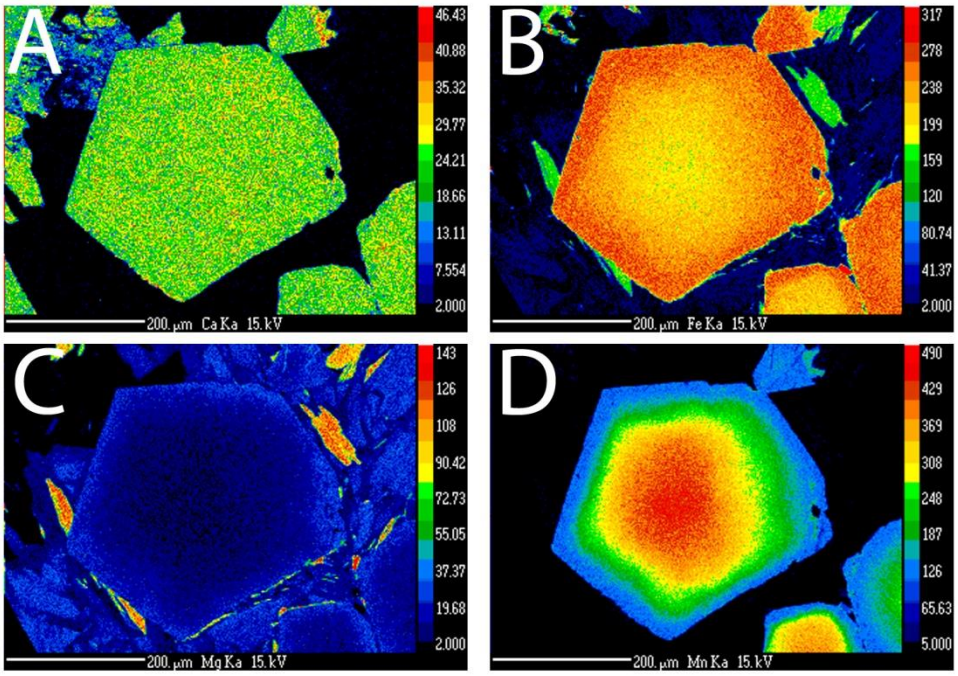

Fig. 5.21: Quantitative element map for a selected garnet in sample 53-14 from the EMP. A: CaO B: FeO C: MgO D: MnO. CaO and MgO show no zonation, but MgO shows a slight increase at the edge og the crystal. FeO shows a clear zonation with the highest concentration at the edge of the crystal. MnO shows a distinct bell-shaped zonation with the highest concentration in the centre of the crystal.

5.4 Gneiss

Two outcrops of the Upper Bergsdalen Nappe are visible in the study area (see appendix 1 and fig. 6.5). The Bergsdalen nappes consists of kilometre thick slices of Precambrian metasedimantary rocks along with volcanic and igneous rocks (Kvale, 1946), and was significantly affected in the Caledonian orogeny (Fossen, 1993a; b). The gneissic rocks in the study area have been dated to 1496±7Ma (Jakob *et al.*, in prep (b)). Samples taken of the gneissic rocks at Bjørnshaugen and in the area shown in cross-section C-C', have an almost identical mineral assemblage and texture, suggesting that they area of the same stratigrafical layer.

The colour of the lithology varies throughout the layer, but the rock is mainly light grey in colour with layers of dark mica. The lithology has a large variation in macroscopic texture. Some parts of the rock show a clear foliation with layers of quartz and darker minerals e.g. biotite. Other parts show little to none foliation or microstructures. The rock is massive and shows small parasite folding visible in the darker layers in the foliated parts.

Fig. 5.22: Contact between the gneissic rocks (left side) and the metapelite (right side) at cross-section C-C'. The gneissic unit structurally overlies the metapelite as shown in fig. 6.6. Photo taken on the eastern side of the synform, towards the NE.

The unit is very quartz rich with a variation in crystal sizes, with the larger crystals reaching 0,5x0,25mm. Biotite are found as vary small elongated crystals up to 0,4x0,05mm in size. The fairly few biotite crystals are evenly spread out in the thin section. A few muscovite grains were found in the thin-sections, and were slightly bigger than the biotite crystals. The lithology also has some plagioclase, with a maximum size of c. 0,5x0.25mm.

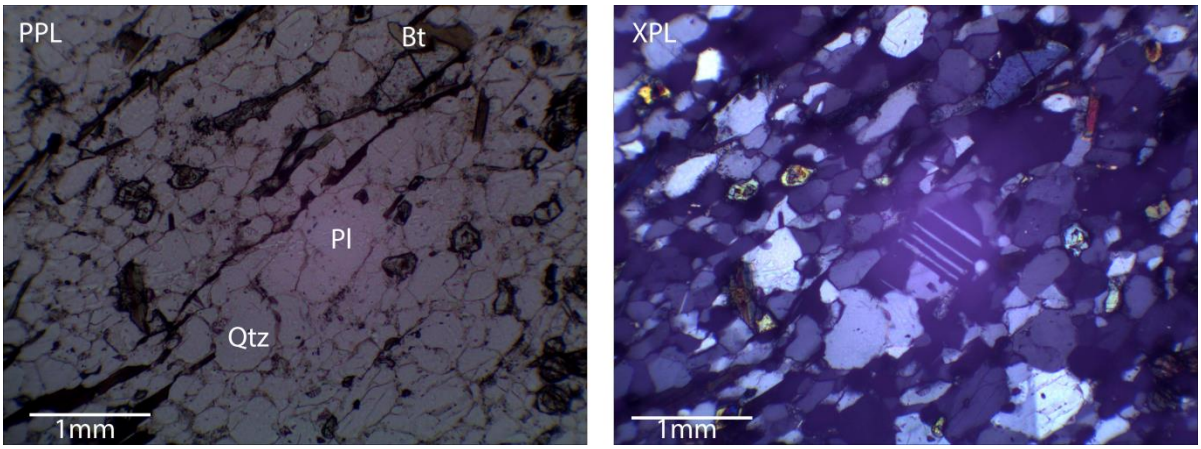

Fig. 5.23: PPL and XPL thin-section images of the gneissic unit. The dominant mineral is quartz with one plagioclase crystal and some small micas. Sample 27-11.

5.5 Garnet amphibolites

Fig. 5.24: Garnet amphibolite located south of Raudberget, with light red garnets in a dark to black, fine grained massive matrix of amphiboles, plagioclase, chlorite and quartz.

The garnet amphibolite has a maximum thickness of approximately thickest ca. 50 meters wide and consists mostly of a massive, garnet rich rock. No primary structures has been observed and it is not known if it is intrusive, part of the sequence as a lava or an older sliver of basement like some other amphibolitic units in the mélange (Jakob *et al.*, in prep (a)).

The rock is for the most part massive with a dark colour with red garnets. The garnets are set in a fine grained matrix of quartz, amphiboles, plagioclase and chlorite. The observed maximum size of the garnets found in the garnet amphibolite is 1,3x1,3mm. All studied garnets have multiple fractures orientated in the same direction cutting through the crystal with inclusions of the same minerals as the matrix and some of the garnets are partly dissolved. The garnet amphibolite has a high content of plagioclase. All the analyses show a

high content of NaO relative to CaO, with an average of 87% albite and 13% anorthite. This puts the plagioclases in oligoclas section of the solid solution series. The lithology also contains quartz and a minor content of fine grained chlorite showing a high FeO (28,6wt%) and low MgO (12,9wt%) composition.

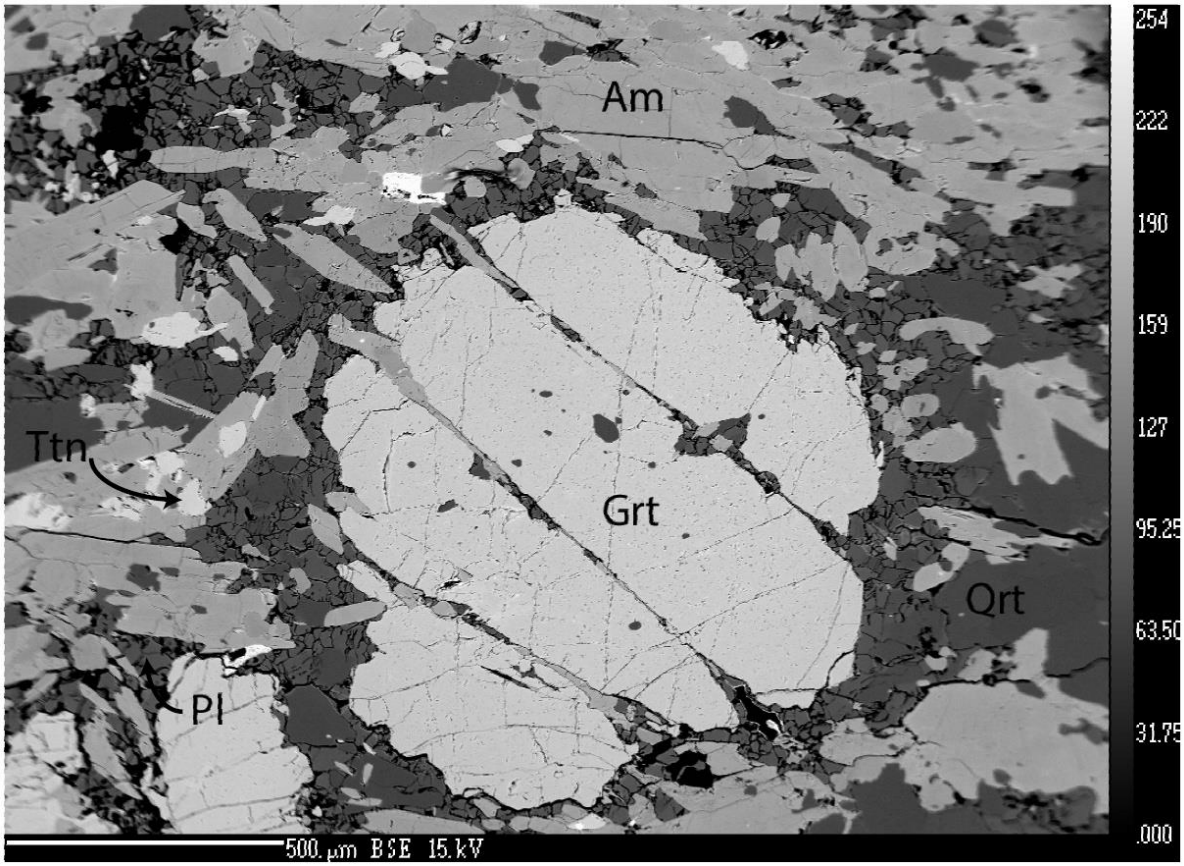

Fig. 5.25: BSE image of the garnet amphibolite. The unit is rich in amphibolite, quartz and plagioclase, with some titanite. The fractures from (possible) D2 stage deformation stage in the garnet are filled with quarts, plagioclase and amphiboles. Sample 65-14

Microscopic and EMP analyses show that the rock is rich in amphiboles. Since the amphibole compositions are near the intersection of three different varieties, they get different names even given a fairly similar geochemistry. The amphiboles vary from ferro-tschermakite, tschermakite to magnesio-hornblende.

The amphibole crystals have a large variation in shape and sizes, and vary few of the crystals show the typical $60^{o}/120^{o}$ cleavage typical for amphiboles. Instead the crystals commonly have a rough uneven edge and are anhedral in shape. In thin sections the amphibolites have a bright green colour.

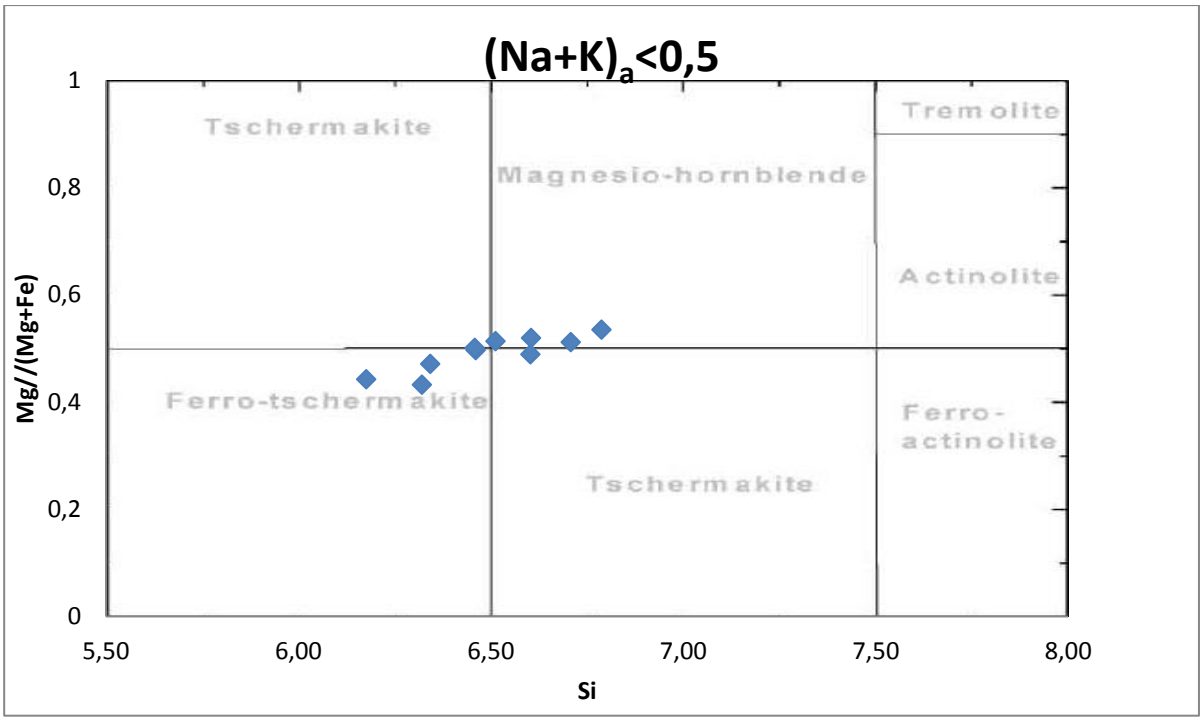

Fig. 5.26: Amphiboles in the garnet amphibolite. The amphiboles plot in the intersection of ferro-tschermakite, tschermakite and magnesio-hornblende. They show a small variation in Mg/(Mg+Fe) composition and have between 6,2-6,8 Si per formula unit. Sample 65-14

There is also one amphibolite other amphibolite body in the study area. This amphibolite has less garnet than the garnet amphibolite, even though they are present in the lithology. The amphibolite is light to dark grey in colour. The rock is massive and shows a clear foliation. The amphibole and epidot/clinozoisite crystals have an elongated shape that is orientated in a preferred direction making up the foliation in the rock (Aarflot, 1984).

The amphibolite was not studied on a microscopic level, but Aarflot (1984) looked more closely at the mineralogy and a summary of the mineralogy in the amphibolite is given in table 5.1.

Table 5.1: A short summary of the mineralogy in the amphibolite, with the approximate distribution of the different minerals. Based on Aarflot (1984):

Mineral	Short description	Distribution
Amphibole	0,1-4mm in size. Found as elongated and prismatic crystals.	55-60%
Epidote/Clinozoisite	<0,5mm in size. Found as both rounded and elongated crystals	ca. 20%
Feldspar	Grains size varying between 0,1 and 0,8mm	ca. 14%
Quarts	Similar to feldspar in both grain size and appearance	2-4%
Titanite	Found as small (0,1mm) rhombic crystals. Uneven distribution	2-4%
Garnet	Similar to the garnet amphibolite in appearance and texture, but less common.	<1-3%

5.6 Blackwall altered schists

These two units area only found in contact with the ultramafic bodies of Raudberget and Vetle Raudberget, suggesting that they are a form by blackwall alteration. This is a metasomatic process around ultramafics that leads to enrichment of Mg creating amphibole rich contact with the surrounding country rocks (Beinlich *et al.*, 2010). Two samples of blackwall altered schists has been analysed, one taken at Raudberget and one at Vetle Raudberget.

Ultramafic assemblage	Talc Carbonate	Talc	Ca-Amphibole Chlorite	Chlorite	Transitional CR	CR

Fig. 5.27: Common features of metasomatic reactions between ultramafic bodies and the country rocks (CR) in greenschist to amphibolite facies. From Sanford (1982).

Fig. 5.27 shows common features found in the contact zone between an ultramafic body and the surrounding country rock. Closest to the ultramafics there is first a layer of talc and carbonates then almost pure talc. This is followed by a Ca-amphibole and chlorite zone and a chlorite zone, before a transition into the surrounding lithology.

5.6.1 Actinolite-biotite schist at Vetle Raudberget

The rock has a green colour, with lighter and darker layers, showing a clear foliation with thickness up to 2mm. The rock has a low strength, and breaks up along the mica layers. Some larger quartz lenses are found. The rock show no micro textures. Interlayered with the blackwall altered schist, there is a matrix supported conglomerate with pebbles of dominantly quartz and quartzite, but also leucogranite in sizes up to 15cm (Andersen *et al.*, 2012). One of these pebbles was dated by Andersen *et al.* (2012), giving an zircon crystallization age of 1033±21 Ma , and a time of metamorphism of 410,4±3,1 Ma based on U/Pb dating of titanite.

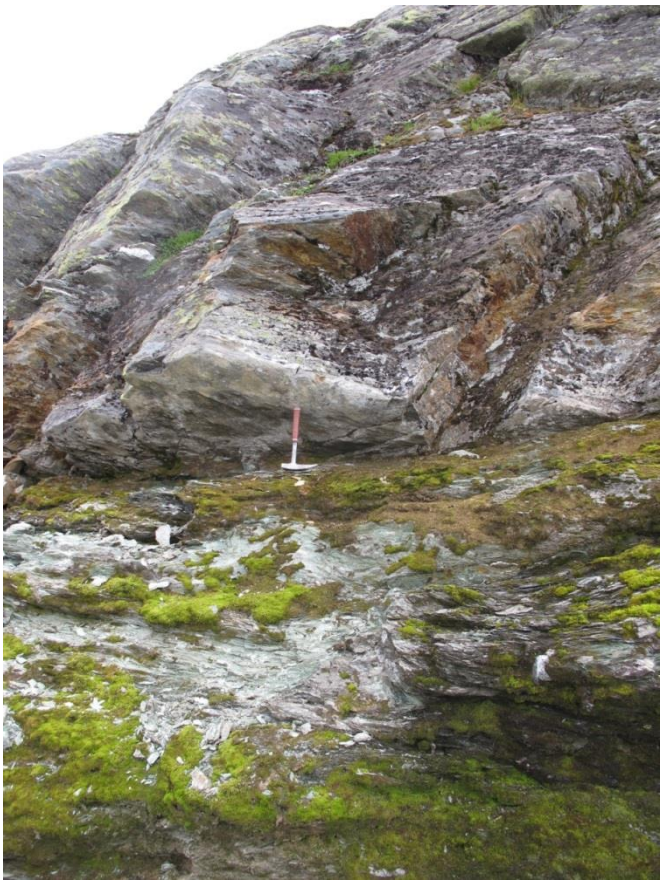

Figure 5.28: Black-wall altered schists (base of outcrop) found in the contact between Vetle Raudberget and the surrounding lithologies down at Kvilesteinsvatnet. Hammer for scale

The altered schist is made up of talc, biotite, epidote, chlorite and carbonate. Biotite is found as elongated crystals orientated with the general foliation in the rock. The crystals have a light brown colour in thin sections because of low Fe content. The biotite crystals show only a minor variation in geochemistry. Both chlorite and biotite show a high MgO content, ~25wt% for chlorite and ~18wt% for biotite.

The amphibole crystals are found as crystals with a very weak green colour in thin-section. A few of the crystals show the typical amphibole cleavage of $60^{o}/120^{o}$, but the crystals are mainly found with uneven edges without cleavage. The amphiboles have a high Si and a high relative Mg/Fe content with little variation, plotting the amphiboles in the actinolite segment of the classification (Fig. 5.30). The content of Si, Mg and Fe has a low variation

giving a close packing of the points in the diagram. A slight trend in increasing Mg relative to Fe following an increase in Si is visible.

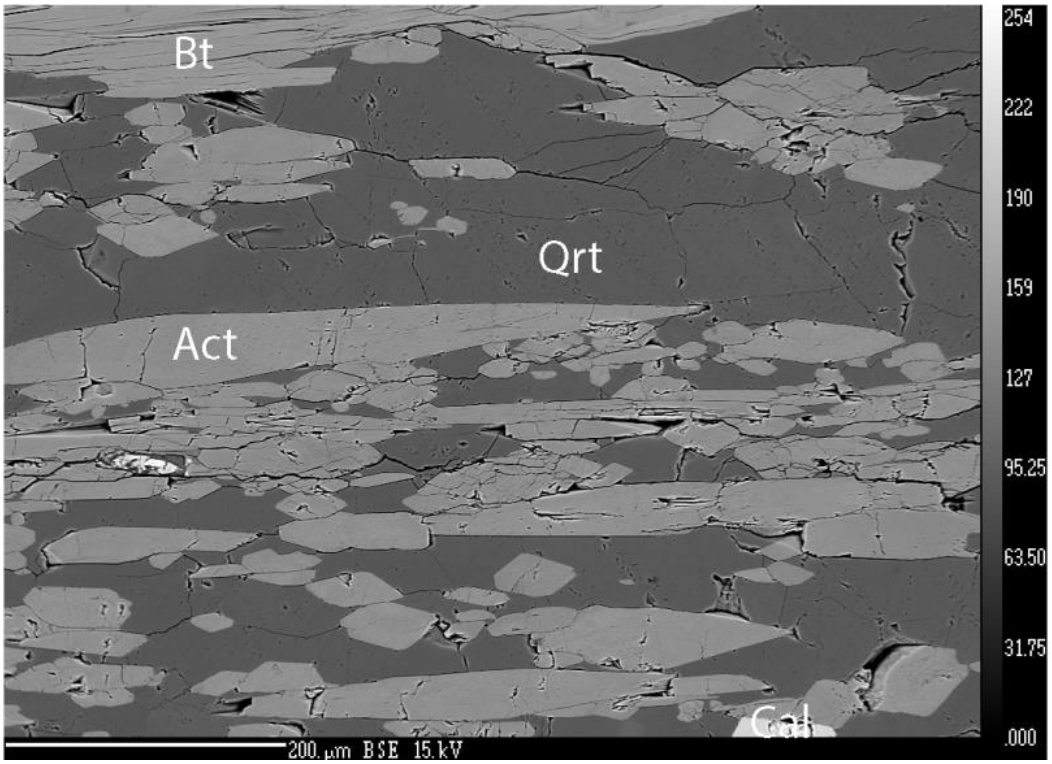

Figure 5.29: EMP image of the blackwall altered schist at Vetle Raudberget. The lithology is rich in quartz, amphiboles (actinolite) and biotite. Sample 60-14.

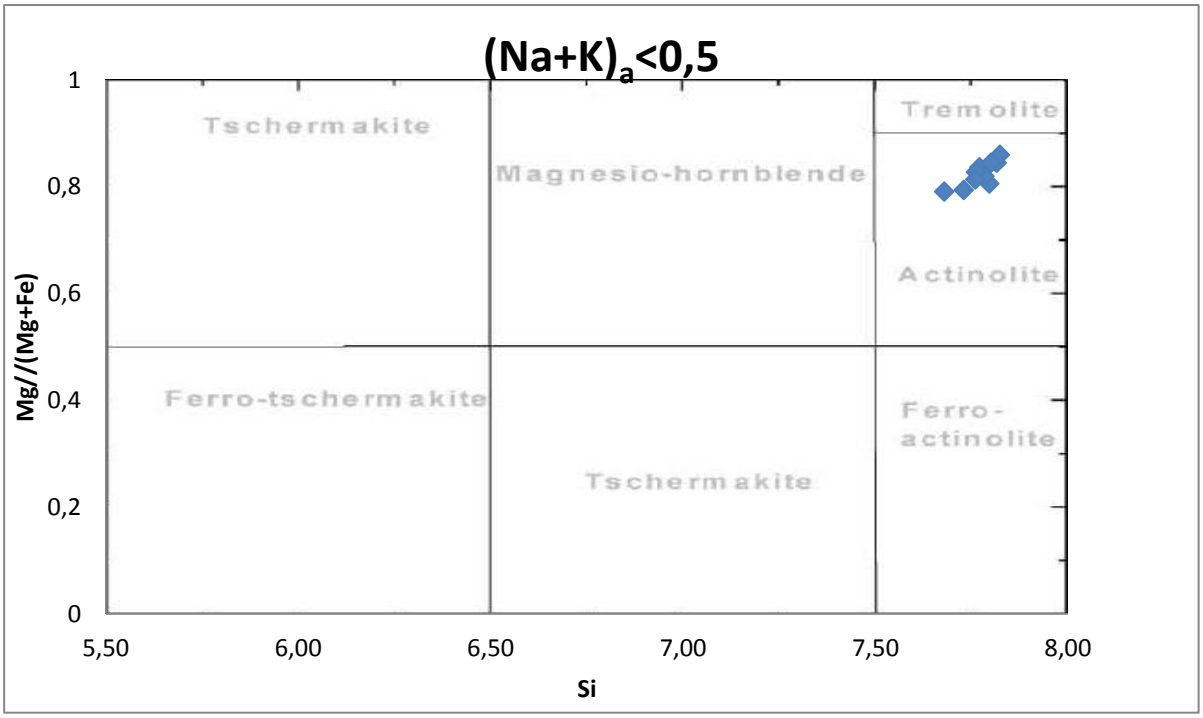

Figure 5.30: Amphiboles in the black-wall altered schist. The crystals all plot as actinolite with a small variation in both relative Mg/(Mg+Fe) and in Si. Sample 60-14

5.6.2 Hornblende-micaschist at Raudberget

The colour on the lihology is weak greenish tint with white and dark layers, giving the rock a clear foliation and weak schistostity. The rock has a higher strength then the blackwall altered schist found at Vetle Raudberget. The lighter layers consisting of quartz show good microstructures, without a clear shear direction. Grain size is fine very grained, with some somewhat larger quartz grains. The lithology consists of chlorite, plagioclase, quartz, carbonate and biotite. Chlorite and biotite both show a high MgO content, ~21wt% for chlorite and ~15wt% for biotite.

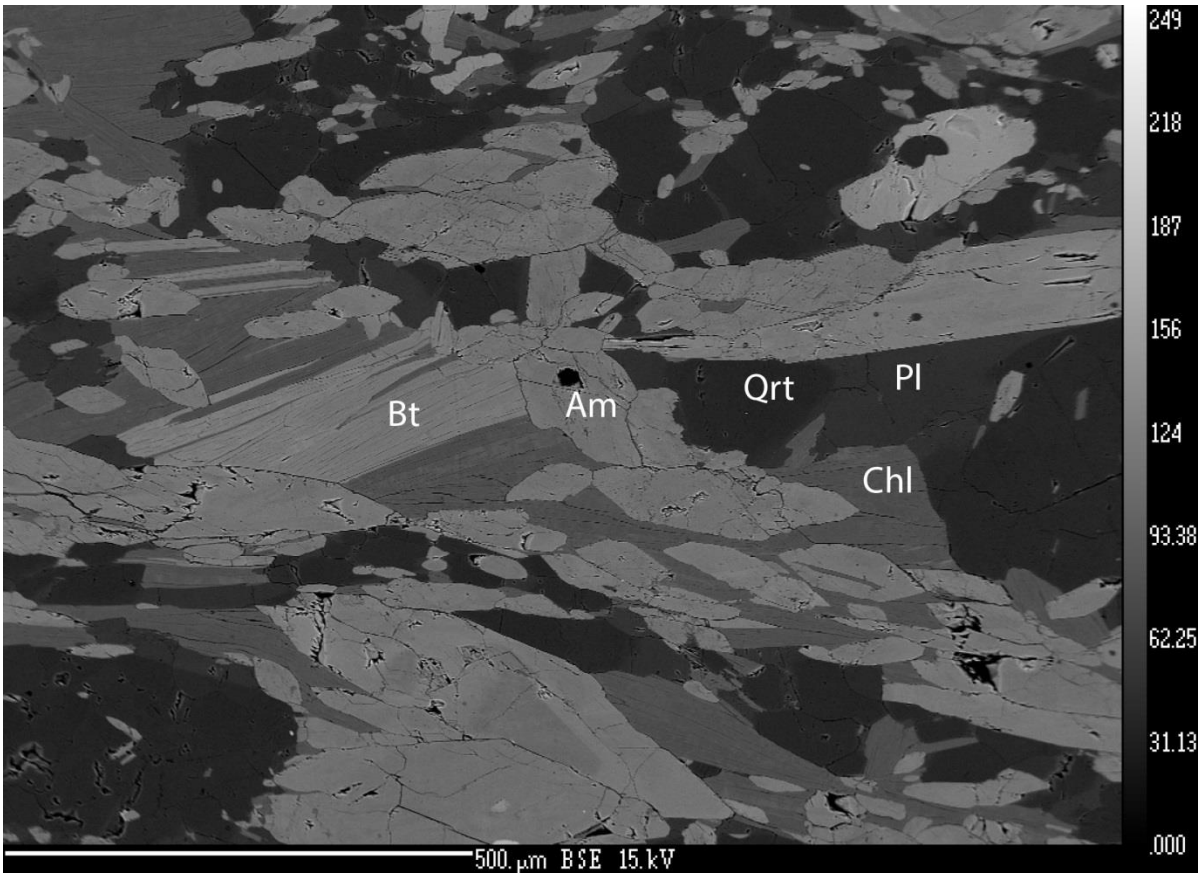

Fig. 5.31: BSE image of the hornblende-micaschist at Raudberget. The lithology has abundant quartz and plagioclase in addition to amphiboles. Biotite and chlorite are found as interlayered crystals as seen in the figure. Sample 68-14

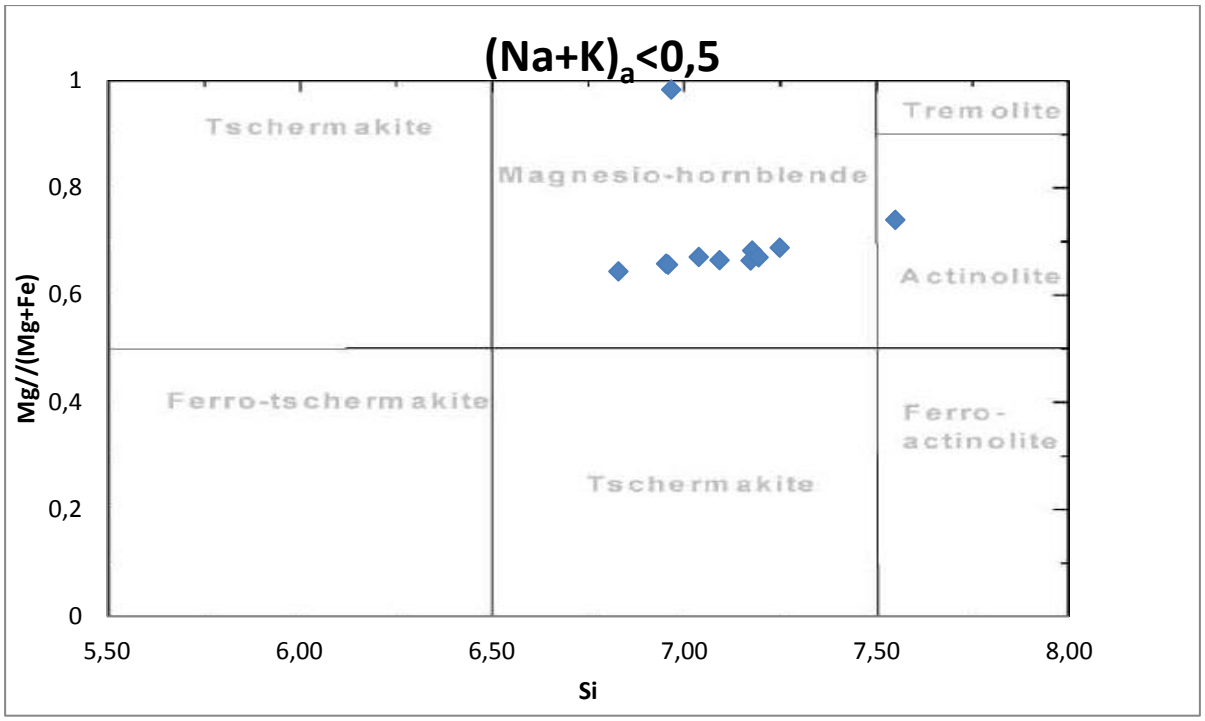

Fig. 5.32: Classification of amphiboles in the hornblende micaschist. Most plot as magnesio-hornblende with one actinolite. One of the datapoints from the EMP show a very high Mg/(Mg+Fe) ratio. Sample 68-14

The amphiboles have a Si content varying around 7,00 atoms per formula unit and a content of Mg relatively to Fe is stable at around 0,65, with the exception of two analyses. The first of the anomalies has a relative Mg/(Mg+Fe) content of close to 1,0, giving a magnesium content almost twice that of Fe. Except the one actinolite, all the amphiboles are magnesio-hornblendes.

6. Structural geology in the Raudberget area

In both the Bergsdalen nappes and in the mélange unit, show two generations of major Paleozoic deformation, as seen by the shear indicators in the lithologies and directly observable fold axis (Fossen, 1993a; b). The older of these two (D1) shows a top to the E or SE shear deformation, related to the main Caledonian nappe translation. The second younger generation (D2) shows a reversal of D1, and indicates a top to the WNW shear direction (Fossen, 1993a).

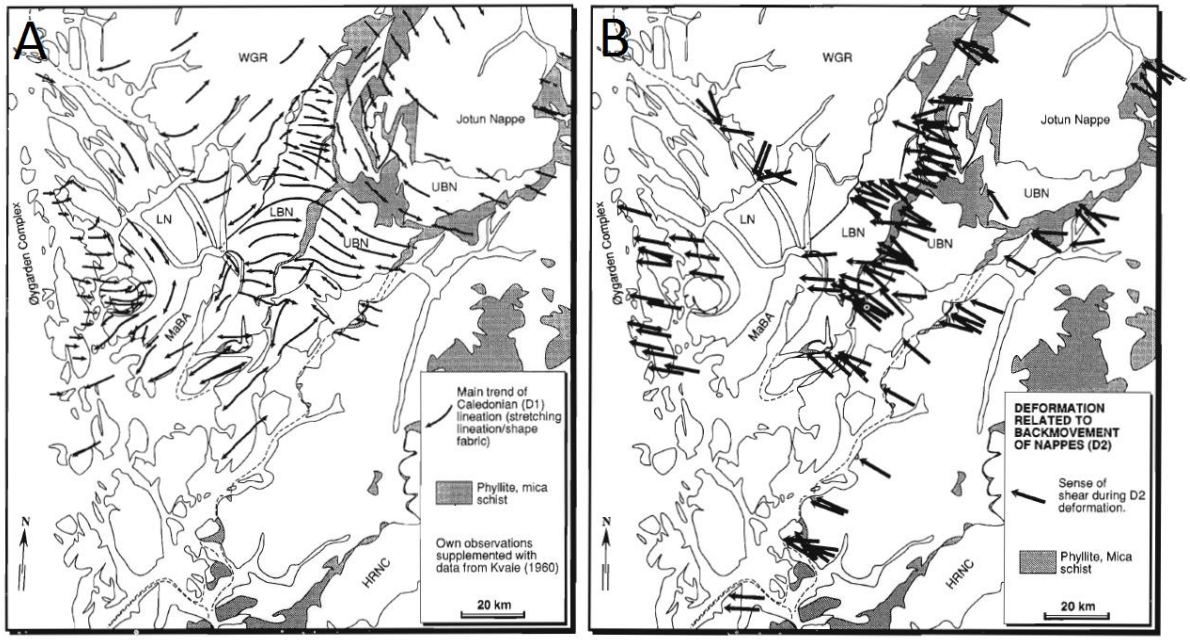

Fig. 6.1: Maps of shear direction given by lineations related to thrusting deformation (D1) (Fig. A) and extensional deformation (D2) (Fig. B) in SW parts of Norway. From Fossen (1993b).

In the Raudberget area there are two sets of fold axis, one running parallel with the main dip direction in the metasediments (NNW-SSE) and the other in a NE-SW direction. The first main fold axis corresponds to the Caledonian cross folds with an D1 age (Fossen, 1993a). These are not easily visible in the non-competent metasediments, but are distinct in the more competent layers (Bakke, 1986). The other main fold axis has a trend corresponding to the last deformation stage in the Caledonian orogeny (D2). The D2 deformation stage is

related to the extensional tectonic exhumation during the extensional collapse of the Scandinavian Caledonides (Andersen, 1998).

During the extensional collapse (D2), the first generation of shear deformation was modified or completely reworked. Mica bearing lithologies in the Bergsdalen nappes often show shear bands of S-C structures with a top to the NW shear sense, which are believed to represent the second generation deformation. On regional scale folds, crenulations and related intersection lineations all show a relative consistent NE shear direction (Fossen, 1993b). The consistent asymmetrical of the D2 kinematic indicators and strain considerations, show that the D2 generation of deformation largely was strongly non-coaxial and close to pure simple shear (Fossen, 1992).

With the exception of the antiform in the amphibolite, the fold axis is not traceable over larger distances. This is particularly the case for the transverse fold axis (fig. 6.2), which is only exposed in a few outcrops in the study area.

Fig. 6.2: Part of an antiform from the Caledonian cross folds found north of Raudberget. The antiform shows folded foliation of gneissic rocks, possibly from the Upper Bergsdalen Nappe. The photo is taken towards the NE, with the plunge of the antiform towards the south. Backpack for scale.

The figure shows a part of an antiform in an outcrop of gneiss NE of Raudberget with NW-SE trend direction. This corresponds to the transverse fold phase.

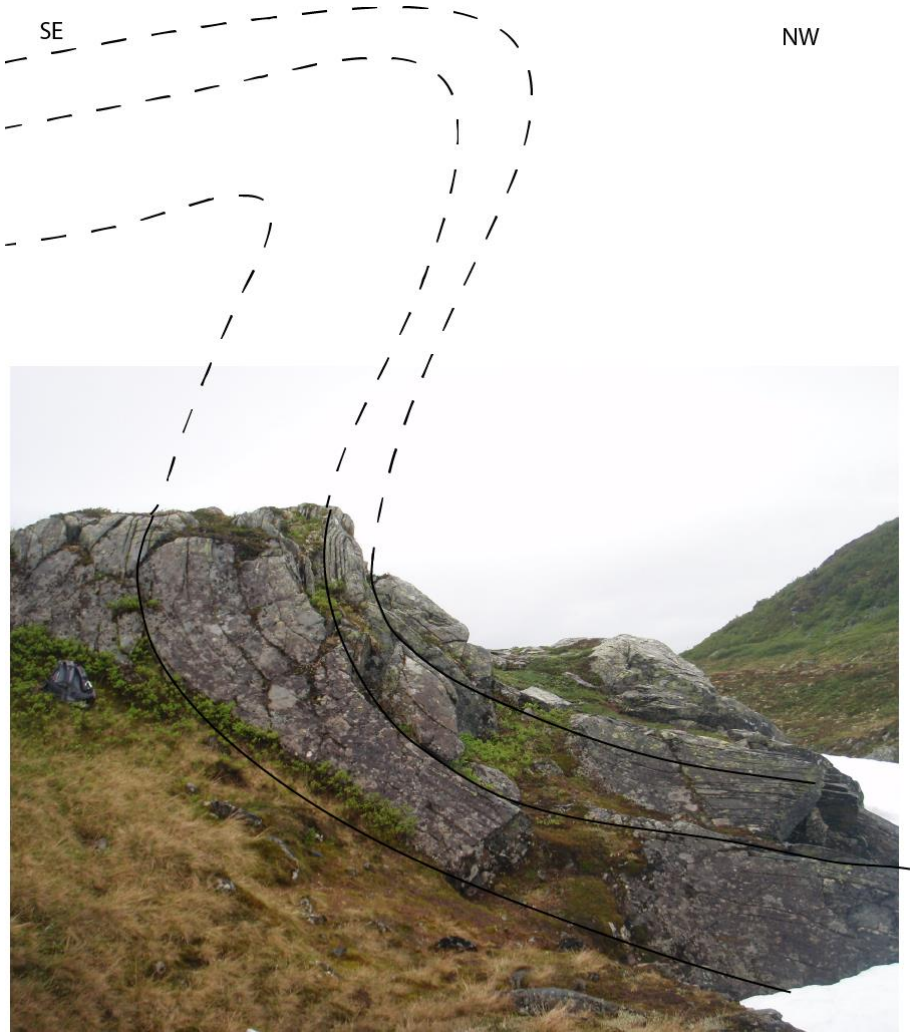

Fig. 6.3: Part of an antiform folding the early foliation in the amphibolite found south of Raudberget. It has a top the NW asymmetry and vergence direction. This suggests a shear direction towards the NW. Backpack for scale

Fig. 6.3 shows a part of an antiform in the amphibolite found south of Raudberget that correspond to the last deformation stage of the orogeny, with a NE-SW trending axis. The antiform in the figure is overturned towards the NW and is similar to the most outspread effect of the D2 deformation stage in the Bergsdalen nappes (Fossen, 1993b). These D2 related folds are found in all sizes from millimetre scale in the micaceous lithologies, through meter scale folds and up to kilometre scale (Fossen, 1993b).

6.1 Stereographic projections

The stereographic projections below are divided unto subareas, one for each side of Raudberget, see appendix 2. The first subarea shows the foliation in the metasediments SE of Raudberget. The foliation shows a small variation in both strike and dip, and has an average orientation of 032/35. Subarea 2 shows the foliation north of Raudberget. This area has a slighter bigger variation on strike and dip, but with the same average of 032/35. Both fall into the dominant trend of the area, with an N-NE – S-SW strike direction with a dip of 20-40^{o} towards the E-SE (Bakke, 1986).

Subarea 3 shows the foliation in the area SW of Raudberget, and show a more complex trend in the foliation. The overall average in strike and dip is 252/30. There are two main trends is strike direction, towards the ENE and NNW. The average strike and dip of the two dominating trends are 256/27 and 276/36, respectively.

6.2 Cross-sections

Two cross-sections have been constructed covering the study area. In addition a third regional cross-section with a corresponding map showing the Stølsheimen area, have been made based on the NGU map database. All cross-sections are made perpendicular to the main fold axis in the area. No primary sedimentary structures have been found, except local bedding in the conglomerate found near Vetle Raudberget. The interoperation of the overall folding structure is therefore based on strike/dip measurements.

The main cross-section A-A' (fig. 6.4) have been constructed from the transition from the underlying LBN to the UBN, covering the entire study area. The cross-section is an interoperation of based on field observations and drill core data from Bakke (1986) and Aarflot (1984). From the drill cores and cross-sections made (Bakke, 1986) from Bjørnshaugen the approximately location and scale of the ultramafic bodies is known.

Cross-section B-B' (fig. 6.5) shows one of the overturned synclines, NW of Raudberget. The cross-section are based on strike and dip measurements and observations of the gneissic rocks. The garnet micaschist located on the NW flank of the syncline (see appendix 1), is not found on the NE side.

Cross-section C-C’ (fig. 6.6) is based on cross-section A-A’ and date collected from the NGU map database. The cross-section and geological map covers the area from the WGR in the NW to the JNC in the SE, giving the structural positioning of the mélange unit relative to the major Allochthon nappes. The study area is marked in red. Following the old classification the LBN is included in the Lower Allochthon, while the UBN and the JNC are parts of the Middle Allochthon.

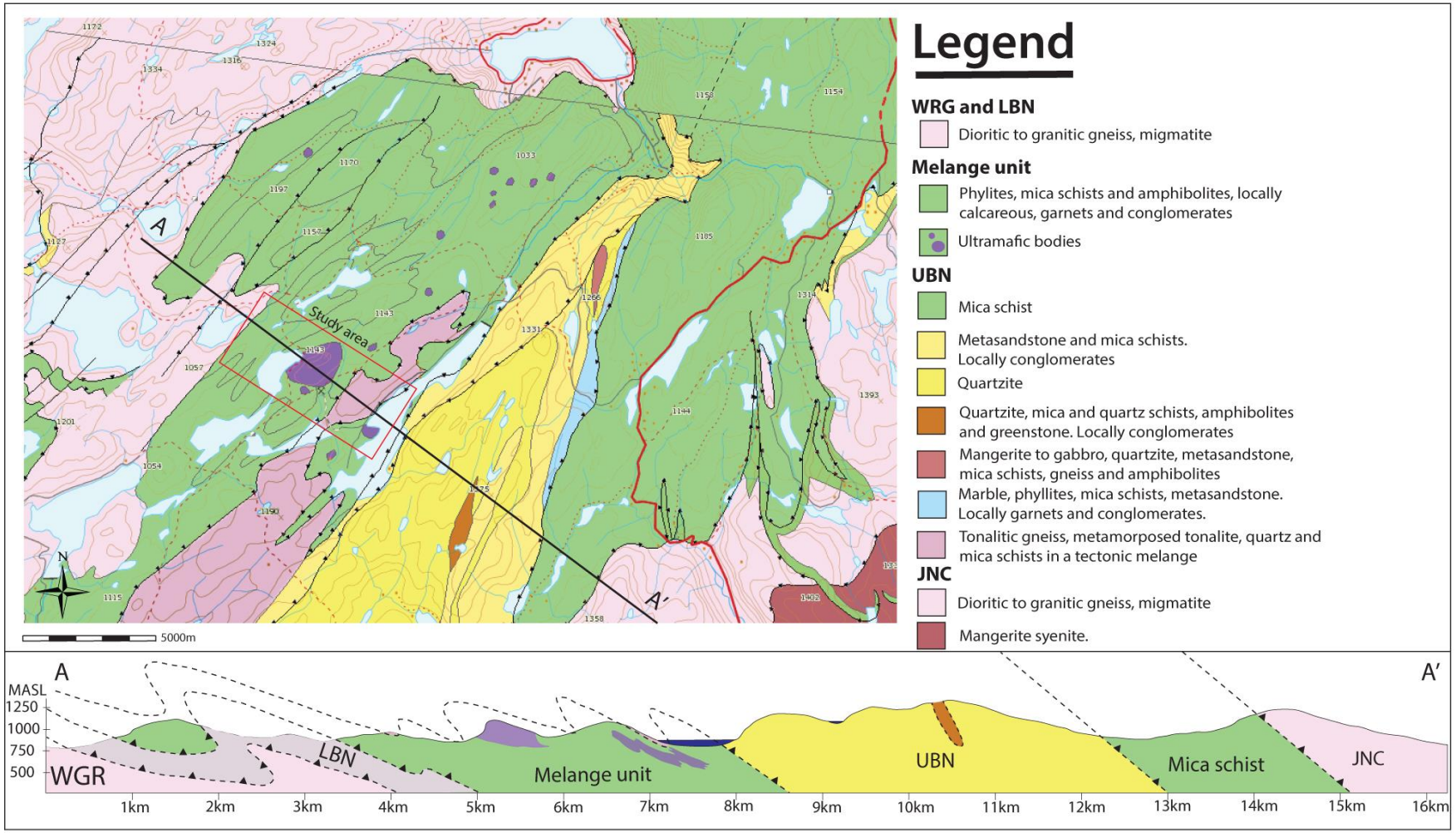

Fig. 6.4: Geological map over Stølsheimen and adjacent areas, with a cross-section from the Western Gneiss Region (WGR) in the NW to the Jotun Nappe Complex (JNC) in the SE. Map modified from geo.ngu.no/kart/berggrunn.

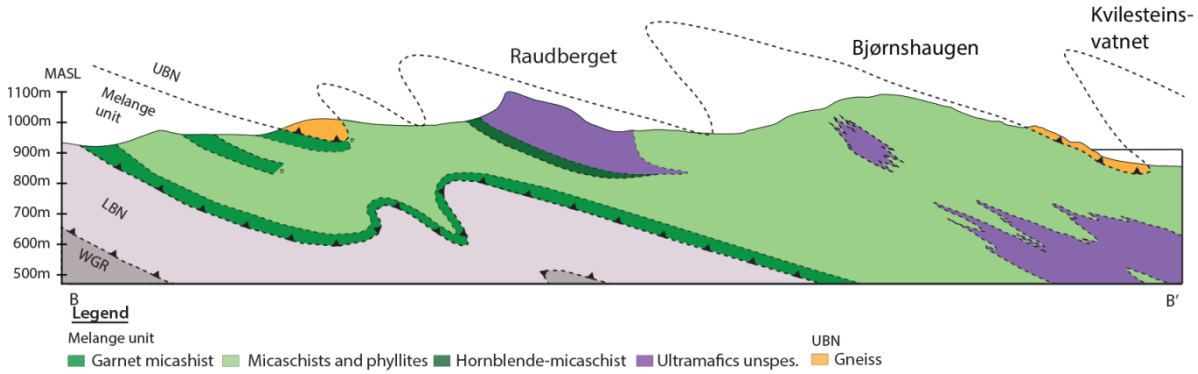

Fig. 6.5: Simplified cross-section between B-B'. See map in appendix 1 for location of cross-section. WGR: Western Gneiss Region LBN: Lower Bergsdalen Nappe UNB: Upper Bergsdalen Nappe. The presence of the ultramafic rocks found underneath Bjørnshaugen is based on drill core data and cross sections from Bakke (1986). The most distinct feature is the overturned top-to-the-NW orientated folds. The uppermost unit (UBN) is observed on two locations in the study area.

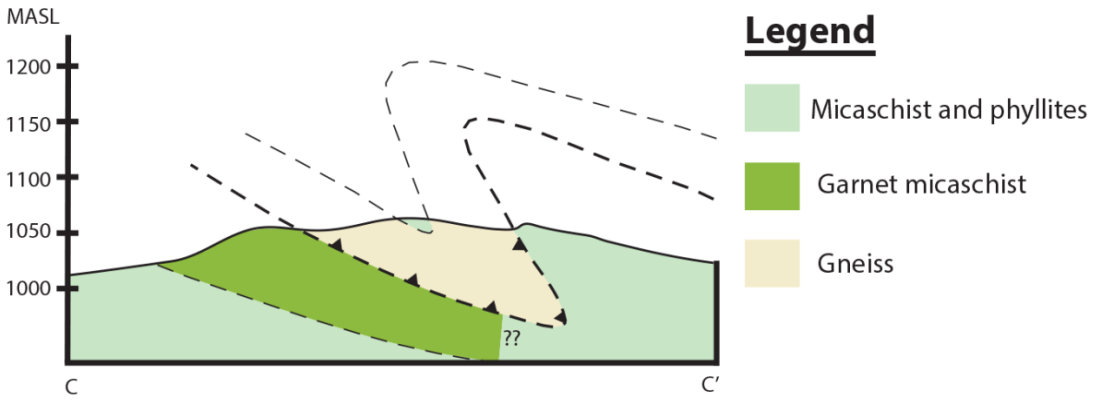

Fig. 6.6: Cross-section between C-C' see appendix 1 for location. The cross-section shows a overturned synform indicating a top the NW shear direction.

6.3 Kinematic indicators

In the study area the dominating shear sense gives a top to the NW shear direction. This shear direction is visible both small scale quartz veins (fig. 6.9A) found in the metapelites and one large scale in the general fold pattern as shown by the cross-sections (fig. 6.4-6.6). This is also visible in the fracture system in Raudberget (fig. 6.7).

As explained above a top to the NW shear direction is associated with the extensional tectonics following the Caledonian collision.

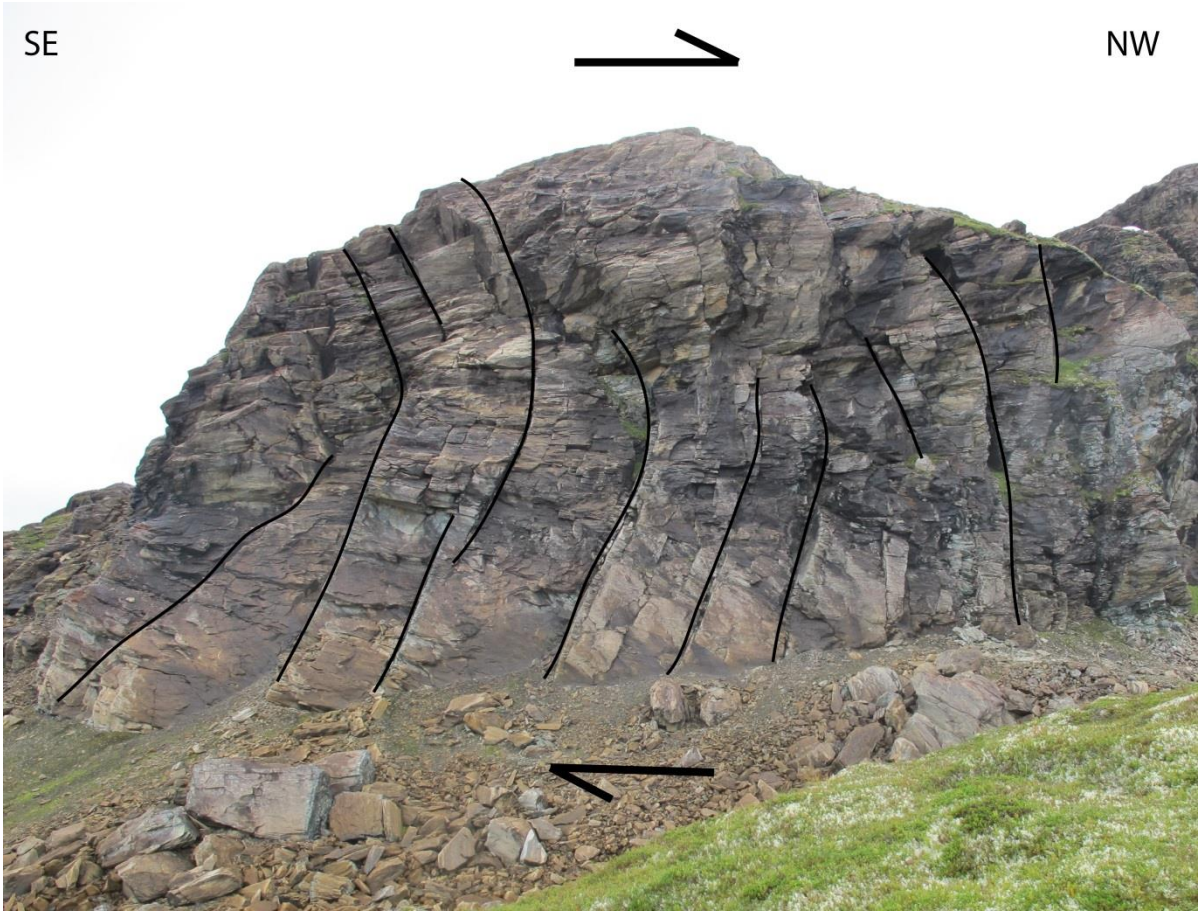

Fig. 6.7: Fracture system in Raudberget, giving a top to the right (NW) shear sense of D2 age. Photo taken on the north-eastern side of Raudberget, towards the south-west. Outcrop is ca. 50m tall.

The simplified explanation of the formation of the fracture system visible in Raudberget is shown in fig 6.8A and B.

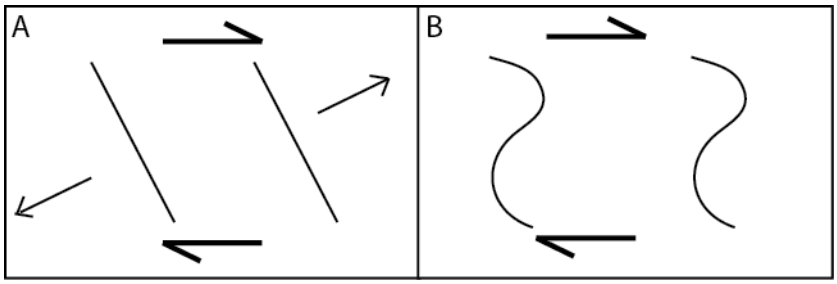

Fig. 6.8: Simplified explaining of the formation of the fracture pattern in Raudberget. A: opening if the fractures by extensional forces related to (simple) shear deformation. B: Rotation of the fractures by continuing shear movement during the D2 deformation stage.

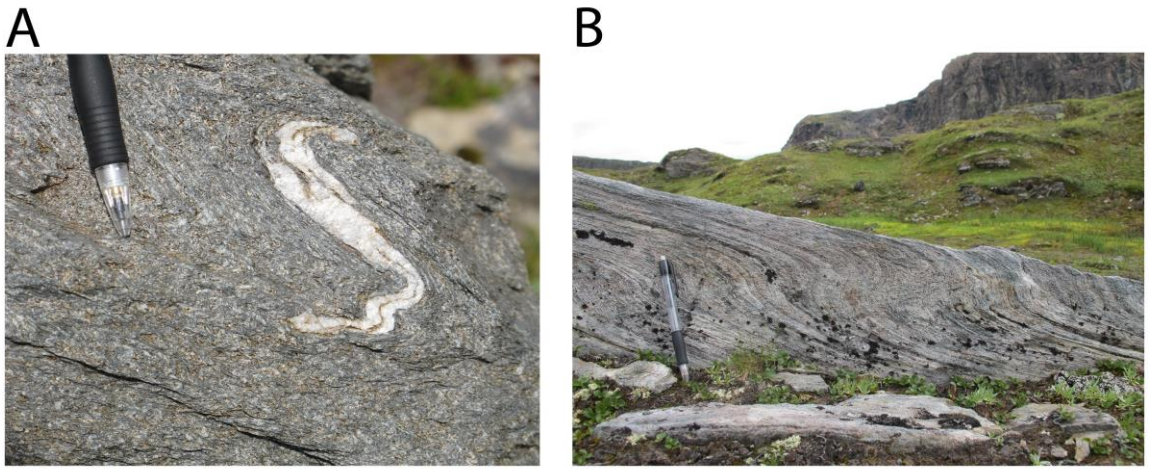

Fig. 6.9A: A folded quartz-vein (D2) in the metapelite, showing asymmetric and vergence to the left (NW). This suggests a top to the NW sense of shear during the D2 deformation stage. B: Folded gneiss banding in gneiss sheet found north of Raudberget. Picture taken eastwards with dip in folded banding towards the SE. Possibly showing the D1 deformation stage. Pencil for scale.

Even though top to the NW is by far the dominant shear sense in the area, some lithologies show a shear sense with top to the SE (fig. 6.9B). This outcrop shows a part of the gneissic rocks NW of Raudberget. The top to the SE shear direction is an older structure and is most likely of the same age as the D1 deformation found in the Bergsdalen nappes (see above).

7. Metamorphism

Previous works in the adjacent areas of this thesis have looked into the metamorphic conditions during the Caledonian orogeny. Fauconnier *et al.* (2014) used Raman Spectroscopy of carbonaceous material to estimate peak metamorphic temperatures during the orogeny. They found temperatures ranging from 314-515°C (fig. 7.1).

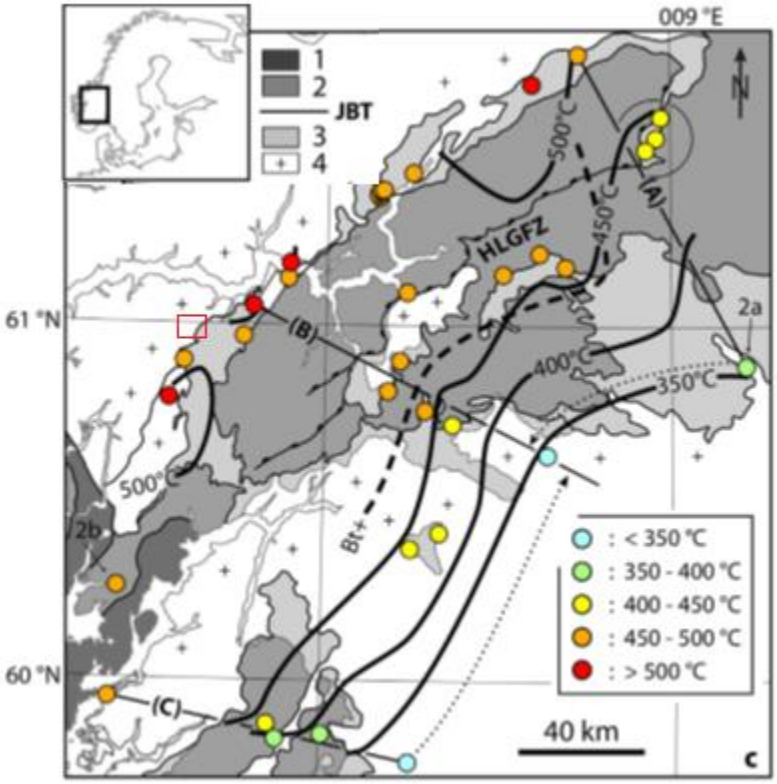

Fig. 7.1: Peak temperatures during the Caledonian orogeny in the western parts of south Norway. 1: Upper Allochthon 2: Middle Allochthon 3: Lower Allochthon and Baltica cover 4: Baltica basement. Approximate location of study area of this thesis marked with red. From Fauconnier et al. (2014).

The highest temperature they found (515°C) was from a sample taken a few kilometre south of Raudberget.

The Bergsdalen nappes, which the mélange unit is sandwiched between, experienced ductile deformation of uppermost green schist to lower amphibolite facies during the Caledonian orogeny (Fossen, 1993b).

In this thesis the peak metamorphic conditions during the Caledonian orogen is calculated by use of bulk rock composition and mineral assemblage together with *Theriak-Domino* (de Capitani and Brown, 1987; de Capitani and Petrakakis, 2009; de Capitani and Petrakakis, 2010). The theoretical mineral assemblage given by the software is compared to the mineralogy found in thin-sections of the samples. This gives a peak pressure and temperature interval. The interval of the *P-T* conditions is dependent upon the stability fields of the mineral assemblage. The larger variation of *P-T* conditions the specific mineral

assemblage is stable, the larger interval in pressure and temperature is given by the software.

The *P-T* interval can be better defined by using geochemistry of specific minerals. Two of these minerals are white mica and garnets. Garnets are stable at a wide range of metamorphic conditions, and commonly preserve the *P-T* history of the host rock through compositional zonation (Tirone and Ganguly, 2010). The diffusion rate in garnets is also low enough to preserve the compositional zonation of the crystal (Konrad-Schmolke *et al.*, 2005). This makes garnets a good indicator for *P-T-t* path. The number of Si atoms in white mica varies dependently upon *P-T* conditions. These two minerals are therefore good indicators of peak pressure and temperature. The method for mineral chemistry is given above.

Sample	30-14	53-14	65-14
Element	Mol	Mol	Mol
Si	47,0	53,4	46,9
Ti	0,9	0,7	0,8
Al	26,9	24,6	15,5
Fe	7,0	8,7	11,2
Mn	0,3	1,5	0,2
Mg	3,7	2,2	10,8
Ca	2,4	1,2	10,6
Na	6,2	3,3	3,7
K	5,7	4,5	0,3
Sum	100,0	100,0	100,0

Table 7.1: Wt% oxide from the XRF recalculated into mole for the samples used in Theriak-Domino

Three samples were chosen for a detailed study of the peak metamorphic conditions, two garnet micaschists and one garnet amphibolite. The localities of the samples are given in appendix 2. Table 7.1 gives the oxide wt% of the samples (appendix 3), recalculated into mole fractions and are the basis for the plots given below. All three samples are run between 3000-10000 bars (0,3-1GPa) and 400-600°C.

7.1 Garnet micaschist (Sample 30-14)

Sample 30-14 is a garnet micaschist taken NW of Raudberget (see appendix 1). The sample in question contains garnets, feldspar, biotite, white mica (muscovite), chlorite and quartz. Fig. 7.2 shows the theoretical stable mineral assemblage for the specific bulk rock composition of this rock sample between 400-600°C and 3000-10000 bars. The area of the diagram that contains these minerals is highlighted in yellow. In addition there is a minor content of calcite in the sample. Since the sample contains garnets, all mineral assemblages that do not contain garnets have been removed to tidy up the figure and make it easier to read.

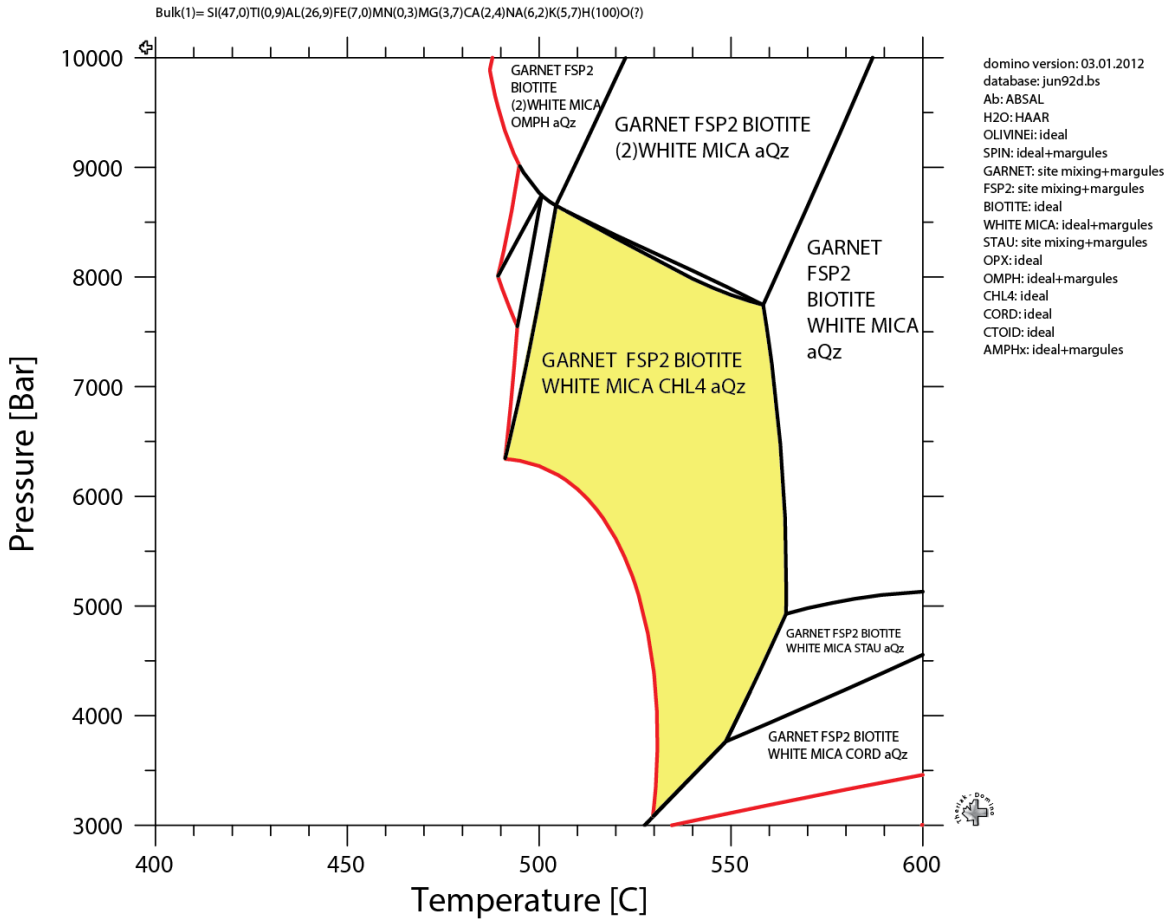

Fig. 7.2: Stable mineral assemblages for the specific bulk rock composition of sample 30-14. Highlighted area (yellow) marks the assemblage that corresponds to the sample. Red line marks the first appearance of garnet.

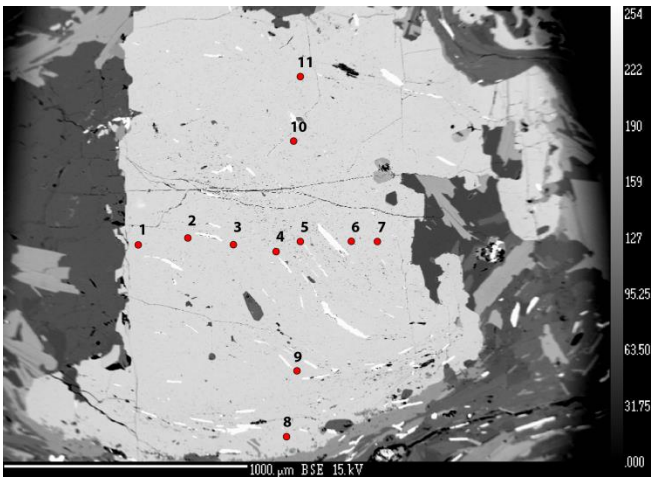

Fig. 7.3: Data points location used as basis for the garnet end member calculation

The mineral assemblage in the highlighted area covers a pressure interval of ca. 3100-8600 bar and 480-560°C. By using garnet end member composition and Si content per formula unit (SIPFU) in white mica, the *P-T* interval can be better defined for the bulk rock composition. Table 7.2 shows 11 data points taking in the EMP of the same garnet, recalculated into garnet end members. The data points show two profiles through the garnet (fig. 7.3).

Table 7.2: EMP results of one of the garnets in the sample. The points show two profiles of the garnet crystal. Profiles 1 (point 1-6) are data points taken across the crystals and profile 2 (point7-11) are data point taken from bottom to top of the crystal (see figure above).

Garnet type	Profile 1						Profile 2					Min	Max
	Pt number						Pt number						
	1	2	3	4	5	6	7	8	9	10	11		
Almandine	71,01	70,21	70,82	70,10	71,17	71,05	71,04	69,85	70,81	71,60	74,17	69,85	74,17
Pyrope	4,01	3,88	3,84	3,89	4,07	4,02	4,23	4,78	4,06	3,98	4,74	3,84	4,78
Grossular	20,15	19,47	19,05	20,25	19,90	19,43	19,82	22,69	20,16	20,04	19,41	19,05	22,69
Spessartine	4,82	6,44	6,29	5,75	4,86	5,50	4,91	2,68	4,97	4,37	1,68	1,68	6,44

Fig. 7.4-7.6 shows the composition of three of the garnet end members (almandine, grossular and pyrope), based on table 7.2. The plots show the change in end member composition of each of the garnet variants with steps of 1%. The plots have the stable mineral assemblages (fig. 7.2) as a background. The highlighted area shows the difference between the minimum and maximum end member composition. By combining the three end members, they should give an area of the plot where they all overlap each other. This can then be used to limit the peak pressure and temperature of the metamorphism during the Caledonian orogeny.

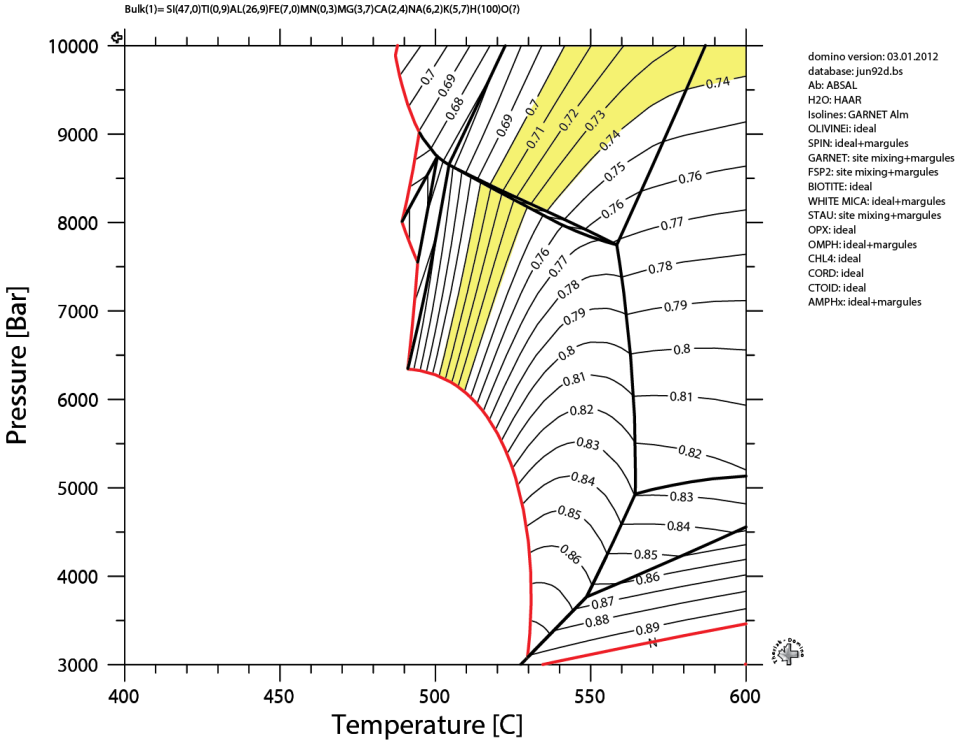

Fig. 7.4: End member almandine composition in sample 30-14. The isolines show area calculated with 1% steps between 60%-90% almandine. The highlighted area (yellow) shows the percentage of almandine analysed garnet. Stable mineral assemblage as a background.

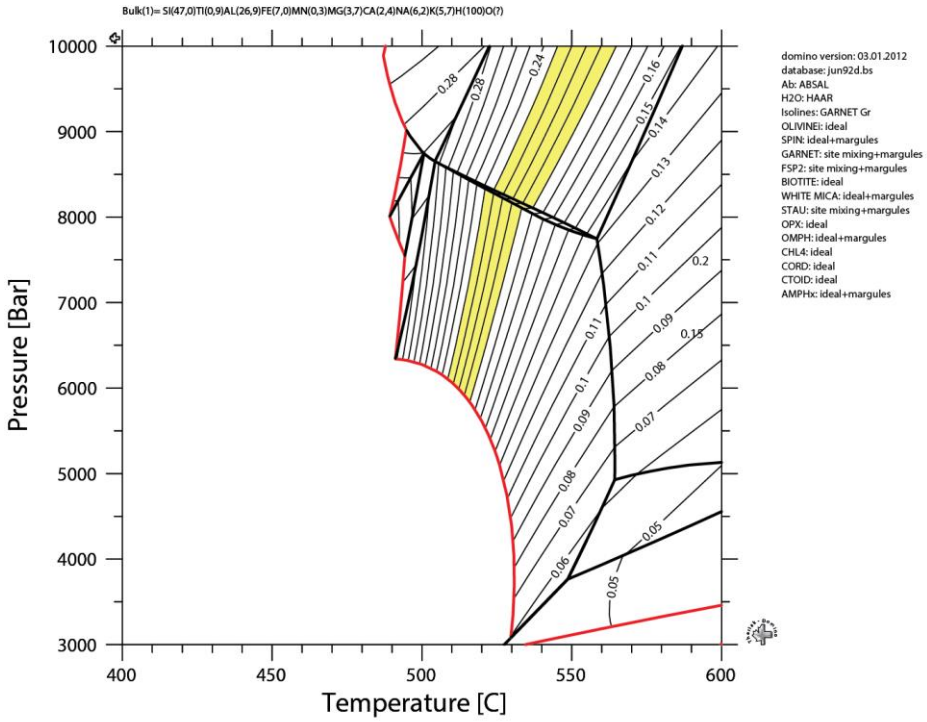

Fig. 7.5: End member grossular composition in the sample. The isolines show area calculated with 1% steps between 0%-30% grossular. The highlighted area shows the percentage of grossular in the analysed garnet.

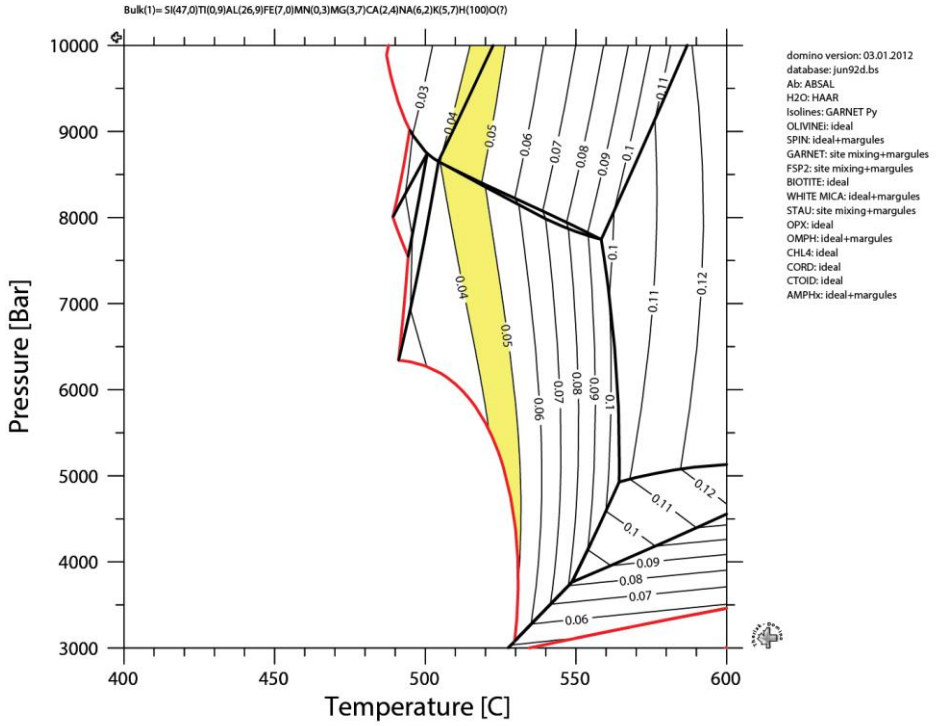

Fig. 7.6: End member pyrope composition in sample 30-14. The isolines show area calculated with 1% steps between 0%-15% pyrope. The highlighted area shows the percentage of pyrope in the analysed garnet. Stable mineral assemblage as a background.

All three of the garnet end members have compositions that overlap the stable mineral assemblage. Since the garnet have a stable composition of the three end members (table 7.2), with only small changes between minimum and maximum value, the areas covered in the plot by each of the end member is small. Small variation in the garnets composition has potential to give the best *P-T* estimate, because the overlapping area will be smaller. All three of the garnets reduce the peak temperature interval, and show that the peak temperature lies in the lower half of the estimate based solely on the mineral assemblage.

The end members show a compositional change as a function of both pressure and temperature. In the selected temperature and pressure interval the compositional change seems to be most depended on pressure, rather than temperature. This is especially the case for pyrope which only has a minor temperature impact on the end member composition.

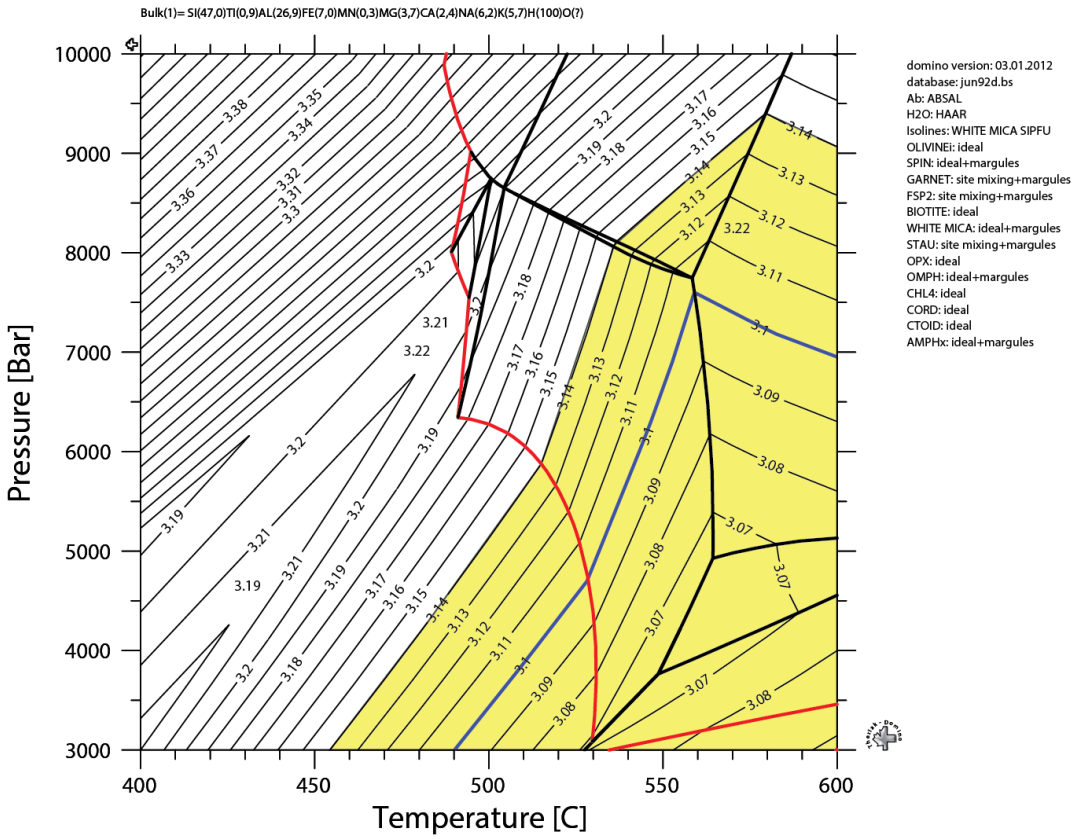

Fig. 7.7: The change in Si content in white mica. The highlighted area shows the interval between the minimum and maximum Si, with the blue line (at 3.10 Si) showing the average.

Fig. 7.7 shows the change in white mica SIPFU. The analysed muscovite contains between 3,05-3,14 Si atoms per formula unit, with an average of 3,10 (blue line). The figure shows

the theoretical content of Si in the same *P* and *T* regime as the other plots for the same sample. The highlighted area in yellow shows the Si content in the white micas found in the sample.

Like the garnet end members, the number of Si atoms in white mica change dependently upon the metamorphic conditions. In the pressure and temperature regime covered by the plot (fig. 7.7), the general trend is that a higher temperature reduce the Si atoms down to 3,07 at ca. 4500 bars. Lower temperatures show a higher Si content. The trend seems to reverse on temperatures above 580^{o}C. The number of Si atoms also varies dependently upon pressure. Higher pressure, especially at lower temperatures, give a higher SIPFU number than lower pressure.

The Si content of the muscovites has a fairly large variation between the minimum and maximum value. This result in the SIPFU in white mica covers large areas of the plot. Unlike the garnets, SIPFU alone is not enough to define the peak pressure and temperature more than just based on mineral assemblage.

Fig. 7.8 combines all the garnet and Si in white mica together with the mineral assemblage to estimate the maximum *P* and *T*. The cross hatched area show the overlapping area of all the three end member garnets (fig. 7.4-7.6) and the highlighted area in yellow show the Si content in white mica (fig. 7.7).

The three garnet end members overlap each other in the part of the plot with the corresponding mineral assemblage of the sample. The overlapping garnets give a *P* and *T* interval of ca. 6100-8000 bars (0.61-0.8GPa) and c. 510-525^{o}C. White mica Si only just overlaps the garnets, suggesting that the maximum pressure lies towards the lower end of the interval and that maximum temperature is in the upper half of the temperature interval.

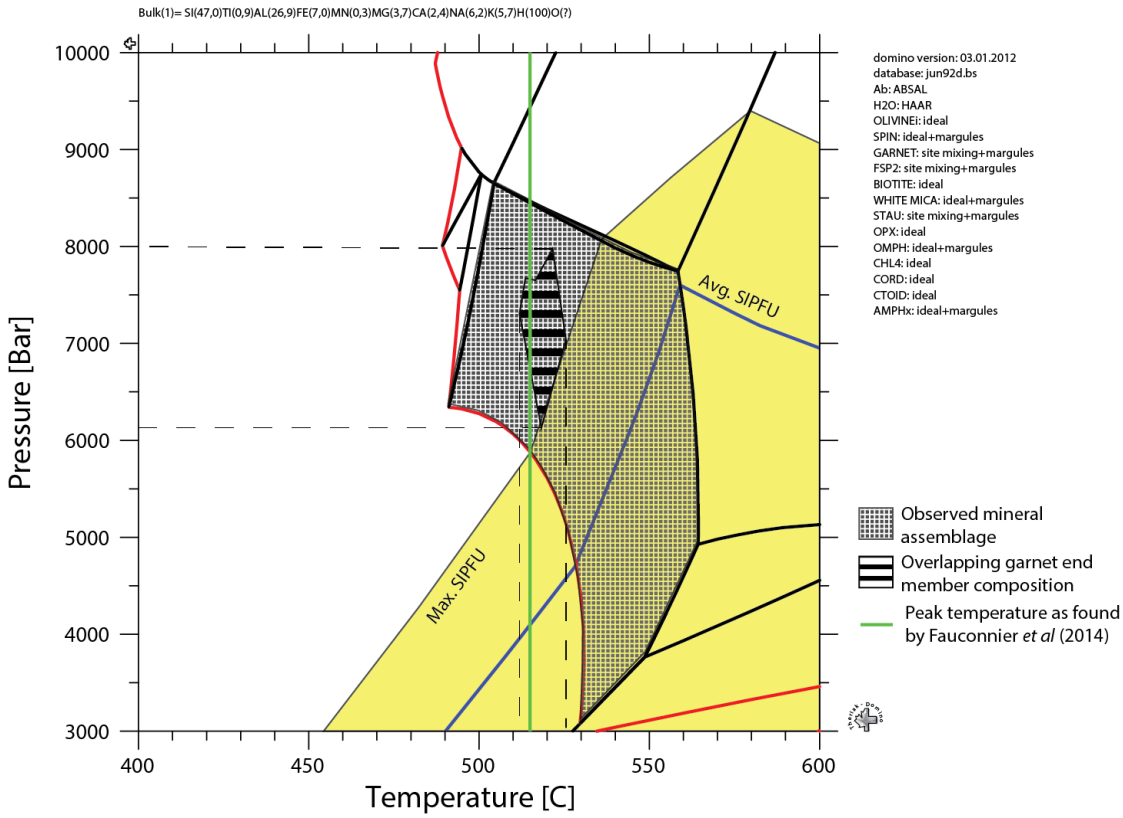

Figure 7.8: Combination of the garnet end members and sipfu in white mica plots. The cross hatched area show the area where all of the three garnet end members are overlapping each other. The highlighter area (yellow) shows the interval between maximum and minimum sipfu in white mica, as shown in figure 36 with the average marked in blue. The green line marks the maximum temperature Fauconnier et al (2014) found in the area

7.2 Garnet micashist (Sample 53-14)

Sample 53-14 is a garnet micaschist containing garnet, feldspar, biotite, white mica, chlorite and quartz. The sample is taken in the most NW part of the study area (see appendix 1). Sample 30-14 and 53-14 is very similar in mineralogy, but there are some differences in element composition. Sample 53-14 has a much higher Mn component than sample 30-14. There is also a large (relative) difference in Mg, Ca and Na (table 9). Since the bulk rock composition is so different, the stable mineral assemblage will be different. Fig. 7.9 shows the theoretical stable mineral assemblages as given by the specific bulk rock composition between 400-600^{o}C and 3000-10000 bars. There are two areas that match this mineral assemblage as the figure show. The difference between the two areas is a slight change in

feldspar composition. The mineral assemblage gives a peak temperature of somewhere between 470°C and 515°C and a peak pressure of up to 9500bars.

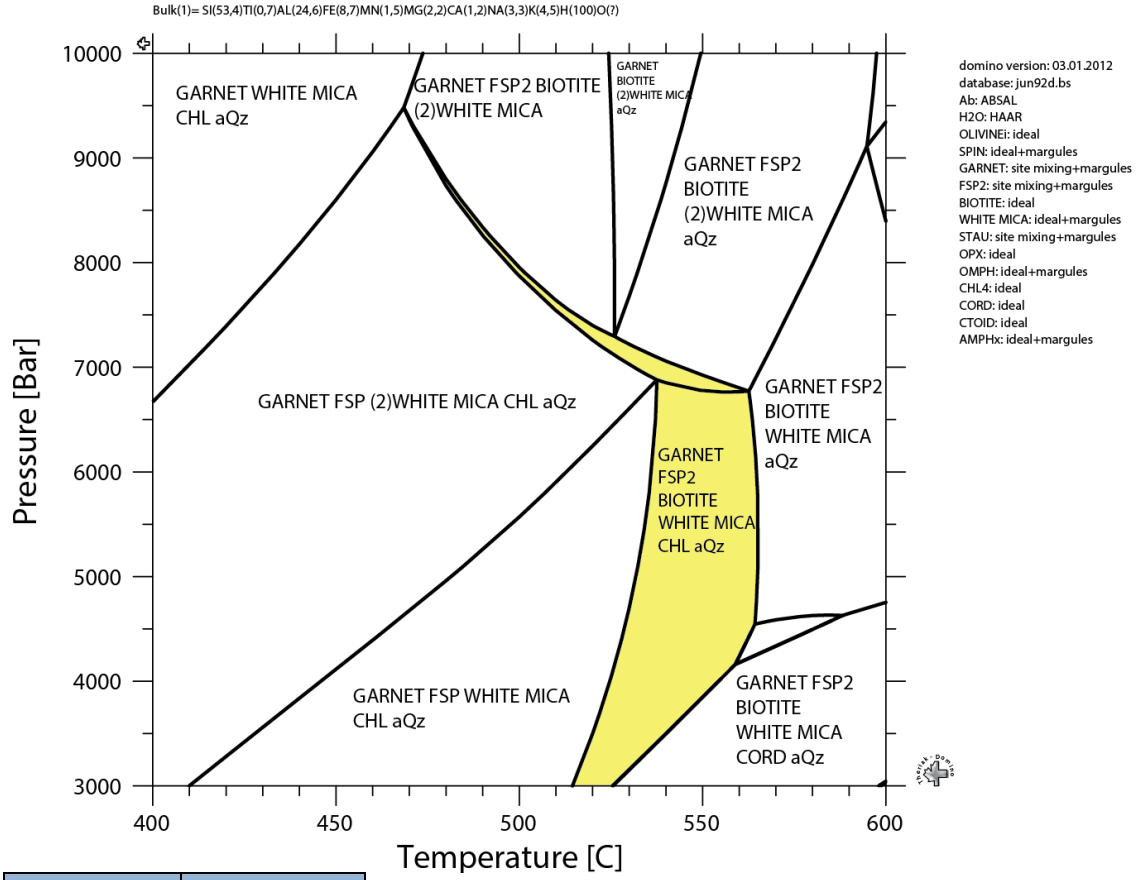

Fig. 7.9: Theoretical stable mineral composition with the given bulk rock composition of sample 53-14, between 400-600°C and 3.000-10.000 bars. The highlighted areas (yellow) show the mineral assemblage corresponding with the sample.

Garnet type	Pt number	
	9	10
Almandine	75,15	70,34
Pyrope	6,32	4,34
Grossular	10,19	11,22
Spessartine	8,32	14,08

Table 7.3: Garnet end members in sample 30-14 used in thermobarometric calculation

Table 7.3 shows the basis of the garnet end member compositions. Unlike sample garnet used in 30-14, the garnets in this sample have a clear element zonation (see fig. 5.20). The data points have therefore been selected to give a best possible equilibrium with the surrounding minerals. The data points selected are the last two points of the profile in fig. 5.20.

Fig. 7.10 show the almandine end member composition in the garnet based on table 7.3. The figure shows that almandine composition is almost only dependent upon temperature, at least up to 70% almandine and ca. 500°C in the *P-T* regime covered by the figure. Up to

this point the composition of almandine change fairly regularly. Above this the composition is more stable and pressure influences the composition to a greater degree.

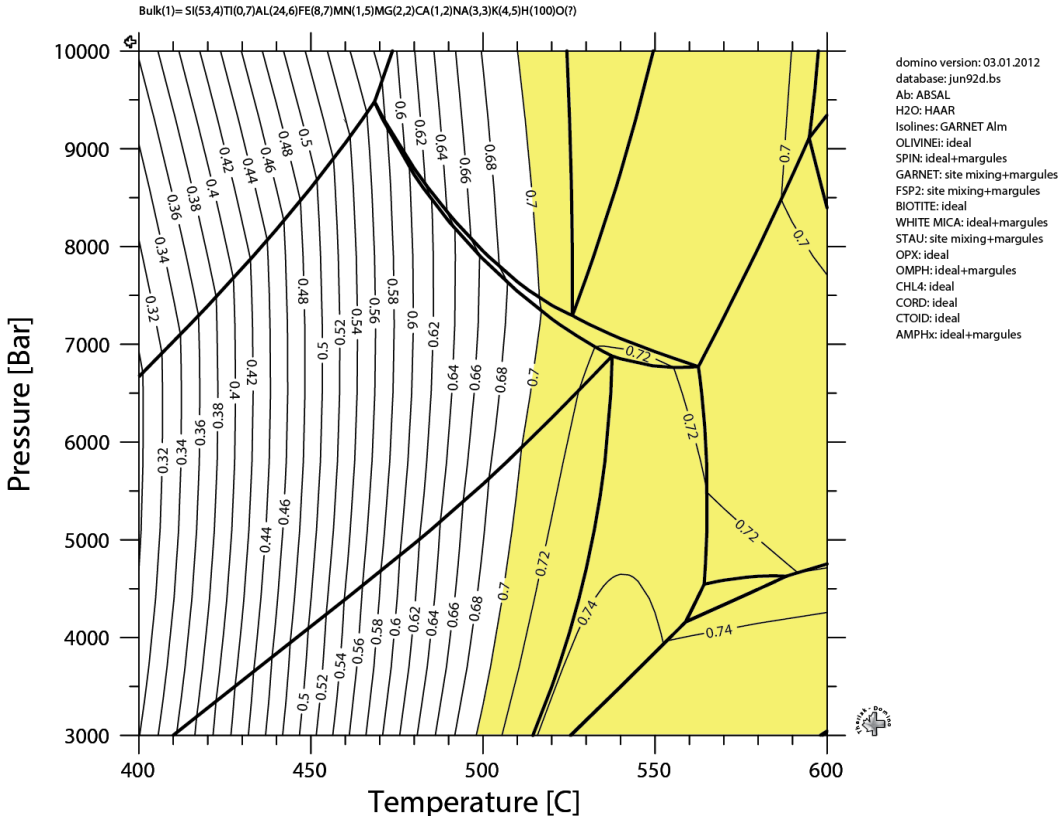

Fig. 7.10: End member almandine composition. The isolines show area calculated with 2% steps between 30-80% almandine. The highlighted area shows the percentage of almandine in the garnets.

Table 7.3 shows that the composition of this garnet end member varies between 70-75%. This corresponds to a large area in fig. 7.10. The almandine composition covers all plotted values of pressure above 510^{o}C. Almandine cover one of the sections with the corresponding mineral assemblage entirely and the higher temperatures for the other section of the plot with the same mineralogy. This means that almandine alone is not enough to limit the peak metamorphic conditions.

Fig. 7.11 shows the grossular component of the garnet in the sample, based on table 7.3. The figure shows that grossular component in the garnet for this bulk rock composition and *P-T* regime, vary as a function of both pressure and temperature. The grossular component has a small variation between 10,2-11,2%. This means that the area of the plot corresponding to this end member will be small.

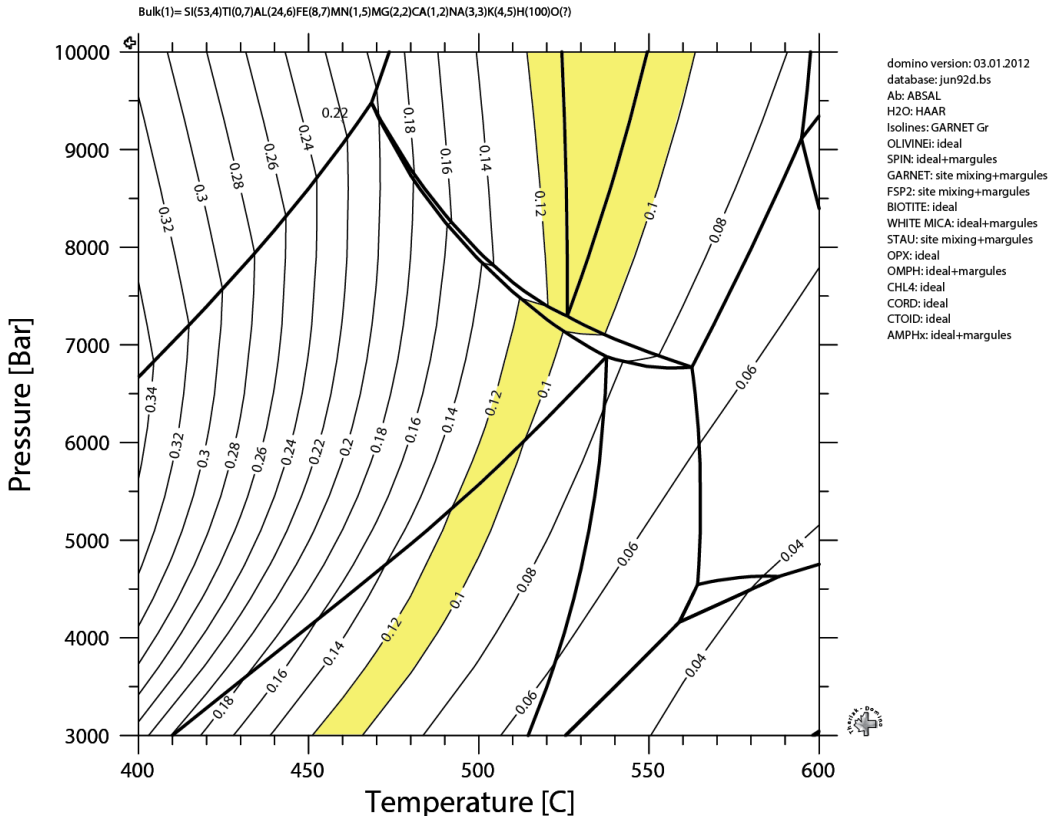

Fig. 7.11: End member grossular composition. The isolines show area calculated with 2% steps between 4-34% grossular. The highlighted area shows the percentage of grossular content in the garnets.

Unlike the almandine component, grossular only covers one of the fields with the corresponding mineral assemblage, ruling out one of the compositions. Because the end member only covers one of the mineral assemblages, together with the small component variation, the peak *P-T* conditions can be very well defined. The pressure interval is reduced to only a few hundred bars and the peak temperature is reduced to ca. 510-540^{o}C.

Fig. 7.12 shows the pyrope composition of the garnet. Table 7.3 show that the pyrope component lies between 4,3-6,2%. For this specific bulk rock composition and *P-T* regime, the pyrope end member is solely dependent on pressure, and do not vary as a function of temperature. Just like grossular, pyrope component only covers one of the corresponding mineral assemblages. In addition pyrope excludes the higher end of the peak temperature of the composition. Because of the small variation in component and relatively small variation in of the fields in the plot, the peak temperature and pressure conditions can be defined with only a small interval.

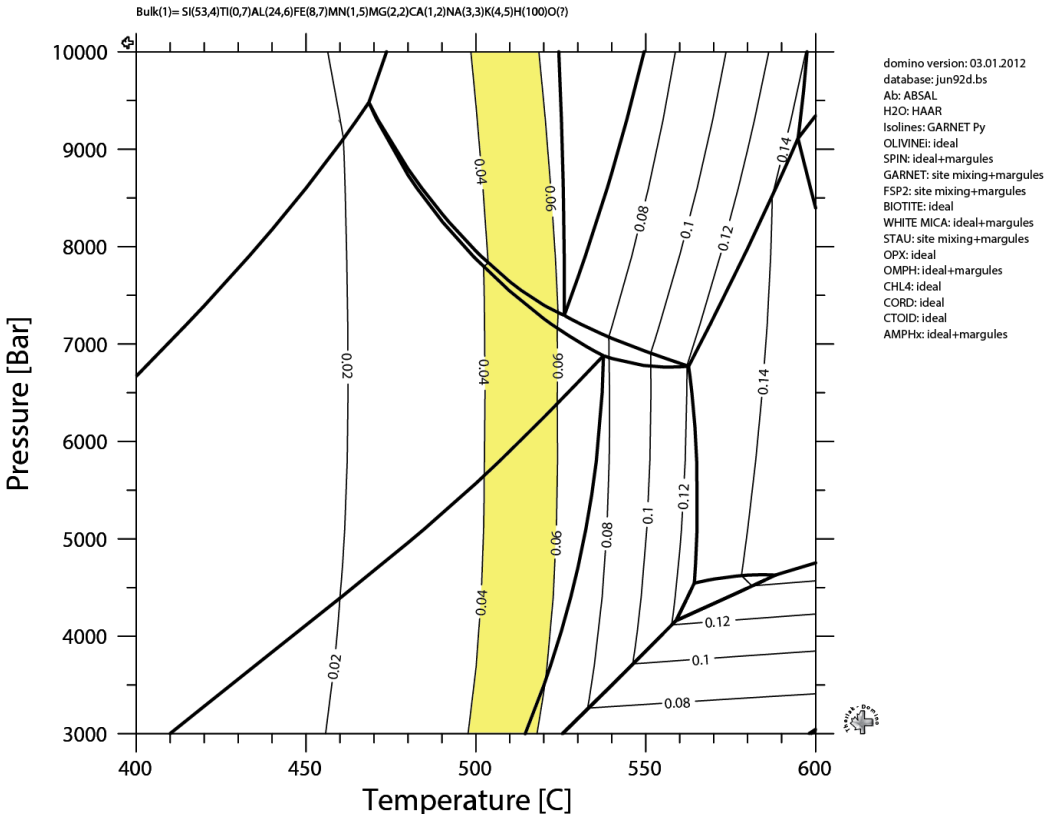

Fig. 7.12: End member pyrope composition. The isolines show area calculated with 2% steps between 0%-20% pyrope. The highlighted area shows the percentage of pyrope content in the garnets.

The pressure interval in pyrope component is larger than in grossular, so the peak pressure cannot be reduced more be solely looking at pyrope. The temperature on the other hand can be reduced. Grossular gives a temperature between 510-540°C (see above), while pyrope gives a peak temperature of 500-525°C. By combining these two end members the peak metamorphic temperature is most likely in the overlapping gap, between 510-525°C. Fig. 7.13 shows the Si content in the white micas. The amount of Si varies between 3,03-3,15 atoms per formula unit, with an average of 3,09. In contrast to the garnet end members white mica SIPFU covers a large area of the plot, and includes both of the mineral assemblages. White mica SIPFU rules out the lower end of the temperature interval, but cannot be used to define the peak metamorphic conditions any further.

Fig. 7.14 is a combination of all the garnet end member plots, SIPFU in white mica and the stable mineral assemblage (fig. 7.10-7.12). The cross hatched area show where the garnet end members overlap and the highlighted area in yellow show the interval of SIPFU in white mica, with the blue line as the average, as in fig. 7.13.

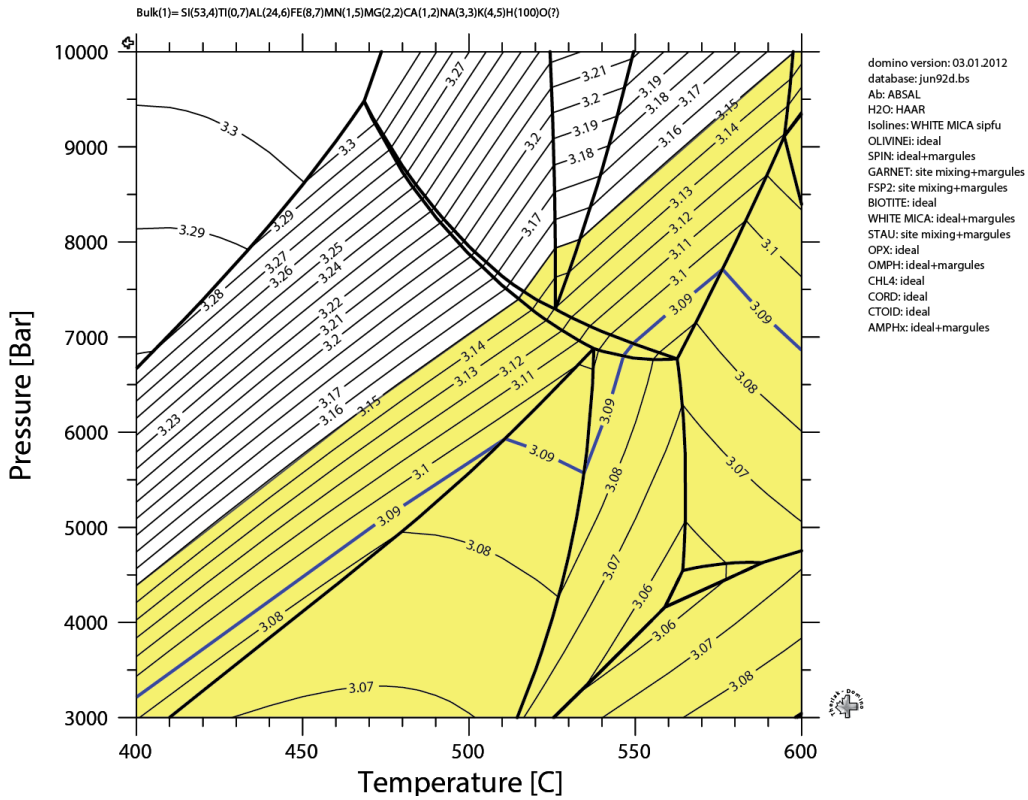

Fig 7.13: The change in Si content in white mica. The highlighted area shows the interval between the minimum and maximum Si, with the blue line showing the average.

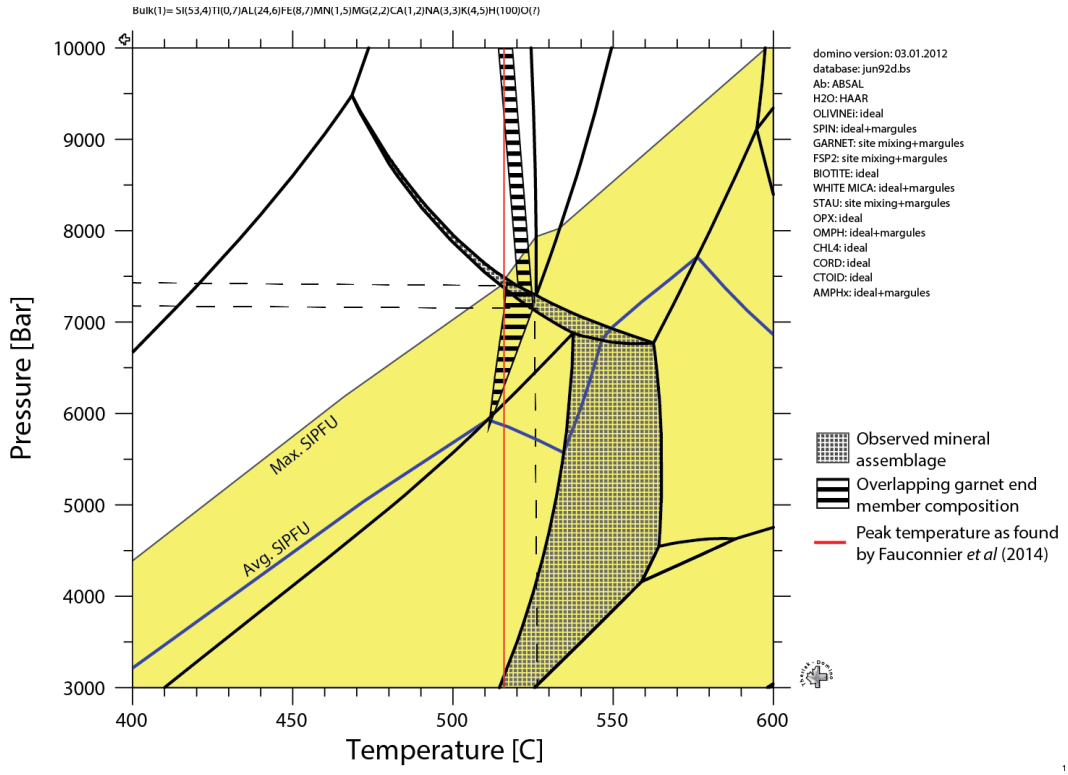

Fig. 7.14: Combination of the garnet end members and sipfu in white mica plots. The cross hatched area show the area where all of the three garnet end members are overlapping each other. The highlighted area (yellow) shows the interval between maximum and minimum SIPFU in white mica, with the average marked in blue

All of the three garnet end members overlap each other in the same area of the plot that has the same theoretical mineral assemblage as the sample. The overlapping garnets give a peak pressure of ca. 7100-7450 bars and a peak temperature of ca. 515-525°C. White mica SIPFU also overlaps this *P-T* regime, and underpins the peak metamorphic conditions found by the garnet end members.

7.3 Garnet amphibolite (sample 65-14)

Fig. 7.15 shows the stable mineral assemblages between 400-600°C and 3000-10000 bars. The red line shows the first appearance of garnet and since the sample contains garnets these assemblages area not of interest and have therefore been removed. Other minerals in the rock are feldspar, chlorite, amphiboles and quartz, highlighted in the figure. Ferro-pargasite (FePa) is an end member in the hornblende series and therefore fall in under the amphibole group, even thou the program do not include it under AMPHx in the figure.

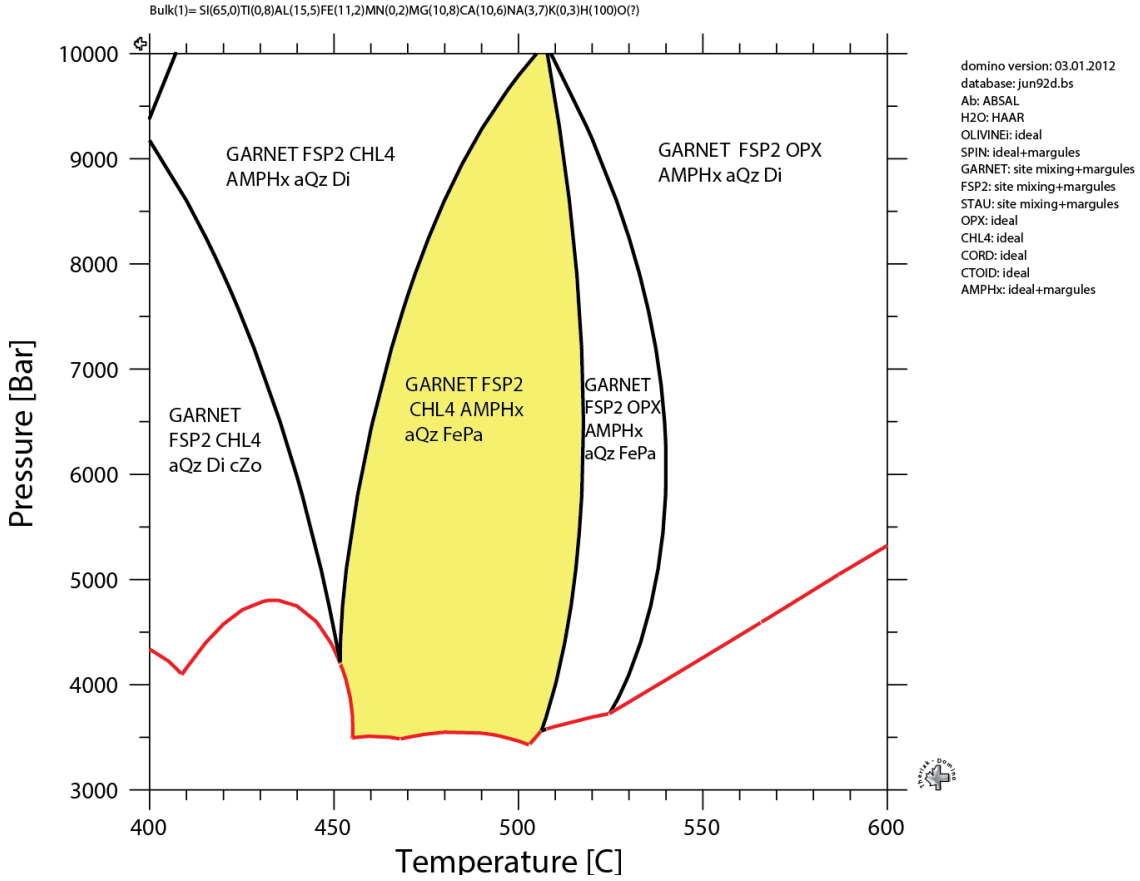

Fig. 7.15: Theoretical stable mineral assemblage for the garnet amphibolite (sample 65-14) between 400-600°C and 3000-10000 bars. The highlighted area shows the same mineral assemblage as the sample. The red line shows the first appearance of garnet.

Table 7.4: Garnet end member composition in the garnet amphibolite

Garnet type	Pt number						Min	Max
	1	2	3	4	5	6		
almandine	52,97	52,88	51,96	55,26	55,86	55,50	51,96	55,86
pyrope	11,32	10,38	11,93	10,25	8,86	11,21	8,86	11,93
grossular	30,89	35,35	34,52	31,07	31,66	30,15	30,15	35,35
spessartine	4,82	1,39	1,59	3,42	3,61	3,14	1,39	4,82

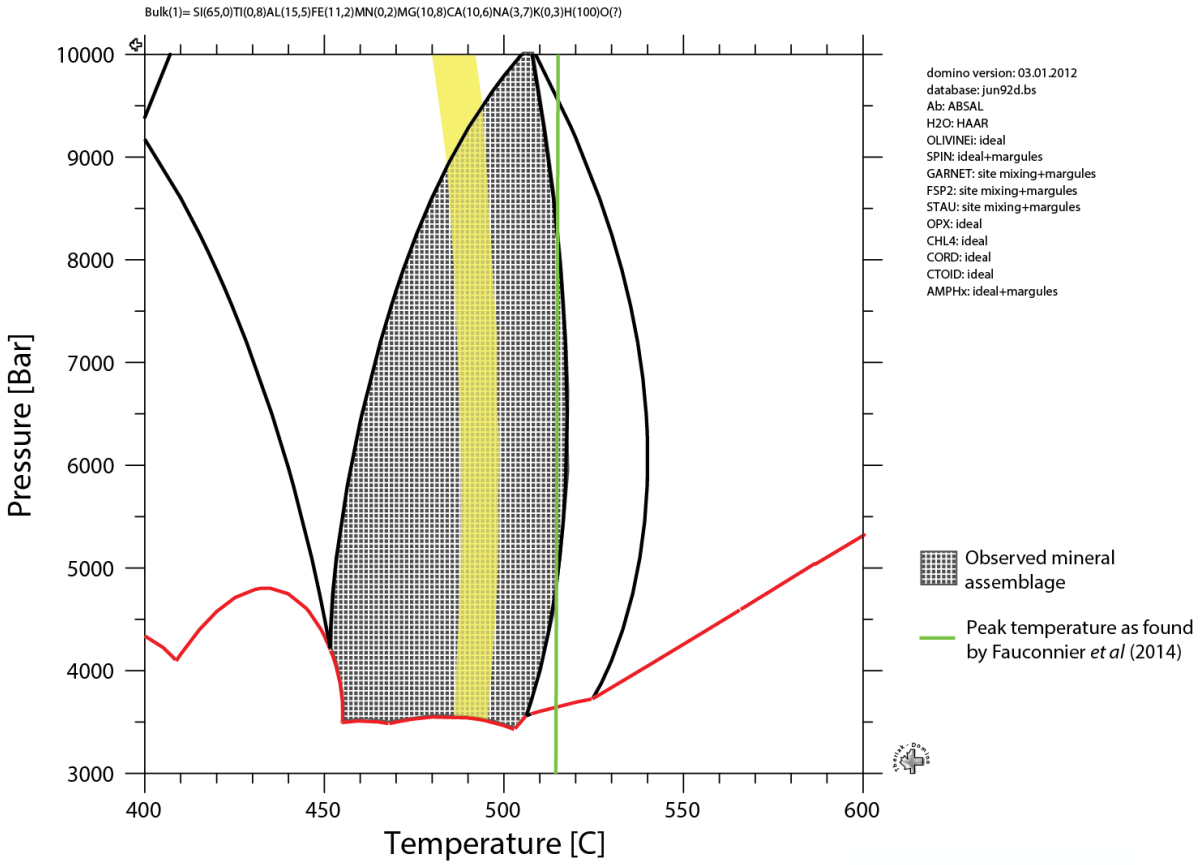

Fig. 7.16: Almandine end member component with the stable mineral assemblage as a background. Only almandine plots in the same area as the mineral assemblage. Maximum temperature given by the garnet is ca. 500°C. The green line at 515°C shows the maximum temperature found by Fauconnier et al. (2014).

The almandine content in the garnets in the sample lies between 52-56% (table 7.4). This composition is marked in fig. 7.16. The mineral assemblage gives a maximum temperature between 450-520°C and a maximum pressure of 3500-10000 bars. By using the almandine component of the garnets, the maximum temperature can be narrowed in to between 480-500°C. None of the garnets overlap each other in *P-T* interval with the correct mineral assemblage, so limiting the pressure interval any further is not possible with this method.

8. Discussion

8.1 Metamorphism

8.1.1 Peak metamorphic conditions

The metamorphic grade of D1 deformation (M1) is constrained by growth of white mica, biotite, amphibole, garnets and the coexistence of oligoclase and albite in the Bergsdalen nappes (Kvale, 1946). This indicates lowermost amphibolite facies metamorphic conditions in these nappes. M2 metamorphism in the Bergsdalen nappes related to the D2 deformation show a somewhat lower metamorphic grade then during D1 deformation. This is apparent in the formation of D2 fabrics where M1 generation garnets have been cracked (see fig. 5.17) and replaced with biotite and chlorite in the phyllites and micaschists in the Bergsdalen nappes. In the granitic and quartzitic rocks of the Bergsdalen nappes retrogression is only found in the quartz shape fabrics of D2 age, which may indicate lower recrystallization rates and a lower temperature then the D1 deformation (Fossen, 1993b). Because the Bergsdalen nappes are situated so close to the mélange unit, the metamorphic conditions in these nappes are most likely mirrored in the mélange unit.

Both of the garnet micaschists samples analysed with the *Theriak-Domino* software show similar peak *P-T* conditions. Sample 30-14 gives a peak pressure of between 6100-8000 bars and sample 53-14 give a peak pressure of 7100-7450. Both of the samples give a peak pressure in the same area, but while sample 30-14 has a pressure interval of 1900 bars, sample 53-14 only differs 350 bars from minimum to maximum peak pressure. While the peak pressure interval varies substantially between the two samples, the peak temperature interval is almost the same. Sample 30-14 gives a peak temperature between 510-525^{o}C, and sample 53-14 give a temperature of 515-525^{o}C. The two intervals overlap between 515-525^{o}C, suggesting a peak metamorphic temperature in the range between these two values.

The garnet amphibolite (sample 65-14) gives a much higher pressure interval because of the large stability field of the mineral assemblage. In addition the garnet end members do

not overlap each other in the *P-T* regime given by the garnet micaschist and by Fauconnier *et al.* (2014), only the almandine component fall within the observed mineral assemblage in the diagram. The peak pressure is therefore not possible to define using this method for this lithology. The original database plot omphacite in every stable mineral assemblage within the chosen *P* and *T*. Omphacite is a clinopyroxene found exclusively in (U)HP and high *T* metamorphosed rocks, like eclogites (e.g. Nesse, 2013). Since the maximum metamorphism only reached medium *P* and *T*, there is little surprise that there are no omphacite in the sample. The mineral was therefore removed from the database (see chapter 4.6) to see if that would give a mineral assemblage closer to the observed assemblage. Even though this gave a better result, it shows that the uncertainties are larger for this sample than for the garnet micaschist, where both samples show the sample result in the expected *P-T* area. The increased uncertainty is most likely due with the database. XRF analyses are very accurate, especially when only looking at major components. The risk of sample contamination in preparation of the XRF analyses is also small, leaving the database used in the program suite. The garnet amphibolite gives a peak temperature between 480-500^{o}C, 15^{o}C lower than the lowest temperature given by the garnet micaschist.

Fauconnier *et al.* (2014) did Raman Spectroscopy of carbonaceous material in the Stølsheimen area. They found a peak temperature to be between 314-515^{o}C (fig. 7.1), with an average scatter of ±25^{o}C. The sample showing the highest temperature was taken a few kilometres south of the study area of this thesis. This fits well with the thermobarometric results found based on the *Theriak-Domino* software as used in this thesis. Both of the garnet micaschists have a peak temperature around 515^{o}C. The garnet amphibolite shows a slightly lower temperature of maximum 500^{o}C. The bell shaped zonation in the garnets found in the garnet micaschist also supports low to medium grade metamorphism. Bell shaped zonation of MnO is often absent in high grade metamorphic rocks, but is common in lower grade metamorphism (Woodsworth, 1977). Fossen (1993b) showed that the Bergsdalen nappes were exposed to lowermost amphibolite facies conditions during D1 deformation. The thermobarometric results from *Theriak-Domino* based on bulk rock composition of the garnet micaschists from the study area, gives a peak metamorphic

conditions in the intersection of upper greenschist and lower amphibolite facies (Winter, 2014). Results from the ultramafics also indicate greenschist facies metamorphism Enger (work in progress).

8.1.2 Black-wall alteration

In the theoretical relations between an ultramafic body and the surrounding country rocks there is several different lithologies (see fig. 5.26). The figure shows reaction zones commonly found between ultramafic bodies and the country rocks at greenschist to amphibolite facies metamorphism. As explained above the metamorphic conditions reached upper greenschist or lower amphibolite facies during the Caledonian orogeny in the study area, so this is the expected lithologies in the reaction zone. This theoretical layering is best observed at Vetle Raudberget, but is only partly met. At Raudberget the talcified zone and the Ca-amphiboles are not found in contact with each other. The blackwall altered schists are only found at the NW flank of the mountain and the talc is only found at the southern flank (appendix 1 and fig. 5.2). This is most likely due to the Caledonian orogeny affecting the lithologies (Karlsen 1990). Still the general trend is visible with a ring of talc and carbonate, followed by amphibole schist in the blackwall altered parts is easily recognized, especially at Vetle Raudberget.

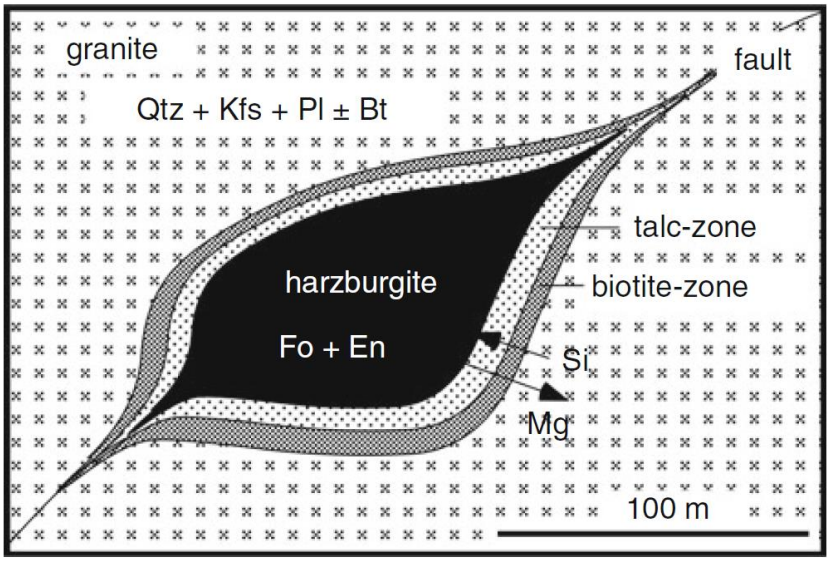

Fig. 8.1: Reaction zone between an ultramafic body and the surrounding host rocks, with talc biotite zones between the two lithologies. The figure show a possible source of the increased MgO in the blackwall schists found in the Raudberget area. From Bucher and grapes

A contact between the Fo-bearing mantle rock and the quartz rich host rock have a large scale disequilibrium feature and the chemical mass transfer between the two incompatible rock types results in encapsulation of the mantle rocks in shells of reaction zones (Bucher

and grapes). Si from the host rock are incorporated into the minerals in the ultramafic rocks and forming talc (Bucher, Capitani Grapes). Both Vetle Raudberget and Raudberget show this talcifed zone towards the host rocks (Enger, work in progress).

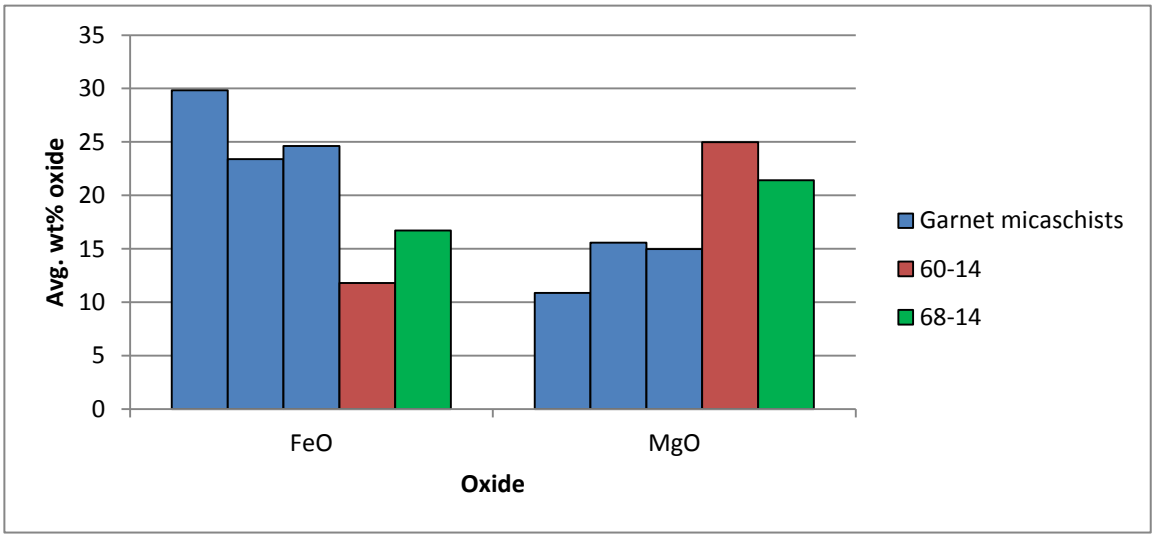

Fig. 8.2: FeO and MgO in chlorite in the three samples of garnet micaschist and blackwall altered schist at Vetle Raudberget (sample 60-18) and Raudberget (sample 68-14). Both blackwall schists show a clear decrease in FeO and an increase in MgO. The difference is bigger in the sample from Vetle Raudberget.

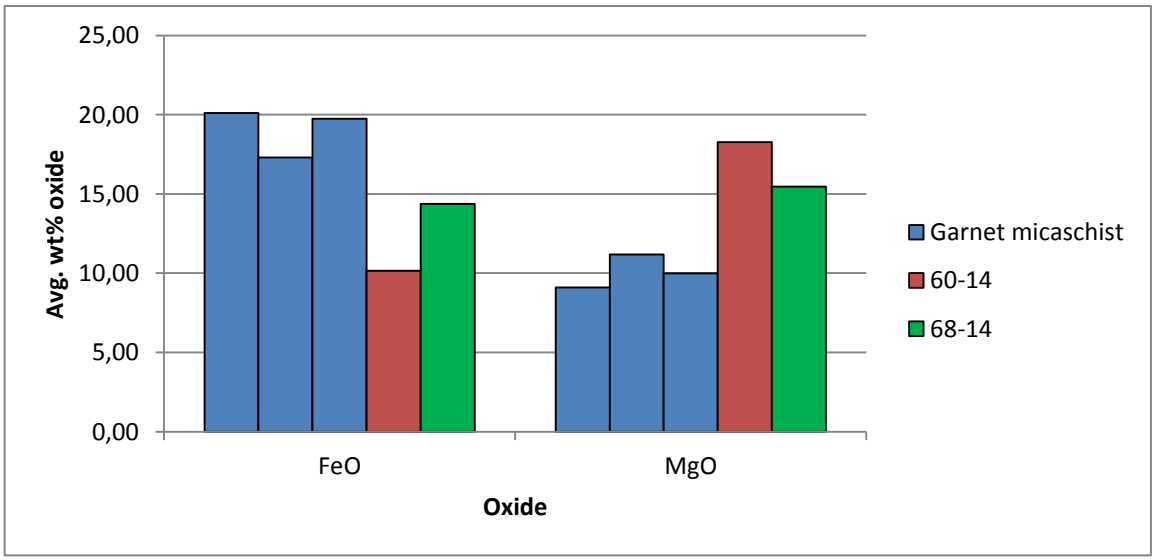

Fig 8.3: FeO and MgO in biotite in the three samples of garnet micaschist and blackwall altered schist at Vetle Raudberget (sample 60-18) and Raudberget (sample 68-14). Both blackwall schists show a clear decrease in FeO and an increase in MgO. The difference is bigger in the sample from Vetle Raudberget.

Figure 8.2 and 8.3 shows the average wt% of FeO and MgO in chlorites and biotite in three samples of garnet micaschist and the two blackwall schists based on EMP data. The garnet micaschists have a fairly stable FeO and MgO content in both biotite and chlorite, while the blackwall schists show a significantly higher concentration of MgO and a lower concentration of FeO. Other elements show a stable concentration so FeO is most likely been replaced by MgO in the minerals.

The increase of MgO in the micas most likely came from the ultramafic rocks that surround the schist (fig. 8.3). The removed FeO may have been included in magnetite crystals found in the serpentinite (see Enger, work in progress). Both of the micas shows the same trend in FeO and MgO concentration, where the FeO is lower than the other metapelite and the MgO concentration is higher. The sample taken at Vetle Raudberget (sample 60-14) shows a higher MgO and lower FeO concentration than the sample taken at Raudberget. This would suggest a higher degree of alteration at Vetle Raudberget. Vetle Raudberget does show a higher degree of serpentinization (Enger, work in progress), so it is possible that this have led to a higher degree of blackwall alteration.

8.2 Hyperextension

The mélange lies structurally between the Lower and Upper Bergsdalen nappes, below the Jotun and Lindås Nappes (see above). The unit is traceable continuously across the southern parts of Norway, from Bergen and more or less continuously to Otta. Further north there are no signs of mélange development (Nilsson and Roberts, 2014). Even though they disputed the hyperextension hypothesis for the areas north of Otta, they agreed with Andersen *et al.* (2012) for the areas from Bergen and towards Otta. The ultramafic bodies found further north is found together with gabbros, at a higher stratigrafic level than the mélange. These ultramafics are still interpreted as ophiolites (Nilsson and Roberts, 2014). The mélange unit has previously been largely overlooked, and the ultramafic bodies found in the unit have been given an ophiolitic origin (e.g. Qvale and Stigh, 1985; Sturt *et al.*, 1991), see above. The unit show strong Caledonian deformation and must therefore have been formed prior to the orogen, and then been thrust into the present day positioning during the collision.

Next to Vetle Raudberget there are found serpentine conglomerate, which means that the ultramafic bodies must have been exhumed to the surface prior to the orogeny in order to supply the basin with clasts now found in the conglomerate (Andersen *et al.*, 2012). Serpentine conglomerates are common in the Scandinavian Caledonides (Qvale and Stigh, 1985). The classical pseudostratigraphy of an ophiolite contains serpentinites, gabbros, sheeted dikes, pillow basalts and deep marine sediments (Dilek and Furnes, 2011). This makes an ophiolitic origin less likely because no pillow basalt, or sheeted dikes and little gabbro have been found in the mélange. This also means that with an ophiolitic origin, all the sheeted dikes, gabbro and pillow basalts must have been removed to expose the metaperidotites at the seafloor, without removal of the ultramafics, prior to the orogen. A hyperextended origin is therefore more likely than an ophiolitic. Hyperextension explains the different lithologies and their relations found in the study area. This could also explain the curse grained conglomerate found interlayered within the black-wall altered schists, which has an age similar to the Baltic basement Andersen *et al.* (2012). In a hyperextended situation the basin is situated close to the continent, and the basin can be supplied with sediments from the continent. The ultramafic bodies found in the mélange has undergone widespread alteration though serpentinization, talcification and formation of ophicarbonate (Enger, work in progress; Andersen *et al.*, 2012). This is typical of peridotites that has a origin of exhumation during hyperextension of passive continental margins (Bernoulli and Jenkyns, 2009).

One thing that would help considerably in the discussion of the origin of the mélange unit and the metaperidotites, is an age of formation. Since the unit shows strong Caledonian deformation it must have formed prior to the orogeny, and the basin was receiving sediments at 468±26Ma shown by zircons in samples taken at Kvilesteinsvatnet (Slama and Pedersen, 2015). There is however little else to limit the age of formation of the mélange at this point. If the mélange formed as a product of hyperextension of the border between Baltica and Laurentia, it most likely formed during the formation of the Iapetus Ocean. The continental break up leading to the formation of the Iapetus Ocean is marked by doleritic and doleritic-tholeiitic dyke swarms with an age span between ca. 542-610Ma (Nystuen *et*

al., 2008). If the mélange formed in the evolving Iapetus it may have an age close to the dyke swarms.

8.2.1 Comparisons between the study area and other localities in the mélange

Another part of the Caledonian mélange mapped in detail is in Bøverdalen (see Alsaif, 2015). As in the study area for this thesis, the lithologies consist of metaperidotites set in a matrix of metasediments. The metasediments is today found as meta-sandstone, garnet schist, mica schist and graphite schist. The ultramafic bodies in Bøverdalen are mostly found as serpentinites, with the addition to some local occurrences of soapstone and talc schist. No preserved peridotite is found (Alsaif, 2015). The serpentinites in Bøverdalen also show ophicarbonatization and breccia structures. High grade of alteration of the ultramafic bodies are also the case in Stølsheimen (Enger, work in progress). As in Stølsheimen, blackwall altered schists are only observable in the contact between the ultramafic rocks and the surrounding metasediments (Alsaif, 2015). Dated granitoid samples from Bøverdalen gives an age most likely linked to partial melting during the orogeny at ~420Ma (Alsaif, 2015), with the use of U-Pb data. This is similar to the age of the Caledonian overprint found by (Andersen *et al.*, 2012) to be 410±3,1Ma by use of U/Pb dating of titanite.

8.2.2 Iberian passive margin, a possible present day analogue?

The best studied present day hyperextended margin is the passive margin of the coast of Iberia. Fig. 8.4 shows a part of this present day hyperextended margin of the coast of Iberia. The figure is based on both seismic imaging and drill cores. The extension has split the continental crust into slivers with exhumed mantle between them. The figure shows that the subcontinental mantle has been exhumed to the surface through extension of the continental crust. This results in a basin where fragments of exhumed mantle and continental crust can mix with post rift sediments. If this is a possible model for the passive margin of Baltica, we would expect somewhat similar lithologies. In the figure there are abundant syn- and postrift sediments surrounding the exhumed subcontinental mantle. As explained above the metaperidotites in the Caledonian mélange is set in a matrix of metasediments and this is exactly what the figure show. This possible analogue can also explain the serpentine conglomerate that is present in the Caledonian mélange. With the

subcontinental mantle exhumed to the surface as it is in the figure, it is possible for the mantle rocks to break free from the main ultramafic body and end up as clasts in the sediments, before the entire system is covered by late sediments. Interlayered with the black wall altered schists is a course grained conglomerate with clasts dated to 1033±20Ma. These clasts are believed to have a continental origin (Andersen *et al.*, 2012). These clasts are too big to be transported great distances, so they are most likely found fairly close to their place of origin. This can also be explainable by the present day hyperextended margin shows in fig. 8.4. The exhumed subcontinental mantle is found close to the continental crust and continental ribbons separated from the continental crust by the extensional tectonics.

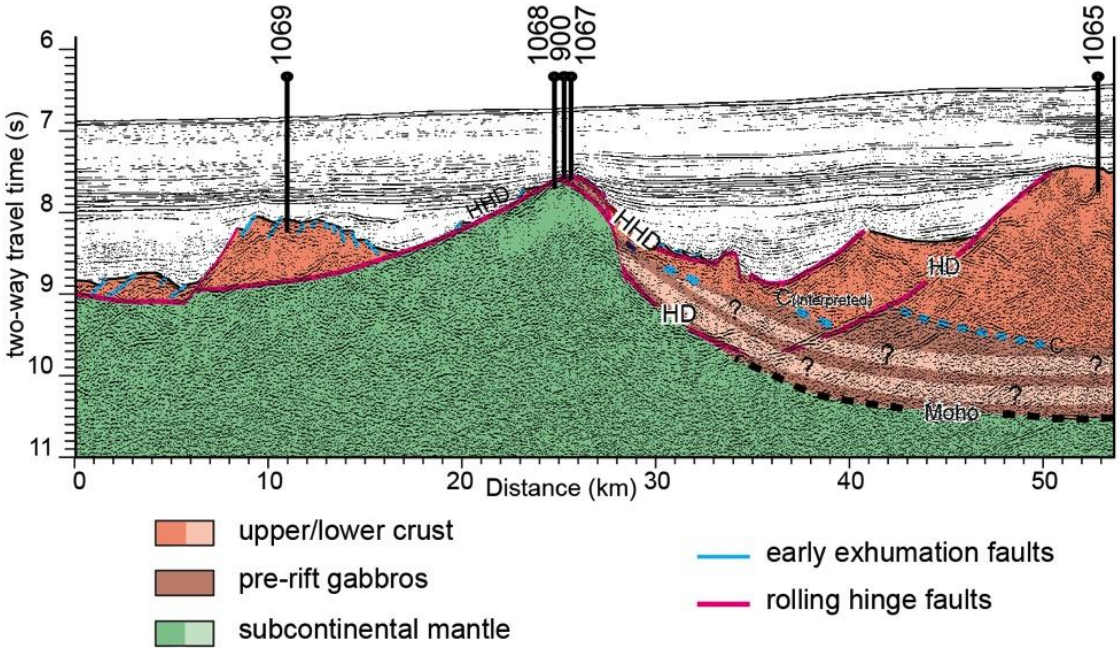

Fig. 8.4: Present day hyperextended margin of the coast of Iberia, with subcontinental mantle exhumed to the surface and then buried in post rift sediments. Modified after Manatschal (2004).

8.3 Paleotectonic implications due to the hyperextended margin

In the classical model of the Caledonian orogen, the Lower Bergsdalen Nappe is a part of the Lower Allochthon, and the Upper Bergsdalen and Jotun nappes are parts of the Middle Allochthon. All of these three nappes in the Middle Allochthon were believed to be attached to Baltica prior the orogeny (table 2.1). The presence of the mélange unit however, challenges this view. The most likely origin of the mélange is that it formed between Baltica and the nappes of the Middle Allochthon (fig.8.5). See explanation below. If this is the case the mélange would have separated Baltica with the Upper Bergsdalen, Lindås and Jotun nappes with a considerable distance.

This is supported by fossils found in the Vågå serpentine conglomerate (Bruton and Harper, 1981), belonging to the mélange unit. The Celtic fauna have a Mid-Ordovician age (470-464Ma) and supports an island arc outboard of Baltica, separated with a considerable distance (Fig 8.1).

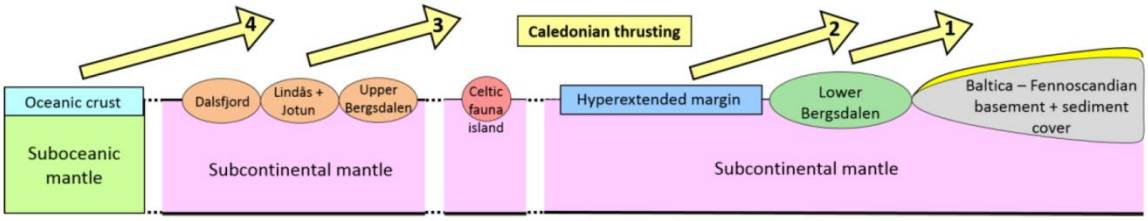

Fig. 8.5: Possible reconstruction of the Baltica margin prior to the Caledonian collision, with the hyperextended margin separating the Lower Bergsdalen Nappe with the Upper Bergsdalen, Lindås, Jotun and Dalsfjord nappes. These three nappes may have been microcontinents or arcs. The arrows show the thrusting and stacking of the nappes and the numbers show the sequence of stacking. Also note the island with the Celtic fauna. From Alsaif (2015).

This would imply that the crystalline nappes of Upper Bergsdalen, Lindås and Jotun nappes are (probably) microcontinents or continental ribbons separated from Baltica (Andersen *et al.*, 2012 and fig. 8.5). The pseudo-terrain reconstruction gives a possible explanation of the stacking of the Caledonian Nappes as it is found today, with the Lower Bergsdalen as the lowermost unit, the possibly hyperextended margin on top, followed by the other major Allochthonous units.

If both the Upper and Lower Bergsdalen nappes were attached to Baltica at the start of the orogeny, an alternative explanation is required. This can be done by out of sequence faulting or by wedging the mélange unit in between the nappes, as explained by Alsaif (2015). In an out of sequence scenario the Lower Bergsdalen nappe would be thrusted on top of the Baltic basement first. The hyperextended margin would then have to thrusted up and over the Upper Bergsdalen, Lindås and Dalsfjord nappes, placing the unit on top of the Lower Bergsdalen nappes. The Upper Bergsdalen, Lindås and Dalsfjord nappes would then be trusted on top of the mélange. In a wedging scenario the Lower and Upper Bergsdalen, Lindås and Dalsfjord nappes would be thrusted on top of the Baltic basement first, followed by the hyperextended margin. The mélange would then have to be wedged in between the Bergsdalen nappes. Both these scenarios are unlikely to explain the positioning of the mélange. In an out of sequence faulting scenario the thrusting of the hyperextended margin would most likely stopped on top of the Dalsfjord, Lindås and Upper Bergsdalen nappes. In a wedging scenario the hyperextended margin consisting of serpentinites and metasediments would have to be wedged in between two major units of crystalline rocks. This makes the scenario in fig. 8.5, with the hyperextended margin separating the Lower Bergsdalen nappe with the Dalsfjord, Lindås and Upper Bergsdalen nappes the most likely of the three.

9. Conclusion and way forward

The mélange unit in between the Lower and Upper Bergsdalen nappes have largely been overlooked in previous tectonic models for the Caledonides. These two nappes have traditionally been assigned to the Lower and Middle Allochthon, both with Baltic origin. The mélange shows that the Dalsfjord, Lindås, Jotun and the Upper Bergsdalen nappes, most likely was not attached to Baltica at the start of the Caledonian orogen, but may have originated as microcontinents separated from Baltica with a considerable distance. The new interpretation of the formation mélange is that the unit is believed to be of a hyperextended origin.

This thesis has together with Enger (work in progress) studied the metaperidotites and surrounding metasediments found in the Stølsheimen area. This thesis has largely focused on the structural and metamorphic history of the metasediments, while Enger (work in progress) have studied the ultramafic bodies in detail. The dominating kinematic indicators in the Raudberget area give an apparent top to the NW shear direction, giving a deformation age corresponding to the Caledonian extensional. Some remaining D1 age (Caledonian thrusting) deformation has also been found in the area. Peak metamorphic conditions have been limited to 515-525^{o}C and 7100-7450 bars by use of the *Theriak-Domino* program suite, achieved during prograde metamorphism. The metasediments show a largely overprinted foliation during D2 deformation, but remnants of the older foliation is still visible in thin-sections.

In order to conclude on the hyperextension hypothesis, more work in needed. More detailed mapping of the mélange along the Caledonides together with structural restoration can give a clearer image of the basin prior the Caledonian orogeny. A more precise age of formation of the unit would also help in determining the origin of the mélange.

10. References

Aarflot, G. (1984). En geologisk og mineralogisk undersøkelse an talkforekomster i Raudberg-feltet i Stølsheimen. Trondheim, NTH. **Master thesis:** 141.

Alsaif, M. T. (2015). The lithostratigraphy and history of the Caledonian mélange basin rocks below the Jotun Nappe in Bøverdalen, South Central Norway. Oslo, University of Oslo. **Master thesis:** 107.

Andersen, T. B. (1998). "Extensional tectonics in the Caledonides of southern Norway, an overview." Tectonophysics **285**(3): 333-351.

Andersen, T. B., F. Corfu, L. Labrousse and P.-T. Osmundsen (2012). "Evidence for hyperextension along the pre-Caledonian margin of Baltica." Journal of the Geological Society **169**(5): 601-612.

Andersen, T. B., B. Jamtveit, J. Dewey and E. Swensson (1991). "Subduction and eduction of continental crust: major mechanism during continent-continent collision and orogenic extensional collapse, a model based on the south Caledonides." Terra Nova **3**: 303-310.

Austrheim, H. (1987). "Eclogitization of lower crustal granulites by fluid migration through shear zones." Earth and Planetary Science Letters **81**(2): 221-232.

Austrheim, H. and T. Prestvik (2008). "Rodingitization and hydration of the oceanic lithosphere as developed in the Leka ophiolite, north–central Norway." Lithos **104**(1): 177-198.

Bakke, S. (1986). "Talk i Raudbergfeltet, Vik i Sogn." Norges geologiske undersøkelse Rapport 86.018.

Banno, S. and S. Chii (1978). "A model to explain the Mn enrichment in the rim of zoned garnet." Geochemical Journal **12**(4): 253-257.

Beinlich, A., H. Austrheim, J. Glodny, M. Erambert and T. B. Andersen (2010). "CO 2 sequestration and extreme Mg depletion in serpentinized peridotite clasts from the Devonian Solund basin, SW-Norway." Geochimica et Cosmochimica Acta **74**(24): 6935-6964.

Bernoulli, D. and H. C. Jenkyns (2009). "Ancient oceans and continental margins of the Alpine-Mediterranean Tethys: Deciphering clues from Mesozoic pelagic sediments and ophiolites." Sedimentology **56**(1): 149-190.

Bingen, B., Ø. Nordgulen and G. Viola (2008). "A four-phase model for the Sveconorwegian orogeny, SW Scandinavia." Norsk Geologisk Tidsskrift **88**(1): 43.

Brady, J. (2015). "Mineral Formulae Recalulation." Retrieved 02.10, 2015, from www.serc.carleton.edu/research_education/equilibria/mineralformulaerecalculation.html.

Brouwer, P. (2003). "Theory of XRF." Panalytical, Netherlands.

Brun, J. and M. Beslier (1996). "Mantle exhumation at passive margins." Earth and Planetary Science Letters **142**(1): 161-173.

Bruton, D. L. and D. A. Harper (1981). "Brachiopods and trilobites of the early Ordovician serpentine Otta Conglomerate, south central Norway." Norsk Geologisk Tidsskrift **61**(2): 153-181.

Bryhni, I. and P. Andréasson (1985). "Metamorphism in the Scandinavian Caledonides." Gee, DG, Sturt, BA,(Eds.), The Caledonide Orogen-Scandinavia and Related Areas. Wiley & Sons Ltd, Chichester: 763-782.

Bucher, K. and R. Grapes (2011). Petrogenesis of Metamorphic Rocks. New York, USA, Springer.

Cochran, J. and G. Karner (2007). "Constraints on the deformation and rupturing of continental lithosphere of the Red Sea: the transition from rifting to drifting." Geological Society, London, Special Publications **282**(1): 265-289.

Contrucci, I., L. Matias, M. Moulin, L. Géli, F. Klingelhofer, H. Nouzé, D. Aslanian, J.-L. Olivet, J.-P. Réhault and J.-C. Sibuet (2004). "Deep structure of the West African continental margin (Congo, Zaïre, Angola), between 5 S and 8 S, from reflection/refraction seismics and gravity data." Geophysical Journal International **158**(2): 529-553.

Corfu, F., T. Andersen and D. Gasser (2014). "The Scandinavian Caledonides: main features, conceptual advances and critical questions." Geological Society, London, Special Publications **390**(1): 9-43.

Corfu, F. and M. Heim (2014). "Geology and U–Pb geochronology of the Espedalen Complex, southern Norway, and its position in the Caledonian nappe systems." Geological Society, London, Special Publications **390**(1): 223-239.

Cowie, P. A., J. R. Underhill, M. D. Behn, J. Lin and C. E. Gill (2005). "Spatio-temporal evolution of strain accumulation derived from multi-scale observations of Late Jurassic rifting in the northern North Sea: A critical test of models for lithospheric extension." Earth and Planetary Science Letters **234**(3): 401-419.

de Capitani, C. and T. H. Brown (1987). "The computation of chemical equilibrium in complex systems containing non-ideal solutions." Geochimica et Cosmochimica Acta **51**(10): 2639-2652.

de Capitani, C. and K. Petrakakis (2009). THERIAK-DOMINO user's guide. Theriak-Domino documentation, Version 01.08.09.

de Capitani, C. and K. Petrakakis (2010). "The computation of equilibrium assemblage diagrams with Theriak/Domino software." American Mineralogist **95**(7): 1006-1016.

Dilek, Y. and H. Furnes (2011). "Ophiolite genesis and global tectonics: geochemical and tectonic fingerprinting of ancient oceanic lithosphere." Geological Society of America Bulletin **123**(3-4): 387-411.

Doré, T. and E. Lundin (2015). "RESEARCH FOCUS: Hyperextended continental margins—Knowns and unknowns." Geology **43**(1): 95-96.

Dunning, G. and R. Pedersen (1988). "U/Pb ages of ophiolites and arc-related plutons of the Norwegian Caledonides: implications for the development of Iapetus." Contributions to Mineralogy and Petrology **98**(1): 13-23.

Enger, A. (work in progress). "Solitary mantle peridotite bodies in Stølsheimen, Central South Norway (provisonal title)."

Fauconnier, J., L. Labrousse, T. B. Andersen, O. Beyssac, S. Duprat-Oualid and P. Yamato (2014). "Thermal structure of a major crustal shear zone, the basal thrust in the Scandinavian Caledonides." Earth and Planetary Science Letters **385**: 162-171.

Fossen, H. (1992). Devonian extensional deformation in the Caledonia orogen, Southern Norway. Minnesote, USA, University of Minnesota. **PhD thesis:** 169.

Fossen, H. (1993a). "Linear fabrics in the Bergsdalen Nappes, southwest Norway: implications for deformation history and fold development." Norsk Geologisk Tidsskrift **73**(2): 95-108.

Fossen, H. (1993b). "Structural evolution of the Bergsdalen Nappes, southwest Norway." Norges geologiske undersøkelse Bulletin **424**: 23-50.

Hacker, B. R., T. B. Andersen, S. Johnston, A. R. Kylander-Clark, E. M. Peterman, E. O. Walsh and D. Young (2010). "High-temperature deformation during continental-margin subduction & exhumation: The ultrahigh-pressure Western Gneiss Region of Norway." Tectonophysics **480**(1): 149-171.

Harper, D. A., A. W. Owen and D. L. Bruton (2009). "Ordovician life around the Celtic fringes: diversifications, extinctions and migrations of brachiopod and trilobite faunas at middle latitudes." Geological Society, London, Special Publications **325**(1): 157-170.

Hollister, L. S. (1969). "Contact metamorphism in the Kwoiek area of British Columbia: an end member of the metamorphic process." Geological Society of America Bulletin **80**(12): 2465-2494.

Jakob, J., M. T. Alsaif, F. Corfu and T. B. Andersen (in prep (b)). "New U-Pb ID-TIMS age constraints on the evolution of a tectonic melange in southwestern Norway: Indications for magmatic activity outboard the Caledonian margin of Baltica in the Early Ordovician (Provisional title)."

Jakob, J., T. B. Andersen and O. Beyssac (in prep (a)). "On the tectonothermal evolution of a melange zone in southwestern Norway: The Wilson Cycle from hyperextension to contnent-continent collision (Provisional title)."

Karlsen, T. (1990). "Mineralogisk undersøkelse av talk-karbonat-malm, Raudberg-feltet, Vik i sogn." Norges geologiske undersøkelse Report 90.086.

Konrad-Schmolke, M., M. R. Handy, J. Babist and P. J. O'Brien (2005). "Thermodynamic modelling of diffusion-controlled garnet growth." Contributions to Mineralogy and Petrology **149**(2): 181-195.

Kretz, R. (1973). "Kinetics of the crystallization of garnet at two localities near Yellowknife." The Canadian Mineralogist **12**(1): 1-20.

Kvale, A. (1946). Petrologic and structural studies in the Bergsdalen Quadrangle western Norway, part 1, Bergen Museums Årbok 1946-47, Naturvit. rekke 1.

Labrousse, L., G. Hetényi, H. Raimbourg, L. Jolivet and T. B. Andersen (2010). "Initiation of crustal-scale thrusts triggered by metamorphic reactions at depth: Insights from a comparison between the Himalayas and Scandinavian Caledonides." Tectonics **29**(5).

Le Pichon, X. and J.-C. Sibuet (1981). "Passive margins: a model of formation." J. geophys. Res **86**(B5): 3708-3720.

López-Carmona, A. and E. Segovia-Diaz (2015). "Mineralformula recalculation." Retrieved 01.05, 2015, from www.serc.carleton.edu/research_education/equilibria/mineralformulaerecalculation.html.

Lundin, E. R. and A. G. Doré (2011). "Hyperextension, serpentinization, and weakening: A new paradigm for rifted margin compressional deformation." Geology **39**(4): 347-350.

Lundmark, A. and F. Corfu (2008). "Late-orogenic Sveconorwegian massif anorthosite in the Jotun Nappe Complex, SW Norway, and causes of repeated AMCG magmatism along the Baltoscandian margin." Contributions to Mineralogy and Petrology **155**(2): 147-163.

Lundmark, A., F. Corfu, S. Spürgin and R. Selbekk (2007). "Proterozoic evolution and provenance of the high-grade Jotun Nappe Complex, SW Norway: U–Pb geochronology." Precambrian Research **159**(3): 133-154.

Manatschal, G. (2004). "New models for evolution of magma-poor rifted margins based on a review of data and concepts from West Iberia and the Alps." International Journal of Earth Sciences **93**(3): 432-466.

Minshull, T., S. Dean, R. White and R. Whitmarsh (2001). "Anomalous melt production after continental break-up in the southern Iberia Abyssal Plain." Geological Society, London, Special Publications **187**(1): 537-550.

Müller, G. and A. Schneider (1971). "Chemistry and genesis of garnets in metamorphic rocks." Contributions to Mineralogy and Petrology **31**(3): 178-200.

Nesse, W. D. (2013). Introduction to optical mineralogy. New York, USA, Oxford University Press**:** 203-204.

Neuman, R. B. (1984). "Geology and paleobiology of islands in the Ordovician Iapetus Ocean: Review and implications." Geological Society of America Bulletin **95**(10): 1188-1201.

Nilsson, L.-P. and D. Roberts (2014). "A trail of ophiolitic debris and its detritus along the Trøndelag-Jämtland border: correlations and palaeogeographical implications." Norges geologiske undersøkelse Bulletin **453**: 29-41.

Nystuen, J. P., A. Andresen, R. A. Kumpulainen and A. Siedlecka (2008). "Neoproterozoic basin evolution in Fennoscandia, East Greenland and Svalbard." Episodes **31**(1): 35-43.

Oftedahl, C. (1969). "Caledonian pyroclastic (?) serpentinite in central Norway." Geological Society of America Memoirs **115**: 305-316.

Osmundsen, P. and J. Ebbing (2008). "Styles of extension offshore mid-Norway and implications for mechanisms of crustal thinning at passive margins." Tectonics **27**(6).

Pérez-Gussinyé, M. (2013). "A tectonic model for hyperextension at magma-poor rifted margins: an example from the West Iberia–Newfoundland conjugate margins." Geological Society, London, Special Publications **369**(1): 403-427.

Pérez-Gussinyé, M., C. Ranero, T. J. Reston and D. Sawyer (2003). "Mechanisms of extension at nonvolcanic margins: Evidence from the Galicia interior basin, west of Iberia." Journal of Geophysical Research: Solid Earth (1978–2012) **108**(B5).

Perez—Gussinyé, M. and T. J. Reston (2001). "Rheological evolution during extension at nonvolcanic rifted margins: onset of serpentinisation and development of detachments leading to continental break-up." Journal of Geophysical Research **106**(B3): 3961-3975.

Péron-Pinvidic, G. and G. Manatschal (2009). "The final rifting evolution at deep magma-poor passive margins from Iberia-Newfoundland: a new point of view." International Journal of Earth Sciences **98**(7): 1581-1597.

Peron-Pinvidic, G., G. Manatschal and P. T. Osmundsen (2013). "Structural comparison of archetypal Atlantic rifted margins: a review of observations and concepts." Marine and Petroleum Geology **43**: 21-47.

Preston, J. (2015). "Mineralogical spreasheet." Retrieved 01.05, 2015, from http://www.gabbrosoft.org/spreadsheets.html.

Qvale, H. and J. Stigh (1985). Ultramafic rocks in the Scandinavian Caledonides. The Caledonide Orogen-Scandinavia and Related Areas, part 2. D. G. Gee and B. A. Start. Great Britain, Wiley-Interscience Publication**:** 693-716.

Ranero, C. R. and M. Pérez-Gussinyé (2010). "Sequential faulting explains the asymmetry and extension discrepancy of conjugate margins." Nature **468**(7321): 294-299.

Roberts, D. (2003). "The Scandinavian Caledonides: event chronology, palaeogeographic settings and likely modern analogues." Tectonophysics **365**(1): 283-299.

Roffeis, C. and F. Corfu (2014). "Caledonian nappes of southern Norway and their correlation with Sveconorwegian basement domains." Geological Society, London, Special Publications **390**(1): 193-221.

Roffeis, C., F. Corfu and H. Austrheim (2012). "Evidence for a Caledonian amphibolite to eclogite facies pressure gradient in the Middle Allochthon Lindås Nappe, SW-Norway." Contributions to Mineralogy and Petrology **164**(1): 81-99.

Roffeis, C., F. Corfu and R. Gabrielsen (2013). "A Sveconorwegian terrane boundary in the Caledonian Hardanger–Ryfylke Nappe Complex: The lost link between Telemarkia and the Western Gneiss Region?" Precambrian Research **228**: 20-35.

Sandstad, J. S., O. Olesen, B. Larsen, B. Sundvoll, D. M. Ramsay, B. A. Sturt and R. Bøe (1993). "The Conglomerates of the Sel Group, Otta-Vågå Area, Central Norway, an Example of Terrane-linking Succession." Norges geologiske undersøkelse , Bulletin **425**: 1-23.

Sanford, R. F. (1982). "Growth of ultramafic reaction zones in greenschist to amphibolite facies metamorphism." American Journal of Science **282**(5): 543-616.

Schärer, U. (1980). "U-Pb and Rb-Sr dating of a polymetamorphic nappe terrain: the Caledonian Jotun Nappe, southern Norway." Earth and Planetary Science Letters **49**(2): 205-218.

Slama, J. and R. B. Pedersen (2015). "Zircon provenance of SW Caledonian phyllites reveals a distant Timanian sediment source." Journal of the Geological Society: 2014-2143.

Smithson, S. B., I. B. Ramberg and G. Grönlie (1974). "Gravity interpretation of the Jotun Nappe of the Norwegian Caledonides." Tectonophysics **22**(3): 205-222.

Strand, T. (1970). "On the mode of formation of the Otta serpentinite conglomerate." Norwegian Journal of Geology **50**: 393-395.

Sturt, B. A. and D. M. Ramsay (1999). "Early Ordovician terrane-linkages between oceanic and continental terranes in the central Scandinavian Caledonicles." Terra Nova-Oxford **11**(2-3): 79-85.

Sturt, B. A., D. M. Ramsay and R. B. Neuman (1991). "The Otta Conglomerate, the Vågåmo Ophiolite - further indications of Early Orodovician Orogenesis in the Scandinavian Caledonides." Norsk Geologisk Tidsskrift **71**: 107-115.

Sutra, E. and G. Manatschal (2012). "How does the continental crust thin in a hyperextended rifted margin? Insights from the Iberia margin." Geology **40**(2): 139-142.

Terry, M. P., P. Robinson, A. Hamilton and M. J. Jercinovic (2000). "Monazite geochronology of UHP and HP metamorphism, deformation, and exhumation, Nordøyane, Western Gneiss Region, Norway." American Mineralogist **85**(11-12): 1651-1664.

Tirone, M. and J. Ganguly (2010). "Garnet compositions as recorders of P–T–t history of metamorphic rocks." Gondwana Research **18**(1): 138-146.

Torstensen, O. (1981). En mineralogisk og magnetometrisk undersøkelse av talkforekomster i Vik i Sogn. Trondheim, NTH. **Master thesis:** 101.

van Roermund, H. (2009). "Mantle-wedge garnet peridotites from the northernmost ultra-high pressure domain of the Western Gneiss Region, SW Norway." European Journal of Mineralogy **21**(6): 1085-1096.

Van Roermund, H. and M. Drury (1998). "An ultra-deep (200 km) orogenic peridotite body in Western Norway." Eos **79**: F971.

Vernon, R. (1978). "Porphyroblast-matrix microstructural relationships in deformed metamorphic rocks." Geologische Rundschau **67**(1): 288-305.

Wernicke, B. (1985). "Uniform-sense normal simple shear of the continental lithosphere." Canadian Journal of Earth Sciences **22**(1): 108-125.

Winter, J. D. (2014). Principles of igneous and metamorphic petrology. New York, USA, Pearson Prentice Hall.

Woodsworth, G. (1977). "Homogenization of zoned garnets from pelitic schists." Canadian Mineralogist **15**: 230-242.

Zwart, H. (1962). "On the determination of polymetamorphic mineral associations, and its application to the Bosost area (Central Pyrenees)." Geologische Rundschau **52**(1): 38-65.

11. Appendix 1 – geological map

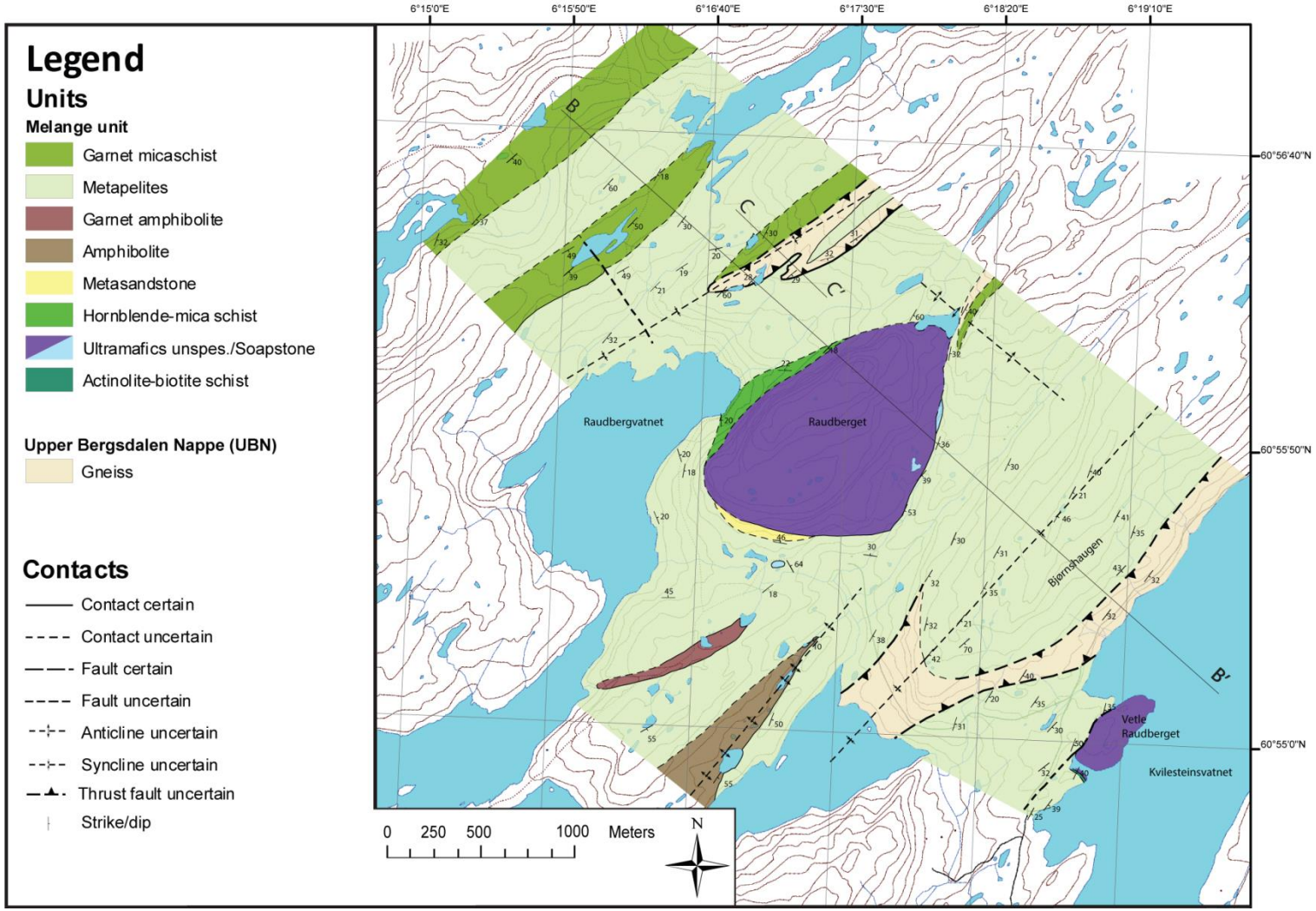

12.Appendix 2 – Sample map

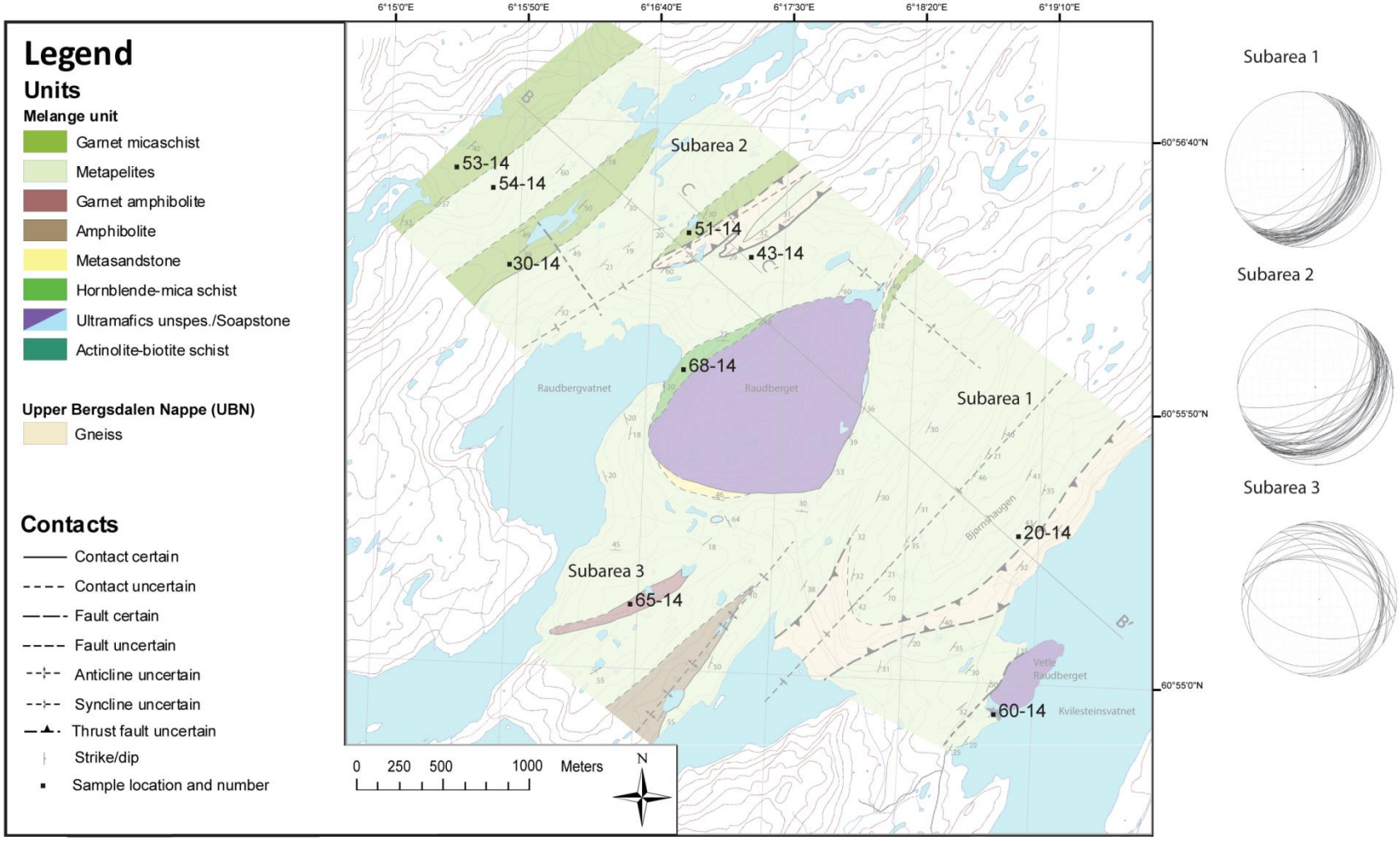

13.Appendix 3 – Sample overview

Sample number	Lithology	EMP	XRF
20-14	Metapelite		X
30-14	Garnet micaschist	X	X
43-14	Metapelite	X	
51-14	Garnet micaschist	X	X
53-14	Garnet micaschist	X	X
54-14	Metapelite		X
60-14	Actinolite-Biotite schist (Blackwall alteration)	X	
65-14	Garnet amphibolite	X	X
68-14	Hornblende micaschist (Blackwall alteration)	X	

14.Appendix 4 - XRF data

Sample	20-14		30-14		51-14		53-14		54-14		65-14	
Lithology	Metapelite		Garnet micaschist		Garnet micaschist		Garnet micaschist		Metapelite		Garnet amphibolite	
Element	Wt%	Wt% w/LOI	Wt%	Wt% w/LOI	Wt%	Wt% w/LOI	Wt%	Wt% w/LOI	Wt%	Wt% w/LOI	Wt%	Wt% w/LOI
SiO_2	56,67	54,87	50,79	49,80	44,24	42,04	56,24	55,39	67,08	65,21	49,83	49,39
TiO_2	1,17	1,14	1,28	1,25	1,60	1,52	0,95	0,94	0,74	0,72	1,09	1,08
Al_2O_3	18,06	17,48	24,67	24,18	28,88	27,44	21,93	21,60	15,76	15,32	14,00	13,88
Fe_2O_3	8,25	7,99	9,04	8,86	11,44	10,87	10,94	10,77	6,59	6,41	14,22	14,09
Mn_3O_4	0,06	0,06	0,40	0,39	0,11	0,10	1,87	1,84	0,11	0,10	0,24	0,23
MgO	5,88	5,69	2,65	2,60	4,89	4,65	1,53	1,50	2,79	2,71	7,68	7,61
CaO	2,41	2,33	2,45	2,40	0,73	0,69	1,22	1,20	1,68	1,63	10,46	10,37
Na_2O	3,43	3,32	3,44	3,37	0,77	0,73	1,77	1,75	1,01	0,99	2,05	2,03
K_2O	3,77	3,65	4,80	4,71	7,22	6,86	3,67	3,62	3,73	3,63	0,27	0,27
P_2O_5	0,02	0,02	0,22	0,22	0,19	0,18	0,13	0,12	0,16	0,15	0,08	0,08
V_2O_5	0,03	0,02	0,05	0,05	0,05	0,05	0,03	0,02	0,02	0,02	0,07	0,07
Cr_2O_3	0,04	0,04	0,03	0,03	0,03	0,03	0,03	0,03	0,02	0,02	0,02	0,02
SrO	0,01	0,01	0,04	0,04	0,01	0,01	0,02	0,02	0,01	0,01	0,00	0,00
ZrO_2	0,03	0,03	0,04	0,04	0,05	0,05	0,02	0,02	0,03	0,03	0,00	0,00
BaO	0,05	0,04	0,12	0,12	0,13	0,12	0,09	0,09	0,06	0,06	0,00	0,00
NiO	0,01	0,01	0,01	0,01	0,01	0,01	0,01	0,00	0,00	0,00	0,01	0,00
ZnO	0,01	0,01	0,01	0,01	0,02	0,02	0,01	0,01	0,01	0,01	0,01	0,01
PbO	0,01	0,01	0,01	0,01	0,01	0,01	0,01	0,01	0,01	0,01	0,01	0,01
LOI	--	3,17	--	1,96	--	5,00	--	1,52	--	2,78	--	0,87
Total	**99,91**	**99,91**	**100,05**	**100,05**	**100,37**	**100,37**	**100,46**	**100,46**	**99,82**	**99,82**	**100,04**	**100,04**

15. Appendix 5 – EMP data

15.1 Sample 30-14

Info	Element profil fig. 5.16									Element profile 1 table 7.2							Element profile 2 table 7.2			
Data pt	1/1	2/1	3/1	4/1	5/1	6/1	7/1	8/1	9/1	38/1	39/1	40/1	41/1	42/1	43/1	44/1	49/1	50/1	51/1	52/1
Min	Grt	Grt	Grt	Grt	Grt	Grt	Grt	Grt	Grt	Grt	Grt	Grt	Grt	Grt	Grt	Grt	Grt	Grt	Grt	Grt
SiO2	36,73	37,04	36,43	36,38	36,48	36,49	36,86	37,15	37,36	37,08	36,80	37,04	37,11	36,83	37,06	37,20	37,58	37,22	36,46	37,03
Na2O	0,02	-0,02	0,01	0,04	0,01	0,02	0,01	0,01	-0,04	0,06	0,00	0,04	0,00	-0,01	0,00	0,01	-0,02	0,03	0,10	-0,01
Al2O3	20,66	20,80	20,82	20,66	20,55	20,44	20,57	20,90	21,10	20,89	20,91	20,84	20,63	20,68	20,65	20,98	20,98	21,01	20,66	20,71
K2O	0,01	0,00	0,01	0,03	-0,01	-0,01	0,00	-0,01	0,01	0,03	-0,01	-0,01	-0,01	0,00	-0,01	0,01	0,00	0,00	0,13	0,01
CaO	6,65	6,08	6,10	6,52	6,99	6,85	7,30	8,17	9,29	7,02	6,81	6,64	7,11	6,90	6,76	6,92	7,91	7,03	6,98	6,82
TiO2	0,00	0,09	0,12	0,14	0,12	0,12	0,12	0,07	0,06	0,06	0,04	0,06	0,15	0,15	0,09	0,09	0,04	0,10	0,08	0,04
FeO	32,38	27,50	25,89	25,44	26,05	28,05	29,27	30,86	30,08	31,68	31,48	31,62	31,55	31,61	31,67	31,76	31,20	31,65	31,95	33,39
MnO	2,28	8,54	9,77	10,14	9,21	6,26	4,54	1,89	1,13	2,12	2,85	2,77	2,56	2,13	2,42	2,17	1,18	2,19	1,93	0,74
MgO	1,10	0,73	0,70	0,59	0,64	0,75	0,89	1,18	1,48	1,00	0,98	0,96	0,98	1,02	1,01	1,06	1,20	1,02	1,00	1,20
Cr2O3	0,01	0,03	-0,01	-0,02	-0,04	0,06	-0,04	0,01	0,00	0,02	0,03	0,07	-0,01	0,05	0,04	0,01	0,01	0,03	0,03	0,04
Total	**99,85**	**100,78**	**99,83**	**99,92**	**100,01**	**99,04**	**99,52**	**100,24**	**100,46**	**99,97**	**99,90**	**100,02**	**100,08**	**99,36**	**99,68**	**100,20**	**100,08**	**100,28**	**99,31**	**99,97**

Data pt	10/ 1 .	11 / 1 .	13 / 1 .	18 / 1 .	20 / 1 .	25 / 1 .	28 / 1 .	33 / 1 .	12 / 1 .	15 / 1 .	17 / 1 .	21 / 1 .	23 / 1 .	24 / 1 .	30 / 1 .
Min	Chl	Chl	Chl	Chl	Chl	Chl	Chl	Chl	Afs	Bt	Bt	Bt	Bt	Bt	Bt
SiO2	23,90	22,64	21,81	24,87	24,96	25,02	25,71	24,53	61,54	35,65	36,24	35,88	36,25	36,73	35,84
Na2O	-0,01	0,02	0,01	0,03	-0,02	-0,03	0,01	-0,01	0,23	0,07	0,03	0,05	0,11	0,08	0,06
Al2O3	21,79	20,55	20,04	21,12	21,50	21,31	20,76	20,62	19,44	17,91	18,09	18,25	17,74	17,72	17,13
K2O	0,00	-0,01	0,00	0,06	0,01	0,02	0,61	0,01	15,13	8,75	9,48	9,27	9,16	9,16	9,48
CaO	0,05	0,04	0,08	0,09	0,01	0,00	-0,02	0,06	0,08	0,32	0,00	0,00	-0,02	-0,04	-0,02
TiO2	0,08	0,05	0,00	0,08	0,10	0,11	0,31	0,08	-0,03	1,74	1,33	0,66	1,95	1,94	1,95
FeO	30,30	38,68	41,56	26,19	26,52	24,79	25,18	25,45	0,79	20,10	20,13	21,06	19,72	19,45	20,09
MnO	0,52	1,02	1,27	0,34	0,35	0,30	0,35	0,34	0,05	0,21	0,28	0,24	0,19	0,19	0,17
MgO	10,91	4,29	1,76	13,37	13,73	14,40	13,75	14,82	0,00	8,87	8,99	8,99	9,47	9,61	9,02
Cr2O3	0,03	-0,02	-0,02	0,05	0,01	0,03	0,01	0,00	-0,01	0,09	0,00	-0,02	0,06	0,08	0,04
Total	**87,57**	**87,27**	**86,51**	**86,19**	**87,16**	**85,95**	**86,67**	**85,88**	**97,21**	**93,71**	**94,56**	**94,38**	**94,64**	**94,91**	**93,75**
Data pt	32 / 1.	34 / 1.	46 / 1.	48 / 1.	16 / 1 .	26 / 1 .	27 / 1 .	31 / 1 .	35 / 1 .	22 / 1 .	29 / 1 .	36 / 1 .	14 / 1 .	19 / 1 .	47 / 1 .
Min	Bt	Bt	Bt	Bt	Pl	Pl	Pl	Pl	Pl	Pl	Cal	Ms	Ms	Ms	Ms
SiO2	34,54	33,17	35,49	36,47	63,07	62,15	63,36	62,266	57,75	68,84	0,01	43,52	46,17	47,04	46,53
Na2O	0,04	0,07	0,07	0,09	9,1667	8,96	9,30	9,136	8,66	12,00	0	0,52	0,67	0,578	0,60
Al2O3	17,40	16,78	18,04	17,63	23,50	23,54	23,75	23,47	22,55	19,73	-0,01	31,71	35,37	34,32	32,97
K2O	9,69	9,58	8,88	8,51	0,11	0,12	0,09	0,10	0,13	0,08	-0,01	10,84	10,09	9,85	10,24
CaO	-0,05	-0,03	0,08	0,30	5,16	5,29	4,69	4,99	5,64	0,14	55,31	-0,07	0	-0,03	-0,03
TiO2	1,99	1,85	1,87	1,85	0,02	-0,00	0,00	0,01	0,02	-0,02	-0,02	0,84	0,3565	0,60	0,61
FeO	19,45	20,40	20,76	19,80	0,31	0,07	0,22	0,17	0,48	0,08	0,089	1,46	2,0544	1,94	1,83
MnO	0,17	0,20	0,24	0,19	-0,03	0,00	0,02	0,03	-0,03	-0,01	0,09	0,01	0,02	0,06	-0,00
MgO	8,90	9,23	8,53	9,36	-0,02	-0,0057	-0,00	-0,00	0,0058	0,016	-0,0938	1,1128	1,3462	1,4384	1,43
Cr2O3	0,01	0,02	0,02	0,07	-0,02	-0,04	-0,02	-0,01	0,01	0,00	0,03	0,07	0,09	0,06	0,04
Total	**92,16**	**91,27**	**93,98**	**94,27**	**101,27**	**100,09**	**101,39**	**100,17**	**95,20**	**100,85**	**55,40**	**90,01**	**96,17**	**95,86**	**94,21**

15.2 Sample 43-14

Data pt	114/1.	115/1.	116/1.	122/1.	123/1.	127/1.	137/1.	139/1.	160/1.	161/1.	143/1.	156/1.	124/1.	154/1.	155/1.
Min	Bt	Bt	Bt	Bt	Bt	Bt	Bt	Bt	Bt	Bt	Tnt	Tnt	Pl	Pl	Pl
SiO2	36,90	36,35	36,89	37,55	36,76	36,35	36,25	36,49	36,60	36,47	30,39	30,36	62,01	62,50	63,49
Na2O	0,10	0,10	0,11	0,11	0,05	0,10	0,13	0,11	0,10	0,07	0,05	0,00	9,02	9,21	9,24
Al2O3	16,94	16,91	17,04	17,48	17,08	16,87	16,16	17,09	16,91	16,71	0,98	1,22	23,17	23,19	23,12
K2O	9,59	9,62	9,59	9,54	9,47	9,49	9,27	9,42	9,39	9,56	0,05	-0,02	0,10	0,07	0,07
CaO	0,03	-0,05	-0,01	-0,02	-0,05	-0,03	0,41	0,01	0,02	-0,06	28,67	28,91	4,98	4,87	4,58
TiO2	1,71	1,86	1,98	1,59	1,85	1,85	1,85	1,76	1,67	1,75	39,24	39,01	0,01	0,00	0,05
FeO	17,08	17,36	17,24	16,70	16,93	17,24	16,66	17,37	17,19	17,75	0,47	0,51	0,21	0,36	0,27
MnO	0,15	0,11	0,12	0,09	0,10	0,08	0,10	0,14	0,08	0,10	0,10	0,03	0,00	0,00	0,00
MgO	12,49	12,11	11,74	12,71	12,07	12,20	12,12	11,93	12,61	12,14	-0,06	-0,03	0,00	-0,01	-0,01
Cr2O3	0,01	0,06	0,07	0,09	0,04	0,09	0,15	0,05	0,05	0,03	0,02	0,02	0,02	-0,03	0,01
Total	**95,00**	**94,42**	**94,79**	**95,85**	**94,30**	**94,23**	**93,10**	**94,37**	**94,63**	**94,52**	**99,91**	**100,01**	**99,52**	**100,15**	**100,83**
Data pt	157/1.	126/1.	128/1.	134/1.	138/1.	140/1.	141/1.	152/1.	125/1.	118/1.	120/1.	121/1.	130/1.	132/1.	142/1.
Min	Pl	Chl	Chl	Chl	Chl	Chl	Chl	Chl	Ilm	Am	Am	Am	Am	Am	Am
SiO2	62,37	25,16	25,58	25,71	25,42	25,55	25,92	25,29	0,06	45,43	45,44	45,35	46,84	46,50	47,09
Na2O	9,12	0,01	-0,02	0,00	0,01	0,00	0,00	0,01	-0,01	1,24	1,32	1,28	1,16	1,34	1,08
Al2O3	23,45	20,90	21,75	20,79	21,20	21,67	21,88	21,70	0,05	12,50	12,17	11,61	10,83	10,87	10,65
K2O	0,10	0,02	0,08	0,02	0,01	0,02	0,02	0,04	0,08	0,30	0,25	0,35	0,31	0,30	0,27
CaO	4,56	0,07	0,03	0,27	0,26	0,01	0,09	0,08	0,07	11,46	10,93	11,11	10,79	10,71	10,94
TiO2	0,02	0,51	0,09	0,09	0,06	0,08	0,07	0,08	53,00	0,31	0,32	0,30	0,25	0,29	0,28
FeO	0,24	21,29	21,43	21,65	21,23	21,54	20,94	20,86	42,88	15,54	15,36	15,81	15,22	15,67	14,95
MnO	0,03	0,21	0,15	0,18	0,16	0,11	0,15	0,17	1,67	0,28	0,27	0,20	0,21	0,24	0,21
MgO	-0,01	17,12	17,72	17,46	17,43	17,67	17,82	17,78	0,10	10,23	10,55	10,60	11,17	10,88	11,38
Cr2O3	-0,04	0,05	0,00	0,09	0,12	0,07	0,05	0,07	-0,02	0,10	0,10	0,41	0,00	0,03	0,01
Total	**99,84**	**85,35**	**86,82**	**86,27**	**85,91**	**86,71**	**86,95**	**86,10**	**97,87**	**97,39**	**96,71**	**97,01**	**96,76**	**96,82**	**96,86**

Data pt	151/1.	153/1.	158/1.	117/1.	119/1.	129/1.	133/1.	135/1.
Min	Am	Am	Am	Cal	Cal	Cal	Cal	Cal
SiO2	47,81	45,82	45,90	0,01	0,01	0,04	0,02	-0,01
Na2O	0,98	1,19	1,27	0,03	0,03	-0,01	0,00	0,03
Al2O3	9,25	11,70	11,55	-0,02	0,00	0,04	0,00	0,01
K2O	0,21	0,28	0,24	0,08	0,02	0,01	0,01	0,02
CaO	11,48	11,50	11,06	58,54	57,55	53,42	57,64	57,85
TiO2	0,22	0,29	0,30	-0,01	0,01	0,01	0,04	0,01
FeO	14,65	15,21	15,12	0,35	1,35	0,90	1,25	0,93
MnO	0,25	0,22	0,24	0,28	0,62	0,44	0,51	0,54
MgO	12,33	10,69	10,59	-0,02	0,49	0,75	0,61	0,32
Cr2O3	0,05	0,05	0,05	0,00	0,00	0,03	-0,05	-0,01
Total	**97,23**	**96,97**	**96,31**	**59,23**	**60,07**	**55,62**	**60,06**	**59,69**
Data pt	**136**	**146**	**147**	**148**	**149**	**144**	**145**	**150**
Min	Cal	Cal	Cal	Cal	Cal	Cal	Cal	Ep
SiO2	0,02	0,03	0,03	0,00	0,01	0,02	0,03	37,89
Na2O	0,06						0,01	-0,01
Al2O3	-0,01						0,00	27,50
K2O	0,02						0,08	0,01
CaO	58,43	51,45	54,27	52,00	52,45	52,98	59,71	23,87
TiO2	0,00						-0,01	0,08
FeO	0,88	1,18	0,87	0,84	0,80	0,76	0,32	6,83
MnO	0,50	0,43	0,44	0,34	0,43	0,33	0,42	0,14
MgO	0,33	0,78	0,63	0,56	0,58	0,41	0,01	-0,01
Cr2O3	0,00						0,03	0,10
Total	**60,23**	**53,87**	**56,23**	**53,73**	**54,27**	**54,49**	**60,58**	**96,40**

15.3 Sample 51-14

Data pt	76/1.	84/1.	85/1.	87/1.	88/1.	91/1.	93/1.	111/1.	112/1.	113/1.	79/1.	81/1.	92/1.	94/1.	110/1.
Min	Bt	Bt	Bt	Bt	Bt	Bt	Bt	Bt	Bt	Bt	Chl	Chl	Chl	Chl	Chl
SiO2	36,52	36,15	35,72	36,25	35,87	35,89	35,29	34,85	34,41	36,34	25,36	25,08	24,63	25,20	25,12
Na2O	0,09	0,11	0,07	0,10	0,12	0,10	0,08	0,08	0,06	0,14	-0,01	-0,01	0,02	0,01	0,00
Al2O3	17,70	18,22	18,33	18,99	18,15	18,84	18,91	18,38	18,13	18,72	21,75	21,55	22,60	22,50	21,17
K2O	8,98	9,00	9,03	8,89	9,12	9,05	9,19	8,56	7,57	9,06	0,02	0,05	0,02	0,07	-0,01
CaO	-0,01	0,00	-0,02	0,02	-0,02	-0,03	-0,03	0,15	0,02	0,02	0,10	0,02	0,03	-0,02	0,03
TiO2	2,04	1,59	1,95	1,58	1,42	1,03	1,66	1,17	1,45	1,02	0,05	0,07	0,07	0,08	0,08
FeO	18,70	19,42	19,39	20,37	19,14	18,71	19,79	21,50	20,95	19,50	24,50	24,15	25,03	24,48	24,94
MnO	0,01	0,07	0,07	0,06	0,05	0,05	0,09	0,14	0,14	0,08	0,11	0,16	0,16	0,13	0,12
MgO	10,08	9,99	9,79	9,84	10,11	10,38	9,54	8,98	10,73	10,35	15,28	15,08	14,64	14,79	15,03
Cr2O3	0,08	0,03	0,03	0,00	0,00	0,05	0,01	0,02	0,04	0,02	-0,01	0,01	0,01	0,04	0,00
Total	**94,20**	**94,59**	**94,37**	**96,10**	**93,96**	**94,06**	**94,53**	**93,83**	**93,49**	**95,25**	**87,15**	**86,17**	**87,20**	**87,28**	**86,49**

Datapunkt	82/1.	109/1.	95/1.	108/1.	77/1.	78/1.	80/1.	86/1.	83/1.	89/1.
Min	Cal	Cal	Ilm	Ilm	Ms	Ms	Ms	Ms	Pl	Pl
SiO2	0,02	0,04	0,78	0,03	48,23	46,90	46,41	46,66	61,89	61,71
Na2O	0,01	0,02	0,02	-0,01	0,47	0,79	0,78	1,06	8,61	8,69
Al2O3	-0,02	0,01	0,46	0,05	32,19	35,45	36,27	34,98	23,81	23,76
K2O	0,02	0,00	0,14	-0,01	9,93	9,69	9,98	9,32	0,08	0,09
CaO	55,87	55,31	0,04	0,04	-0,01	0,00	0,05	0,01	5,51	5,65
TiO2	0,01	0,01	52,75	53,10	0,36	0,40	0,15	0,28	-0,02	-0,01
FeO	0,14	0,53	45,04	45,86	1,99	1,41	1,36	1,72	0,09	0,06
MnO	0,02	0,03	1,06	1,08	-0,03	0,00	0,04	-0,02	0,01	0,02
MgO	-0,06	-0,08	0,16	0,05	1,95	0,92	0,74	0,95	-0,01	-0,01
Cr2O3	-0,01	-0,02	0,00	0,04	0,08	0,08	0,03	0,01	-0,01	0,00
Total	**56,00**	**55,86**	**100,45**	**100,23**	**95,17**	**95,64**	**95,81**	**94,98**	**99,96**	**99,97**

Data pt	96 /1.	97/1.	98/1.	99/1.	100/1.	101/1.	102/1.	103/1.	104/1.	105/1.	106/1.	107/1.
Min	Grt	Grt	Grt	Grt	Grt	Grt	Grt	Grt	Grt	Grt	Grt	Grt
SiO2	37,18	37,25	37,25	37,09	37,19	37,46	37,26	37,31	36,96	37,38	37,17	36,71
Na2O	0,01	-0,03	0,00	0,01	0,01	0,02	0,04	0,01	0,01	-0,01	0,01	0,02
Al2O3	21,01	21,02	20,85	20,90	20,72	20,97	21,04	21,07	20,95	21,34	21,01	20,78
K2O	0,00	-0,02	-0,01	-0,01	0,01	-0,02	-0,01	-0,02	-0,02	0,00	0,01	-0,01
CaO	6,38	7,60	8,30	7,78	7,89	8,07	7,91	8,15	8,42	8,07	7,88	7,07
TiO2	0,04	0,09	0,10	0,07	0,09	0,11	0,09	0,11	0,09	0,06	0,08	0,07
FeO	31,99	31,12	30,38	31,00	30,47	28,96	28,91	29,75	30,15	30,14	31,00	30,83
MnO	2,43	2,05	2,19	2,33	2,73	4,30	4,34	3,13	2,64	2,31	2,04	2,46
MgO	1,65	1,45	1,41	1,44	1,33	1,12	1,09	1,22	1,29	1,33	1,37	1,58
Cr2O3	0,02	0,03	0,03	-0,04	0,00	0,00	-0,01	0,01	0,03	0,04	0,01	0,04
Total	100,71	100,56	100,50	100,57	100,45	100,99	100,68	100,74	100,53	100,64	100,59	99,55

15.4 Sample 53-14

Data pt	1 / 1 .	4 / 1 .	7 / 1 .	8 / 1 .	13 / 1 .	12 / 1 .	17 / 1 .	5 / 1 .	14 / 1 .	15 / 1 .	2 / 1 .	3 / 1 .	6 / 1 .	9 / 1 .	16 / 1 .
Mineral	Bt	Bt	Bt	Bt	Bt	Chl	Chl	Chl	Pl	Pl	Ms	Ms	Ms	Ms	Ms
SiO2	35,89	36,84	36,59	36,97	36,80	25,18	36,96	25,37	68,65	62,65	46,31	47,37	46,23	47,24	47,47
Na2O	0,07	0,08	0,10	0,04	0,10	0,02	2,57	0,01	11,75	9,05	1,20	1,16	1,52	1,14	0,79
Al2O3	18,43	18,47	18,00	18,44	18,13	22,74	30,95	21,66	19,63	22,90	35,32	34,69	37,02	35,02	33,64
K2O	8,47	8,46	7,78	8,37	8,41	0,03	0,02	0,03	0,04	0,09	9,25	9,20	9,14	9,30	9,05
CaO	0,01	-0,04	0,03	0,03	-0,03	0,03	0,33	-0,02	0,18	4,66	-0,03	-0,02	-0,03	-0,07	-0,02
TiO2	1,56	1,73	1,57	1,82	1,29	0,09	0,85	0,07	-0,02	0,00	0,53	0,47	0,43	0,46	0,49
FeO	17,61	16,95	16,48	17,08	18,40	23,40	7,55	21,97	0,07	0,14	1,42	1,51	1,13	1,49	1,85
MnO	0,10	0,11	0,14	0,08	0,13	0,16	0,00	0,14	0,03	0,01	0,00	-0,01	-0,02	0,02	0,04
MgO	11,10	11,30	11,34	10,99	11,19	15,57	7,66	17,11	0,00	0,01	1,15	1,40	0,80	1,51	1,59
Cr2O3	0,03	0,05	0,03	0,01	0,05	0,04	0,03	-0,02	0,03	-0,02	0,01	0,02	0,02	-0,02	0,00
Total	93,27	93,95	92,06	93,83	94,46	87,27	86,93	86,32	100,35	99,50	95,16	95,78	96,25	96,08	94,91

Info	Element profile in fig. 5.20								
Data pt	18 / 1 .	18 / 2 .	18 / 3 .	18 / 4 .	18 / 5 .	18 / 6 .	18 / 7 .	18 / 8 .	18 / 9 .
Min	Grt	Grt	Grt	Grt	Grt	Grt	Grt	Grt	Grt
SiO2	37,10	37,08	36,80	36,87	36,56	36,55	36,86	36,74	36,83
Na2O	0,01	0,00	0,01	-0,01	0,03	0,00	0,03	-0,03	-0,01
Al2O3	21,30	20,99	20,72	20,73	20,73	20,54	20,61	20,84	20,84
K2O	0,01	-0,02	0,00	-0,01	0,00	0,00	0,00	0,00	0,01
CaO	3,52	3,91	4,04	3,83	3,87	4,03	3,68	4,07	3,88
TiO2	0,02	0,06	0,05	0,06	0,07	0,13	0,09	0,09	0,05
FeO	33,27	31,35	29,48	28,19	25,83	25,60	25,57	27,68	30,92
MnO	3,64	6,20	8,58	9,98	12,55	13,08	13,10	10,82	7,00
MgO	1,57	1,09	0,89	0,81	0,71	0,63	0,70	0,77	1,28
Cr2O3	0,02	-0,02	0,03	-0,01	0,00	0,04	-0,01	0,02	-0,03
Total	100,46	100,60	100,60	100,45	100,37	100,60	100,64	101,00	100,78

15.5 Sample 60-14

Data pt	48 / 1	40 / 1	41 / 1	28 / 1	29 / 1	31 / 1	38 / 1	43 / 1	34 / 1	35 / 1	50 / 1	51 / 1	23 / 1	25 / 1	26 / 1	42 / 1
Min	Bio	Bio	Bio	Bio	Bio	Bio	Bio	Bio	Bio	Bio	Bio	Bio	Bio	Ep	Ep	Chl
SiO2	40,30	39,44	39,71	39,03	39,64	39,78	39,42	40,59	39,62	39,77	39,76	40,23	39,82	35,92	35,61	27,99
Na2O	0,08	0,09	0,11	0,12	0,08	0,09	0,11	0,07	0,13	0,04	0,10	0,08	0,07	0,06	0,01	0,00
Al2O3	14,31	14,66	14,59	15,00	15,09	15,53	15,35	14,82	15,37	15,54	14,52	14,43	15,03	20,87	20,75	19,77
K2O	9,30	9,00	8,69	9,48	8,33	9,32	9,52	8,79	9,07	9,41	9,10	9,10	8,91	-0,01	0,01	0,04
CaO	0,05	0,12	0,18	-0,01	0,54	0,05	-0,01	0,22	0,16	0,09	0,06	0,05	0,16	20,57	21,16	0,05
TiO2	0,98	1,24	1,06	1,24	1,06	1,30	1,39	1,05	1,37	1,27	1,01	1,06	0,97	0,00	0,00	0,05
FeO	9,86	10,48	10,31	9,97	10,30	10,19	10,27	10,20	10,14	10,42	9,93	9,91	9,94	11,50	11,85	11,90
MnO	0,05	0,05	0,07	0,05	0,09	0,04	0,10	0,09	0,11	0,08	0,09	0,09	0,13	0,26	0,25	0,12
MgO	18,53	17,90	17,84	17,89	18,70	18,28	18,28	18,38	18,27	18,35	18,53	18,26	18,29	0,40	0,29	24,69
Cr2O3	0,96	1,23	1,11	0,50	0,63	0,59	0,76	0,99	0,57	0,54	1,23	0,89	0,80	0,95	1,01	1,21
NiO	0,36	0,42	0,36	0,32	0,38	0,33	0,30	0,32	0,31	0,33	0,35	0,32	0,39	0,06	-0,02	0,47
Total	**94,78**	**94,62**	**94,02**	**93,59**	**94,85**	**95,51**	**95,48**	**95,52**	**95,11**	**95,86**	**94,70**	**94,41**	**94,51**	**90,59**	**90,93**	**86,30**
Data pt	44 /1	45 / 1	36 / 1	37 / 1	30 / 1	46 / 1	47 / 1	27 / 1	24 / 1	20 / 1	21 / 1	22 / 1	49 / 1	52 / 1	53 / 1	39 / 1
Min	Chl	Chl	Am	Am	Am	Am	Am	Am	Am	Am	Am	Am	Tlc	Tlc	Tlc	Cal
SiO2	28,17	27,84	55,55	55,16	56,26	55,12	55,28	54,48	54,86	55,65	56,56	55,72	61,02	59,99	61,85	0,04
Na2O	0,00	-0,01	0,48	0,41	0,32	0,48	0,52	0,54	0,61	0,47	0,30	0,25	0,05	0,07	0,02	0,02
Al2O3	20,14	19,75	2,29	2,38	1,65	1,92	2,33	3,20	2,84	2,72	1,78	1,91	0,69	1,35	0,43	-0,01
K2O	0,02	0,02	0,03	0,05	0,03	0,03	0,04	0,08	0,05	0,06	0,04	0,07	0,03	0,27	0,10	0,00
CaO	0,07	-0,02	11,60	12,43	13,11	11,53	11,32	10,97	11,00	11,69	11,91	12,43	0,05	0,14	0,08	56,14
TiO2	0,03	0,02	0,04	0,02	0,03	0,03	0,02	0,06	0,07	0,06	0,03	0,04	0,00	0,05	0,01	-0,03
FeO	11,84	11,65	8,25	6,76	6,57	7,69	7,44	8,91	8,68	7,92	6,13	6,54	4,94	5,20	4,90	0,08
MnO	0,09	0,15	0,24	0,26	0,20	0,22	0,32	0,35	0,24	0,26	0,21	0,14	0,06	0,02	0,06	0,02
MgO	25,09	25,13	19,17	19,29	19,96	19,53	19,93	18,85	18,73	19,34	21,05	19,94	27,61	27,48	27,67	-0,07
Cr2O3	1,24	1,45	0,01	0,17	0,17	0,42	0,12	0,14	0,47	-0,03	0,04	0,28	0,19	0,21	0,06	0,02
NiO	0,41	0,33	0,07	0,15	0,13	0,14	0,14	0,17	0,04	0,09	0,18	0,17	0,55	0,48	0,48	0,02
Total	**87,11**	**86,31**	**97,73**	**97,09**	**98,42**	**97,12**	**97,46**	**97,75**	**97,59**	**98,24**	**98,23**	**97,52**	**95,18**	**95,26**	**95,64**	**56,23**

15.6 Sample 65-14

Data pt	74 / 1 .	69 / 1 .	53 / 1 .	54 / 1 .	55 / 1 .	64 / 1 .	61 / 1 .	66 / 1 .	67 / 1 .	63 / 1 .	71 / 1 .	80 / 1 .
Min	Grt	Grt	Grt	Grt	Grt	Grt	Pl	Pl	Pl	Pl	Pl	Pl
SiO2	38,06	37,67	38,13	37,73	37,94	35,78	61,55	61,79	62,88	64,73	63,30	65,94
Na2O	0,04	0,08	-0,01	0,02	0,02	0,02	8,59	8,76	9,25	9,76	9,41	11,37
Al2O3	21,16	21,19	21,39	21,05	21,18	20,54	23,71	23,47	22,79	22,25	22,81	19,40
K2O	-0,01	0,00	-0,01	0,00	0,01	0,00	0,07	0,09	0,08	0,06	0,10	0,06
CaO	11,20	12,74	12,75	11,20	11,31	10,92	5,70	5,39	4,54	3,96	4,37	0,95
TiO2	0,13	0,06	0,07	0,14	0,16	0,14	0,01	0,01	-0,01	0,01	-0,01	-0,01
FeO	24,61	24,42	24,59	25,52	25,57	25,74	0,20	0,40	0,26	0,15	0,23	0,43
MnO	2,21	0,63	0,74	1,56	1,63	1,44	-0,02	0,04	-0,01	0,00	0,01	0,05
MgO	2,95	2,69	3,17	2,66	2,28	2,92	-0,01	-0,02	-0,01	-0,01	0,00	-0,02
Cr2O3	0,01	0,02	-0,01	0,02	0,01	0,01	-0,01	-0,03	-0,01	0,01	-0,01	-0,04
Total	**100,36**	**99,52**	**100,82**	**99,90**	**100,12**	**97,51**	**99,79**	**99,91**	**99,75**	**100,92**	**100,20**	**98,13**
Data pt	**57 / 1 .**	**76 / 1 .**	**58 / 1 .**	**68 / 1 .**	**70 / 1 .**	**62 / 1 .**	**65 / 1 .**	**81 / 1 .**	**82 / 1 .**	**75 / 1 .**	**56 / 1 .**	**60 / 1 .**
Min	Pl	Chl	Am	Am	Am	Am	Am	Am	Am	Am	Am	Am
SiO2	64,08	24,14	44,12	44,69	45,60	43,71	41,64	41,85	43,10	43,70	40,62	42,98
Na2O	9,61	-0,01	1,55	1,39	1,61	1,38	1,64	1,55	1,49	1,72	1,75	1,73
Al2O3	22,36	19,90	12,71	11,80	11,64	12,70	15,26	14,43	13,93	13,71	16,24	13,88
K2O	0,10	-0,01	0,51	0,47	0,32	0,48	0,49	0,47	0,38	0,41	0,76	0,39
CaO	4,05	0,13	11,43	11,35	10,53	11,52	11,44	11,44	12,19	11,44	11,38	11,56
TiO2	-0,02	0,03	0,62	0,60	0,33	0,36	0,40	0,41	0,43	0,46	0,44	0,43
FeO	0,12	28,62	15,92	16,37	16,10	16,86	17,83	17,44	16,26	16,05	17,31	16,35
MnO	-0,03	0,34	0,33	0,31	0,37	0,35	0,28	0,32	0,25	0,25	0,36	0,29
MgO	0,00	12,91	9,65	9,60	10,37	9,04	7,61	8,71	8,98	9,50	7,69	9,20
Cr2O3	0,04	0,01	-0,03	0,01	-0,01	-0,01	-0,02	0,03	0,02	0,04	0,00	-0,01
Total	**100,32**	**86,06**	**96,79**	**96,59**	**96,85**	**96,40**	**96,59**	**96,65**	**97,03**	**97,28**	**96,57**	**96,79**

15.7 Sample 68-14

Data pt	1/1.	4/1.	13/1.	15/1.	16/1.	20/1.	21/1.	29/1.	34/1.	36/1.	38/1.	7/1.	25/1.	27/1.	33/1.
Min	Am	Am	Am	Am	Am	Am	Am	Am	Am	Ami	Am	Ep	Bt	Bt	Bt
SiO2	50,32	49,32	49,13	48,15	48,99	46,44	47,39	47,79	52,66	49,80	48,02	37,33	37,59	38,03	38,26
Na2O	1,20	1,23	1,19	1,14	1,31	1,44	1,30	1,28	0,58	1,23	1,37	0,01	0,16	0,10	0,13
Al2O3	7,82	8,41	7,95	8,75	8,92	10,81	9,34	9,83	4,26	8,35	9,98	24,58	16,31	16,13	16,82
K2O	0,20	0,21	0,22	0,19	0,22	0,27	0,22	0,24	0,13	0,21	0,26	-0,02	9,18	9,11	9,13
CaO	11,26	10,95	11,29	12,01	11,28	11,36	11,62	11,66	12,05	10,99	11,24	23,19	-0,10	-0,03	0,02
TiO2	0,16	0,21	0,18	0,15	0,24	0,30	0,15	0,26	0,08	0,21	0,29	0,09	1,01	0,97	0,94
FeO	11,73	11,80	12,61	12,27	12,47	12,82	12,74	12,56	10,50	12,35	12,74	10,09	14,67	14,50	14,21
MnO	0,21	0,18	0,22	0,20	0,26	0,17	0,20	0,20	0,22	0,20	0,25	0,14	0,06	0,12	0,07
MgO	14,46	14,21	13,94	13,96	13,84	12,98	13,71	13,42	16,72	14,05	13,37	-0,01	15,44	15,68	15,42
Cr2O3	0,06	-0,02	0,05	0,00	-0,01	0,03	0,09	0,02	0,00	0,03	0,03	0,06	0,01	0,04	0,05
NiO2	-0,01	0,01	-0,01	0,04	-0,01	-0,03	0,03	0,02	0,03	-0,02	0,05	-0,03	0,05	0,01	0,01
Total	97,41	96,51	96,78	96,85	97,51	96,59	96,79	97,28	97,24	97,39	97,59	95,43	94,38	94,67	95,06

Data pt	39/1.	39/1.	2/1.	5/1.	6/1.	10/1.	14/1.	24/1.	30/1.	37/1.	40/1.	42/1.	22/1.
Min	Bt	Bt	Chl	Chl	Chl	Chl	Chl	Chl	Chl	Chl	Chl	Chl	Cal
SiO2	38,46	38,46	26,57	26,86	27,24	26,89	26,75	26,59	26,95	26,72	27,85	27,08	0,01
Na2O	0,05	0,05	-0,01	0,01	0,01	0,00	-0,03	-0,01	-0,02	0,00	0,02	-0,01	0,00
Al2O3	16,84	16,84	21,52	21,32	20,99	20,79	21,07	21,19	20,98	21,39	21,39	21,55	0,01
K2O	9,94	9,94	0,12	0,03	0,01	0,00	0,00	0,00	0,03	0,02	0,74	0,00	0,03
CaO	0,02	0,02	0,02	0,05	0,04	0,01	0,05	0,00	0,03	0,01	0,04	0,01	56,01
TiO2	1,04	1,04	0,06	0,05	0,05	0,03	0,04	0,05	0,04	0,05	0,03	0,03	0,00
FeO	14,10	14,10	16,73	16,78	16,95	16,70	16,62	16,86	16,79	16,61	16,24	16,79	0,22
MnO	0,04	0,04	0,15	0,14	0,14	0,15	0,13	0,15	0,14	0,11	0,13	0,17	0,04
MgO	15,29	15,29	21,29	21,49	21,79	21,47	21,28	21,52	21,65	21,23	20,80	21,58	-0,07
Cr2O3	0,03	0,03	0,05	0,05	0,07	0,08	0,01	0,04	0,00	0,07	0,02	0,06	-0,03
NiO2	0,03	0,03	0,03	0,03	0,05	0,04	0,07	0,04	0,03	0,03	0,07	0,02	0,00
Total	95,84	95,84	86,53	86,81	87,34	86,17	86,00	86,42	86,63	86,23	87,32	87,30	56,22

Data pt	96/1.	97/1.	98/1.	99/1.	100/1.	101/1.	102/1.	103/1.	104/1.	105/1.	106/1.	107/1.
Min	Grt	Grt	Grt	Grt	Grt	Grt	Grt	Grt	Grt	Grt	Grt	Grt
SiO2	37,18	37,25	37,25	37,09	37,19	37,46	37,26	37,31	36,96	37,38	37,17	36,71
Na2O	0,01	-0,03	0,00	0,01	0,01	0,02	0,04	0,01	0,01	-0,01	0,01	0,02
Al2O3	21,01	21,02	20,85	20,90	20,72	20,97	21,04	21,07	20,95	21,34	21,01	20,78
K2O	0,00	-0,02	-0,01	-0,01	0,01	-0,02	-0,01	-0,02	-0,02	0,00	0,01	-0,01
CaO	6,38	7,60	8,30	7,78	7,89	8,07	7,91	8,15	8,42	8,07	7,88	7,07
TiO2	0,04	0,09	0,10	0,07	0,09	0,11	0,09	0,11	0,09	0,06	0,08	0,07
FeO	31,99	31,12	30,38	31,00	30,47	28,96	28,91	29,75	30,15	30,14	31,00	30,83
MnO	2,43	2,05	2,19	2,33	2,73	4,30	4,34	3,13	2,64	2,31	2,04	2,46
MgO	1,65	1,45	1,41	1,44	1,33	1,12	1,09	1,22	1,29	1,33	1,37	1,58
Cr2O3	0,02	0,03	0,03	-0,04	0,00	0,00	-0,01	0,01	0,03	0,04	0,01	0,04
Total	**100,71**	**100,56**	**100,50**	**100,57**	**100,45**	**100,99**	**100,68**	**100,74**	**100,53**	**100,64**	**100,59**	**99,55**